Can we Understand, Control and Use the Blinking of Quantum Dots in Biological Surroundings?

Nela Durisic

Ph.D.

Department of Physics

McGill University

Montréal, QC, Canada

A Thesis submitted to the Faculty of Graduate Studies and Research in partial fulfilment of the requirements for the degree of Doctor of Philosophy

31. 08. 2009.

To my sister, Svetlana for her love and for always being there for me; and to the memory of my parents, Rusica and Ivan, who would have enjoyed seeing this thesis published.

Abstract

Semiconductor nanocrystals, also known as quantum dots (QDs), are evoking remarkable technological and scientific interest due to their fascinating size-dependent electronic and optical properties. Many biophysical studies to date have used effectively as brighter and more photostable replacement of organic dyes. In this thesis we focus on the most prominent feature of their photophysical properties, a random switching between emitting and non-emitting states, also known as fluorescence intermittency, or “blinking,” in order to better understand the mechanism of quantum dot emission and how it reflects interaction with their immediate environment. We first designed and built a total internal reflection florescent microscope (TIRFM) with single molecule detection capabilities and determined optimal conditions for single QD studies. We then used image correlation techniques to show that the change in blinking dynamics could be detected and that it could complicate interpretation of the commonly used analytical techniques that rely on intensity fluctuations as reporters of particle mobility. In particular, we demonstrated that the transport coefficients recovered from fluorescence fluctuation analysis of diffusional mobility using temporal image correlation spectroscopy (TICS) had significant systematic errors due to

blinking of the nanoparticles. We then performed a thorough, systematic study of the effects of protons on QDs' photochemical stability by varying the pH of their aqueous environment and related the single particle properties to properties of an ensemble of QDs. As pH was lowered, shorter "on" times and longer "off" times were observed, brightness of single QDs decreased and the number of permanently non-emitting QDs (dark fraction) increased. Based on these results, we proposed a coupled role for H^+ ions by which they first reduced the intensity of the emitting state as well as affected probabilities of the QD to switch between the "on" and "off" states and eventually trapped the QD in a permanent dark state. We discussed and extended theoretical blinking models to account for the effect of the H^+ ions as well as to highlight a common mechanism governing blinking and the dark fraction formation. Results presented in this thesis are particularly important for developing a more complete theory of QD blinking, but are also relevant in various applications of QDs, especially for quantitative biological imaging applications where pH variations exist between the cytoplasmic and extra cellular spaces and within cellular organelles.

Résumé

Les nanoparticules semi-conductrices, aussi connues sous le nom de particules quantiques (PQ), suscitent un grand intérêt dans les domaines technologiques et scientifiques en raison de leurs propriétés spectroscopiques uniques et avantageuses. À ce jour, plusieurs études de biophysique ont remplacé succès les sondes fluorescentes organiques traditionnelles par des PQ.

Cette thèse porte principalement sur l'étude de la propriété la plus photophysique des PQ, soit leur capacité à activer ou à inactiver de manière aléatoire l'émission fluorescente (plus connue sous le nom de l'intermittence de l'émission fluorescente, ou « clignotement »), dans le but de mieux comprendre le mécanisme entourant l'émission des particules quantiques et son interaction avec son environnement immédiat.

Nous avons tout d'abord conçu et construit un microscope de fluorescence par réflexion totale interne (TIRFM) qui a la capacité de détecter une seule molécule et de déterminer les conditions idéales afin d'étudier une PQ unique. Nous avons ensuite utilisé des techniques de spectroscopie de corrélation temporelle dans les images afin de montrer que l'intermittence de l'émission fluorescente pouvait être détectée et qu'elle pourrait rendre possible l'interprétation d'analyses plus

complexes que les techniques d’analyse traditionnelles qui se fondent sur les clignotements fluorescents comme preuve du mouvement des particules.

De façon plus précise, nous avons démontré que les coefficients de transport obtenus d’analyses utilisant la technique de spectroscopie de corrélation temporelle dans les images (TICS) présentaient une marge d’erreur significative due au « clignotement » des nanoparticules. Ensuite, nous avons procédé à une étude systématique plus approfondie des effets des protons sur la stabilité photochimique des PQ, en modifiant le pH de leur environnement aqueux et en faisant des liens avec les propriétés d’une seule particule dans un ensemble de PQ. Au fur et à mesure que le pH diminuait, nous avons observé une diminution du temps d’émission fluorescente, « ouvert », et une augmentation du temps d’absence d’émission, « éteint ». Nous avons également noté une diminution dans la clarté d’une seule PQ et une augmentation dans le nombre de PQ n’émettant aucune clarté (fraction sombre).

À la lumière de ces résultats, nous avons avancé l’idée d’un rôle double des ions H+, qui réduiraient d’abord l’intensité de l’état d’émission et affecteraient ensuite la probabilité d’une PQ d’alterner entre les états d’émission et d’absence d’émission, pour éventuellement emprisonner la PQ dans un état de fraction sombre permanent. Nous avons analysé et élargi les modèles théoriques concernant le « clignotement » afin de tenir compte des effets des ions H+ et de mieux démontrer que le « clignotement » et la formation de fraction sombre se fondent sur un seul et même mécanisme.

Les résultats présentés dans cette thèse sont particulièrement importants pour l'élaboration d'un modèle théorique complet du « clignotement » d'une PQ, mais peuvent également être importants pour les différents usages des PQ, en particulier dans les applications d'imagerie dans le domaine de la biologie quantique, où on retrouve des variations de pH entre les espaces cytoplasmiques et extracellulaires et dans les différents organes cellulaires.

Acknowledgements

I would like to thank Peter Grutter and Paul Wiseman for their understanding, support and for freedom they gave me in designing the work published in this thesis, Colin Heyes for making the research we did together so pleasurable experience, and Florek and Zoé for being there for me during preparation of this manuscript.

Table of contents

Introduction 1

Chapter 2

Chapter 3

Chapter 4

Chapter 5

Chapter 6

Chapter 7

List of figures

Chapter 2

Chapter 3

Chapter 4

Chapter 5

Chapter 6

Chapter 7

List of Tables

Chapter 3

Chapter 6

Statement of Originality

Following aspects of the thesis constitute original contribution to advancement of knowledge:

Chapter 4

Image Correlation Analysis is used instead of commonly used histogram method to determine QD blinking statistics.

The rate of decay of measured image correlation curves using time image correlation spectroscopy (TICS) reflects variations in the QD power-law blinking statistics.

A model developed by Rogier Verberk and Michel Orrit is used to fit image correlation spectroscopy curves in order to quantify their decay and extract power law exponents.

The Verberk and Orrit model describes the correlation curve calculated from a single QD. We show that the model is applicable to the correlation decay of an ensemble of quantum dots as well.

The rate of the decay of measured correlation curves, and therefore accuracy and precision of the recovered power-law parameters, are affected by the number of single emitters in an image and by temporal sampling.

Chapter 5

Effects of QD blinking on diffusion measurements using temporal image correlation spectroscopy (TICS) are established.

The extent of bias introduced by QD blinking in diffusion measurements, using temporal image correlation spectroscopy (TICS), is quantified for different blinking rates and diffusion coefficients.

Reciprocal space image correlation spectroscopy analysis (kICS) is applied to calculate accurate diffusion coefficients.

Chapter 6

Both blinking statistics and dark fraction of QDs are affected by pH in a systematic way.

The form of the probability distribution function describing blinking changes when the QDs are taken from an air-exposed environment into an aqueous one.

Theoretically predicted critical time at which the power-law blinking behaviour changes its rate is experimentally observed in the aqueous environment.

A role if protons in QD blinking is proposed; they first reduce the intensity of the emitting state and affect the probabilities of the QD to switch between “on” and “off” states until eventually QD is trapped in a permanent “off” state.

Theoretical blinking models developed by Tang and Marcus and Frantsuzov and Marcus are extended to account for the effect of protons as well as to highlight their common principles.

Chapter 7

Effect of pH on photo physical properties of single QDs is related to the fluorescence properties of QD ensemble.

Decay in fluorescence intensity with time of QDs freely diffusing in pH solution is irreversible and pH dependent.

Concentration of hydrogen ions and dissolved oxygen is found to be important for ensemble fluorescence decay, suggesting that a proton-catalyzed oxidation process is responsible for the decay.

Decay of fluorescent lifetime is described by four characteristic decay times, the longest of which is found to be pH dependent and is related to formation of surface trap states.

The change of the ensemble quantum yield of QDs in biologically relevant environment is not just determined by bright to dark fraction ratio but also by the change in quantum yield of individual dots.

Contributions of Authors

Chapter 2

N. Durisic designed and constructed The Total Internal Reflection Fluorescence Microscope. All measurements and data analysis were done by N. Durisic.

Chapter 3

All measurements and data analysis were done by N. Durisic.

Chapter 4

N. Durisic designed and performed experiments. Simulations of QD blinking were done by B. Herbert. Data analysis was done by A. Bachir.

Chapter 5

N. Durisic designed and performed all experiments. Simulations of QD blinking were done by B. Herbert and A. Bachir. Data analysis was done by N. Durisic and A. Bachir. Data on quantum dots diffusing in a cell membrane were obtained from C. Lagerholm. KICS analysis was done by D. Kolin.

Chapter 6

C. Heyes synthesized uncapped CdSe quantum dots. N. Durisic designed and performed all experiments. Data analysis was done jointly by N. Durisic and C. Heyes.

Chapter 7

N. Durisic designed and performed all microscopy measurements. All other measurements were done jointly by N. Durisic and C. Heyes. A. Godin analyzed time resolved lifetime data.

Can we Understand, Control and Use the Blinking of Quantum Dots in Biological Surroundings?

1. Introduction

1.1 Motivation

Fluorescent semiconductor nanocrystals (NCs), also known as quantum dots, or QDs, are small crystalline particles which are several nanometers in size and contain a few hundreds of atoms. Because of such a small size, their excitonic wave functions are confined in all three spatial dimensions. This quantum confinement has dramatic consequences. Below a certain size, properties of semiconductors start to deviate significantly from the bulk and start to resemble those of single molecules. Compared to the bulk material, the band edge of the NCs becomes blue shifted by the amount of confinement energy, allowing for the shift to be fine tuned by choosing the nanocrystal size. In addition, a larger probability for recombination of electrons in the valence band and holes in the conduction band significantly increases their ability to emit light. Small size and light emission are the two most important properties of NCs which are evoking tremendous technological and scientific interests in this class of materials.

The first theoretical and experimental description of quantum confinement in three dimensions in semiconductor nanocrystals was developed by Ekimov and Efros in early the 1980s (1-3). They explained how quantum confinement modifies the density of states leading to discretization and increased spacing of electron and hole energy levels. Ten years later, highly monodispersed CdSe

QDs with a very wide range of quantum confinements and much improved crystallinity were synthesized (4). This led to many advances in understanding of electronic properties of QDs in particular the role of surface atoms. It was assumed that small quantum yield and highly intermittent light emission of bare nanocrystals were due to the unpassivated atoms on their surface. Note that a CdSe quantum dot whose diameter is 5 nm has about 25% of its atoms at the surface. If unpassivated these can be involved in trapping and non-radiative recombination of charge carriers. Growing a shell of wider band gap material, such as ZnS, around a CdSe core has substantially improved fluorescence by providing electron and hole barriers (5). Finally in 2000, new synthesis protocols involving air-stable ionic precursors were introduced, thus overcoming potential hazards and allowing for this material to be readily available from commercial companies (6).

1.2 Properties and Applications

In modern biological analysis various kinds of organic dyes and fluorescent proteins are commonly used as labels of molecules of interest. Compared to them QDs have considerably enhanced photophysical properties. They can be designed to obtain quantum yields close to 90% and photostability several orders of magnitude higher then conventional dyes (7, 8). This allows for single molecule tracking up to several hundreds of minutes using confocal microscopy (9), wide-field epifluorescence (10, 11), or total internal reflection microscopy (12). In addition, their long excitation state lifetime allows for time gated detection in order to eliminate shorter-lived background autofluorescent species often encountered in cells (13). Wide excitation spectra and narrow band emission of QDs not only allow for simultaneous excitation of multicolour nanocrystal labels (9), but they also make possible their use as customizable donors for fluorescent resonant energy transfer (14).

Properties of QDs arising from quantum confinement can be used for device design. Lately, much scientific effort is directed toward their applications in fields of solar energy conversion (15), light emitting diodes (16, 17) and lasers (18). Photon anti-bunching in the fluorescence of single CdSe/ZnS nanocrystals opened a variety of quantum optical applications such as quantum cryptography and quantum computation (19).

Studies of single semiconductor quantum dots have revealed many interesting properties and processes which could not be observed in ensemble measurement. Most important of them are blinking (20), spectral jumps (21), multiple and long luminescence lifetimes (22) and systematic blue shifts (20). Spectral jumps or spectral diffusion are random and are correlated with blinking. They are related to ionization of quantum dots due to Auger processes (20, 23-26). As a result of the ionization and subsequent recombination processes, charge distribution around the dot changes, resulting in spectral shift of the emission (26). The blue shift is irreversible and has been attributed to photooxidation of the core in the quantum dot (20, 27). Degradation of QDs caused by oxidation can take several discrete steps, with each of them having only a small effect on overall optical properties of individual QDs. Gradually it will result in a decrease in the emission count rate, prolonged non-emissive periods and eventually bleaching.

1.3 Scope of This Thesis

One of the most prominent features of semiconductor nanocrystals, almost entirely neglected in biophysical applications, is their intermittent fluorescent emission (“blinking”). Blinking is random switching between an emitting (“on”) and non-emitting (“off”) state under continuous laser illumination. While it can be used as a signature of a single fluorophore and as a tool which allows breaking of the diffraction limit, in many cases it leads to loss of information on labelled molecules. It is described by Levy statistics, which indicates complex behaviour and multiple processes involved in the transitions from bright to dark states. Our interest was to examine whether systematic change in blinking dynamics could be detected, to examine possible causes of it and see if we can control and use it for biological applications.

In order to detect single QD fluorescence, a TIRF microscope was first built. In the 2nd Chapter we explain its setup and establish optimal conditions for single QD imaging. The change of blinking rate was first detected as a function of laser power for an ensemble of immobilized QDs and then for the dots diffusing in two dimensions. Results of these experiments together with techniques used for data analysis are described in chapters 3 and 4. Chapters 5 and 6 deal with effects of environmental changes on blinking. Specifically we examine effect of positive charges on blinking and dark fraction formation and then relate optical properties of an ensemble of QDs to those of single nanocrystals. Chapters 2-5 have been published as peer reviewed papers, chapter 6 will be submitted shortly.

References

1. A.I. Ekimov, A. A. O. 1981. Quantum size effect in 3-dimensional microscopic semiconductor crystals. JETP Lett. 34.
2. Al.L. Efros, A. L. E. 1982. Interband absorption of light in a semiconductor sphere. Soviet Phys. Semiconductors–USSR 16:772-775.
3. Rossetti, R., S. Nakahara, and L. E. Brus. 1983. Quantum size effects in the redox potentials, resonance Raman spectra, and electronic spectra of CdS crystallites in aqueous solution. The Journal of Chemical Physics 79:1086-1088.
4. Murray, C. B., M. Nirmal, D. J. Norris, and M. G. Bawendi. 1993. Synthesis and structural characterization of II-VI semiconductor nanocrystallites (quantum dots). Z. Phys. D: At., Mol. Clusters 26:231-233.
5. Hines, M. A., and P. Guyot-Sionnest. 1996. Synthesis and Characterization of Strongly Luminescing ZnS-Capped CdSe Nanocrystals. J. Phys. Chem. 100:468-471.
6. Peng, Z. A., and X. Peng. 2001. Formation of high-quality CdTe, CdSe, and CdS nanocrystals using CdO as precursor. J. Am. Chem. Soc. 123:183-184.
7. Reiss, P., J. Bleuse, and A. Pron. 2001. Highly Luminescent CdSe/ZnSe Core/Shell Nanocrystals of Low Size Dispersion. Nano Lett. 2:781-784.
8. Sukhanova, A., J. Devy, L. Venteo, H. Kaplan, M. Artemyev, V. Oleinikov, D. Klinov, M. Pluot, J. H. Cohen, and I. Nabiev. 2004. Biocompatible fluorescent nanocrystals for immunolabeling of membrane proteins and cells. Anal. Biochem. 324:60-67.
9. Lacoste, T. D., X. Michalet, F. Pinaud, D. S. Chemla, A. P. Alivisatos, and S. Weiss. 2000. Ultrahigh-resolution multicolor colocalization of single fluorescent probes. Proc. Natl. Acad. Sci. U. S. A. 97:9461-9466.

10. Dahan, M., S. Lévi, C. Luccardini, P. Rostaing, B. Riveau, and A. Triller. 2003. Diffusion Dynamics of Glycine Receptors Revealed by Single-Quantum Dot Tracking. Science 302:442-445.
11. Hohng, S., and T. Ha. 2004. Near-Complete Suppression of Quantum Dot Blinking in Ambient Conditions. J. Am. Chem. Soc. 126:1324-1325.
12. Michalet, X., F. Pinaud, T. D. Lacoste, M. Dahan, M. P. Bruchez, A. P. Alivisatos, and S. Weiss. 2001. Properties of fluorescent semiconductor nanocrystals and their application to biological labeling. Single Molecules 2:261-276.
13. Dahan, M., T. Laurence, F. Pinaud, D. S. Chemla, A. P. Alivisatos, M. Sauer, and S. Weiss. 2001. Time-gated biological imaging by use of colloidal quantum dots. Opt. Lett. 26:825-827.
14. Medintz, I. L., A. R. Clapp, H. Mattoussi, E. R. Goldman, B. Fisher, and J. M. Mauro. 2003. Self-assembled nanoscale biosensors based on quantum dot FRET donors. Nat Mater 2:630-638.
15. Huynh, W. U., J. J. Dittmer, and A. P. Alivisatos. 2002. Hybrid nanorod-polymer solar cells. Science 295:2425-2427.
16. Coe, S., W. K. Woo, M. Bawendi, and V. Bulovic. 2002. Electroluminescence from single monolayers of nanocrystals in molecular organic devices. Nature 420:800-803.
17. Bulovic, V., S. A. Coe, W.-K. Woo, and M. G. Bawendi. 2003. Light emitting device including semiconductor nanocrystals. In PCT Int. Appl. (Massachusetts Institute of Technology, USA). Wo. 46 pp.
18. Klimov, V. I., A. A. Mikhailovsky, S. Xu, A. Malko, J. A. Hollingsworth, C. A. Leatherdale, H. Eisler, and M. G. Bawendi. 2000. Optical gain and stimulated emission in nanocrystal quantum dots. Science 290:314-317.
19. Michler, P., A. Imamoglu, M. D. Mason, P. J. Carson, G. F. Strouse, and S. K. Buratto. 2000. Quantum correlation among photons from a single quantum dot at room temperature. Nature 406:968-970.

20. Nirmal, M., B. O. Dabbousi, M. G. Bawendi, J. J. Maklin, J. K. Trautman, T. D. Harris, and L. E. Brus. 1996. Fluorescence intermittency in single cadmium selenide nanocrystals. Nature 383:802-804.
21. Empedocles, S. A., D. J. Norris, and M. G. Bawendi. 1996. Photoluminescence Spectroscopy of Single CdSe Nanocrystallite Quantum Dots. Phys. Rev. Lett. 77:3873-3876.
22. Fisher, B. R., H.-J. Eisler, N. E. Stott, and M. G. Bawendi. 2004. Emission Intensity Dependence and Single-Exponential Behavior in Single Colloidal Quantum Dot Fluorescence Lifetimes. J. Phys. Chem. B 108:143-148.
23. Efros, A. L., and M. Rosen. 1997. Random Telegraph Signal in the Photoluminescence Intensity of a Single Quantum Dot. Phys. Rev. Lett. 78:1110-1113.
24. Banin, U., M. Bruchez, A. P. Alivisatos, T. Ha, S. Weiss, and D. S. Chemla. 1999. Evidence for a thermal contribution to emission intermittency in single CdSe/CdS core/shell nanocrystals. J. Chem. Phys. 110:1195-1201.
25. Neuhauser, R. G., K. T. Shimizu, W. K. Woo, S. A. Empedocles, and M. G. Bawendi. 2000. Correlation between fluorescence intermittency and spectral diffusion in single semiconductor quantum dots. Phys. Rev. Lett. 85:3301-3304.
26. Empedocles, S. A., and M. G. Bawendi. 1997. Quantum-confined stark effect in single CdSe nanocrystallite quantum dots. Science 278:2114-2117.
27. Katari, J. E. B., V. L. Colvin, and A. P. Alivisatos. 2002. X-ray Photoelectron Spectroscopy of CdSe Nanocrystals with Applications to Studies of the Nanocrystal Surface. The Journal of Physical Chemistry 98:4109-4117.

Chapter 2

2. Total Internal Reflection Fluorescence Microscopy of Single Quantum Dots

Total internal reflection (TIR) was first introduced to fluorescent microscopy by Daniel Axelrod in the early 1980s (1). Since then it has been widely used for selective two dimensional illumination of fluorophores at interfaces to study cell membrane molecules, surface reactions and single molecules.

2.1 Theoretical Aspects of TIR

The principle of TIR is based on Snell's law (equation (1)). If light traveling through optically dense medium (index of refraction n_1) strikes a less dense medium (index of refraction n_2) at an angle of incidence θ_1, larger than a certain "critical angle" (θ_c), the light will undergo total internal reflection. This is illustrated in figure 1(a). As the incident angle increases, transmitted light refracts toward the interface with higher index of refraction. When the critical angle is reached the transmitted light takes a path along the interface (figure 1(b)).

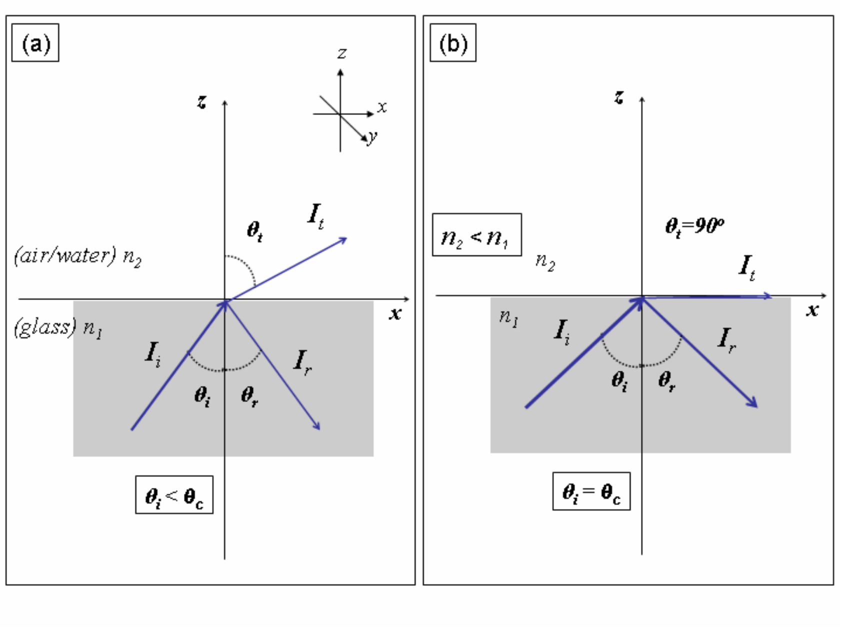

Figure 1

The coordinate system used here to describe total internal reflection. xz-plane is the plane of incidence, the y-axis is perpendicular to it. The evanescent beam is created in the xz-plane and penetrates a depth *d* into the lower refractive index medium. I_i, I_t and I_r are incident, transmitted and reflected rays respectively. (a) The incident angle is smaller than critical angle. (b) The incident angle is equal to the critical angle.

Critical angle increases as n_2 to n_1 ratio decreases. For glass/air and glass/water interface it can be calculated as follows:

$$n_1 \sin\theta_1 = n_2 \sin\theta_2 \qquad (1)$$

For $\theta_1 = \theta_c$, $\theta_2 = 90^\circ$ Equation (1) gives

$$\theta_c = \sin^{-1}(\frac{n_2}{n_1}) \qquad (2)$$

If $n_1 = 1.518$ ° (glass) and $n_2 = 1.0003$ (air) then $\theta_{c\text{glass/air}} = 41.22$ °. In case of glass/water interface $n_1 = 1.518$ ° and $n_2 = 1.33$ (water) gives $\theta_{c\text{glass/water}} = 61.18$ °.

At incident angles $\theta > \theta_c$, some of the energy penetrates the medium of lower refractive index as an evanescent wave, propagating parallel to the plane of incidence. For an infinitely wide beam the evanescent wave intensity decays exponentially with distance form the interface:

$$I(z) = I_0 e^{-\frac{z}{d_p}} \qquad (3)$$

where $I(z)$ is the evanescent field intensity at the distance z above the glass surface, I_0 is the intensity at the interface and *dp* is the penetration depth defined as the distance beyond the optical interface required for the electric field amplitude to fall to the e^{-1} of its value at the interface. For the light of wavelength λ_0 the penetration depth is given by:

$$d = \frac{\lambda_0}{2\pi}(n_2{}^2 \sin^2 \theta - n_1{}^2)^{-\frac{1}{2}} \tag{4}$$

In measurements carried out here a penetration depth of less than 150nm was easily achieved. The net effect is that only fluorophores in a thin optical plane on the glass coverslip are excited leaving those deeper in the sample in the dark. This provides a vertical resolution and signal-to-noise ratio which is unmatched by any other fluorescence technique and is a primary asset of TIRF-based microscopy.

The polarization of the evanescent wave *I(z)* depends on the incident light polarization and can be calculated from boundary conditions for electric and magnetic field vectors at the interface and Fresnel coefficients. For “s” polarized incident light, the electric field vector of the evanescent wave remains normal to the plane of incidence, while for “p” polarization its direction remains in the plane of incidence but it curls along the surface with non zero longitudinal component. When an incident beam is “s” polarized the factor $I(0)$ has a form:

$$I_y(0) = I_s \frac{4\cos^2\theta}{1-(\frac{n_1}{n_2})^2} \tag{5}$$

While for “p” polarization there are two orthogonal components of electric field at the boundary. If each of them is considered separately, corresponding intensities at the interface are:

$$I_x(0) = I_p \frac{4\cos^2\theta(\sin^2\theta - (\frac{n_1}{n_2})^2)}{(\frac{n_1}{n_2})^4\cos^2\theta + \sin^2\theta - (\frac{n_1}{n_2})^2} \tag{6}$$

$$I_z(0) = I_p \frac{4\cos^2\theta\sin^2\theta}{(\frac{n_1}{n_2})^4\cos^2\theta + \sin^2\theta - (\frac{n_1}{n_2})^2} \tag{7}$$

I_s and I_p are intensities of the “s” and “p” polarized incident light in the glass.

For subcritical angles of incidence, $\theta < \theta_c$, the intensity of the “s” polarized transmitted light is given by:

$$I_y(0) = I_s \frac{2\sin\theta_t\cos\theta}{\sin(\theta_t + \theta)} \tag{8}$$

Equations (5) and (8) are used to plot the theoretical intensity of transmitted “s” polarized light in air (gray) and water (black) in figure 2.

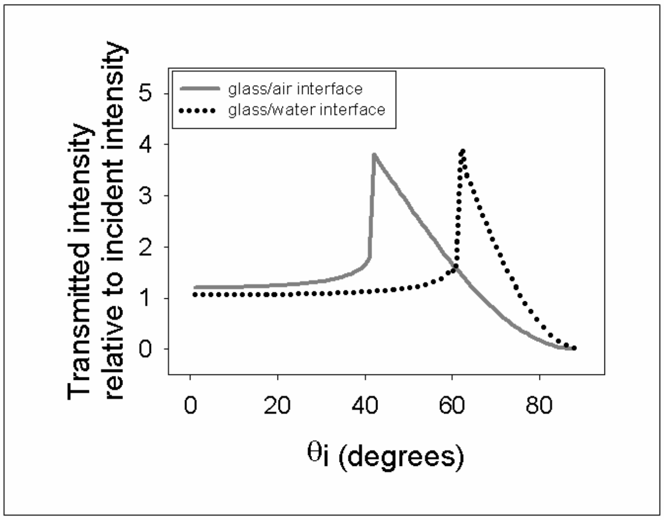

Figure 2

Transmitted intensity enhancement on a low refractive index side of a dielectric interface as calculated from equations (5) and (6). Critical angles for glass/air and glass/water interfaces are $\theta_{c\text{glass/air}} = 41.22$ ° (full gray line) and $\theta_{c\text{glass/water}} = 61.18$ ° (dotted black line). The enhancement is nearly equal to 4.

Around the critical angle the intensity of evanescent wave is larger then the incident intensity and decays to zero when the incident angle approaches 90°. As the incident angle θ approaches θ_c, the incident and reflected amplitudes add constructively to produce intensity approximately four times the average intensity in the glass. For $\theta \to 90^\circ$, the phases add destructively, resulting in a decrease in irradiance to zero at the interface. The same effect is present in the case of p-polarized light.

2.2 Experimental Considerations

Several geometries have been used to introduce the excitation light at an angle greater than the critical angle (2-5). We built a through-the-objective TIRF apparatus since this setup can be used also as a normal inverted epifluorescence microscope and allows mounting of an atomic force microscope on the stage without compromising optical quality. The basic operational principle of through-the-objective TIRF is shown in figure 3.

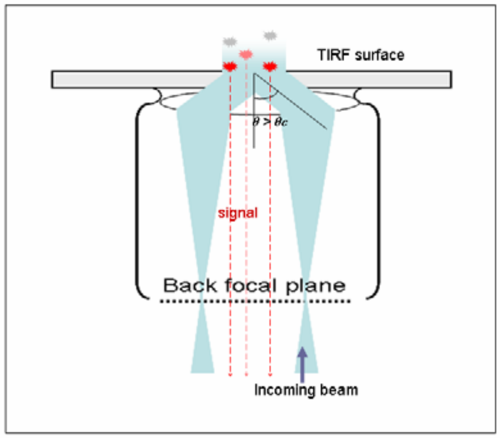

Figure 3

Schematic drawing of objective type TIRF. Laser light is brought to focus at the back focal plane of the objective with a high numerical aperture. When the incident beam is positioned to propagate along the objective edge the beam is totally internally reflected, producing an evanescent wave at the glass/air (glass/water) interface.

When the laser excitation beam is focused at the back focal plane of the objective it comes out collimated at the sample stage. If the incident light is centered on the optical axis and parallel to it the microscope is in EPI illumination mode. As the beam translates off-axis to the side of the objective it comes out at increasingly large angles and gets reflected back in to the objective after the critical angle is reached.

Details of the setup are shown in figure 4.

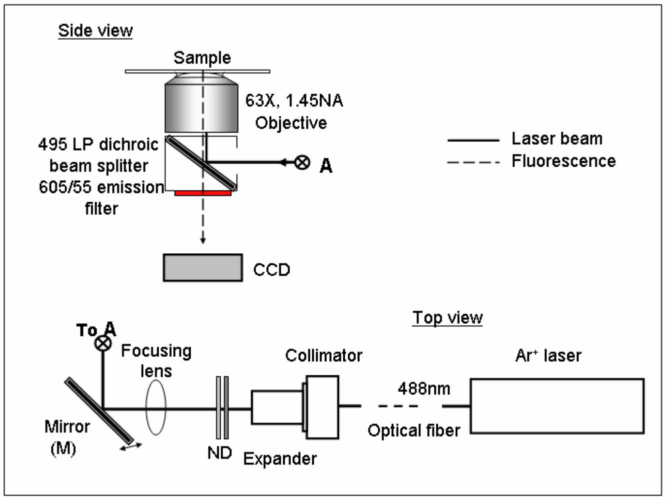

Figure 4

Schematic illustration of through the objective TIRF apparatus used in the measurements presented here. Mirror (M) is used to switch between EPI and TIRF imaging modes.

Our TIRF apparatus is constructed around a commercial Zeiss 135 TV Axiovert S100 microscope (Carl Zeiss, Jena, Germany). Illumination light is provided by a tunable argon-ion laser (Melles Griot 35 LAP 431, Ottawa, ON) equipped with an intra cavity prism for single-line operation. This laser can operate at nine different wavelengths characteristic for Ar+ and can be used for excitation of most biologically relevant fluorescent labels. The laser beam is coupled to a single mode optical fiber (O.Z. Optics, Ottawa, ON) equipped with laser to fiber coupler with adjustable focus and fiber collimator at the other end. The output beam was then expanded using a 5× beam expander (Melles Griot, Ottawa, ON) to a final beam diameter of 3.85 mm. The laser light was focused on the back focal plane of the objective with a planoconvex lens (f = 165 mm) and reflected from a round silver mirror into the objective. The mirror is mounted on a kinematic mirror mount, which allows rotation around two axes. This controls the angle of incidence and permits switching from EPI to TIRF mode to be easily achieved. Rotation around two axes provides displacement of the beam along both x and y-axis in such a way that TIRF can be achieved in several locations in the xy-plane. We used an oil immersion lens Zeiss 63x1.45 NA, Plan-apochromat (focal length 2.5mm) designed to operate in a medium of n=1.52. The numerical aperture of the objective determines the maximum angle at which objective can emit and receive light. Here the maximum incident angle is determined to be 72.78^o, which allows about 43% of the aperture to be used for TIRF for a glass/air and about 10% for a glass/water interface. The corresponding minimum penetration depths are calculated to be $d_{min(glass/air)}$=68nm and $d_{min(glass/water)}$=106nm (assuming values of n_{air}=1.0, n_{water}=1.33 and n_{glass}=1.518 for glass coveslips).

In this setup the objective is used for both illumination of a sample and collection of the fluorescence signal. Therefore careful filtering of residual scattered excitation light and fluorescence emission signal is necessary. For that purpose we used a 495 DCLP dichroic mirror and a 605/55nm emission filter combination (Chroma Technology, Rockingham, VT). A series of neutral density filters (ND) are introduced in the beam path between the expander and focusing lens to adjust the illumination intensity. A shutter placed after the expander was used to restrict illumination to periods of data acquisition.

Images are collected using an intensified frame-transfer CCD camera (IPentaMax, Princeton Instruments, Trenton, NJ, USA) attached to the bottom port of the microscope. The gain of the intensifier can be adjusted by changing the MCP voltage setting (arbitrary units). With the use of 63 x objective, the CCD pixel size of 15 μm corresponds to 0.37 μm in the object space as determined experimentally by imaging a standard chart. Taking into account Rayleigh's definition of resolution and Nyquist’s sampling theorem a magnification of $2 \times \text{pixel size} \times \text{NA}/0.61\lambda$ will yield a quantum dot diffraction limited image over 3.6×3.6 pixels of the camera chip.

2.3 Characterization of microscope performance:

Illumination intensity distribution and incident angle dependence

To visualize the illumination profile of the evanescent field and confirm that there was no freely propagating light when the microscope was in TIRF configuration we imaged uniformly spread fluorescein solution on a glass coverslip. The fluorescence appeared as a small roughly circular green spot in the middle of the field of view due to geometrical constrains of through the objective TIRF. If incident angles much larger than θ_c were allowed, like in TIRF configurations using a prism for example, a cross section of the incident beam in the sample plane would have been elongated creating highly elliptical illumination region. Here the beam enters the objective along x-axis and totally internally reflects from the glass surface producing very little scattered light along the entry path as shown in a contour plot of CCD counts in figure 5.

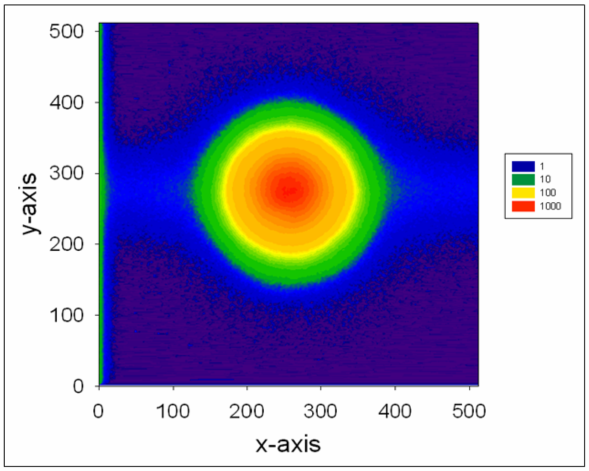

Figure 5

Contour plot showing illumination profile of evanescent wave in the sample plane as measured from fluorescein dye solution. Logarithmic color scheme corresponds to the number of counts recorded by the CCD detector. The maximum number of counts is 1034. A small increase in background (light blue) is due to the scattered light along the beam path. 488nm Ar+ laser line was used for excitation with an incident power of 1mW. MCP gain setting was at 1%.

The non-uniform spatial intensity distribution is caused by the Gaussian laser beam shape. The width (FWHM) of the fluorescent region along x and y-axis as determined from the fit to a two dimensional Gaussian function is ω_x= 41.37+/-0.02 μm and ω_y= 37.46+/-0.02 μm respectively. This size of illumination area is particularly useful for imaging of single quantum dots using an area detector. It minimizes excitation light scattered within the objective, which significantly lowers background light, and yet it allows simultaneous detection of many nanocrystals in parallel.

In the TIRF setup, illumination intensity is commonly estimated as the total power in the laser beam entering the objective divided by the size of illuminated area in the sample plane. The absolute intensity incident on the glass/air or glass/water interface has somewhat different values due to losses in the optical path. We measured 30% of the original power to be lost in the objective. In addition, equations (5) and (8) predict an increase of incident intensity at the interface when switching from EPI to TIR-illumination. To test weather or not this is the case we measured fluorescence of the dye solution as a function of incidence angle. Mirror (M) (see figure 4) was used to shift the incident beam with respect to the main axis of the objective changing the angle of incidence and shifting the center of illuminated area along x-axis. We switched first to EPI-illumination and then systematically increased the angle of incidence to the point of achieving TIR and well beyond the critical angle until no fluorescence from the sample could be observed. Fluorescence signals collected for ten different mirror positions are plotted in figure 6.

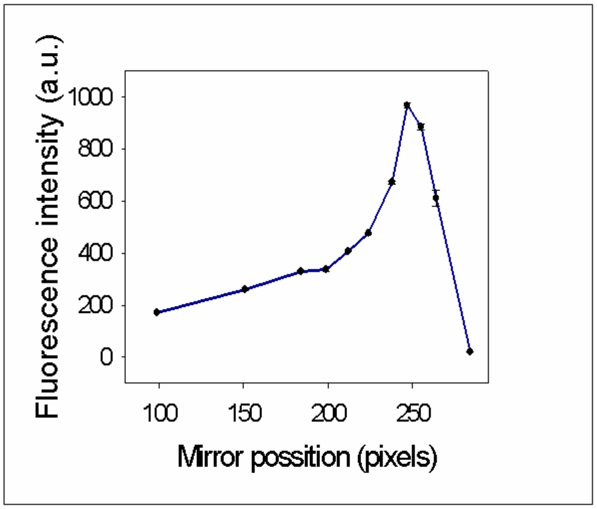

Figure 6

Plot showing change in measured fluorescence intensity from fluorescein solution as a function of the position of illuminated region as the incident angle is changed from EPI to TIRF configuration. Each point represents the average signal from a small (10x10 pixel) area taken from the center of the illumination profile. Error bars are standard deviation of the signal. (Incident illumination 488nm laser line, 1mW, MCP gain setting 1%, pixel size corresponds to 0.37 μm in sample space)

We were not able to map out the full theoretical curve since incident angles larger than 72^o could not be achieved. Thus, the drop of the signal to background level for the last mirror position is not due to destructive interference of incoming and reflected amplitude as in the theoretical curve, but because the incident angle surpassed 72^o. Around θ_c the signal increased about 5 times which was slightly more than theoretically predicted. This can be explained by taking in to account that equation 5 and 8 are derived strictly for transmitted wave at the interface. In the measurement conducted here the objective collects the signal from around a 500nm thick region of the sample and contributions to the illumination intensity from the exp$(-z/dp)$ term in equation (3) can not be neglected. As mentioned earlier, the penetration depth of the evanescent field is the largest for angles just above the critical angle increasing the number of photons collected by the objective.

A short penetration depth and the increase of incident intensity are two main advantages of TIRF that allow high signal to noise ratio to be achieved. When samples are thick fluorescent molecules at the glass interface will appear brighter than when imaged under EPI illumination primarily because the small penetration depth of the evanescent field eliminates background signals coming from regions further away from the glass. When samples are thin, such as single molecules or quantum dots dispersed on the glass surface, contributions to the background from regions further away from the glass are negligible. However, they will still appear brighter than if imaged under EPI illumination due to higher pumping intensity of the evanescent wave.

2.4 Detection capabilities: Signal to Noise Ratio (SNR), Signal to Background Ratio (SBR) and Amplification of the Signal

We now determine Signal to Noise Ratio (SNR)and Signal to Background Ratio (SBR) figures of merit as a function of laser power for the system described above. To avoid the effect of evanescent field decay we use polystyrene microspheres (diameter 20nm) sparsely dispersed on the glass coverslip. In all calculations only the signal from the brightest pixel of the diffraction limited spot representing a microsphere was measured. The SNR was calculated as the average value of the signal above the background level collected from 10 microspheres divided by its standard deviation. The SBR was determined as the mean signal (signal plus background) divided by the average background signal. Maximum signal and background levels and their corresponding variance are dependent on intrinsic characteristics of fluorescent molecules and on the image acquisition parameters such as excitation power, signal amplification (gain) and integration time.

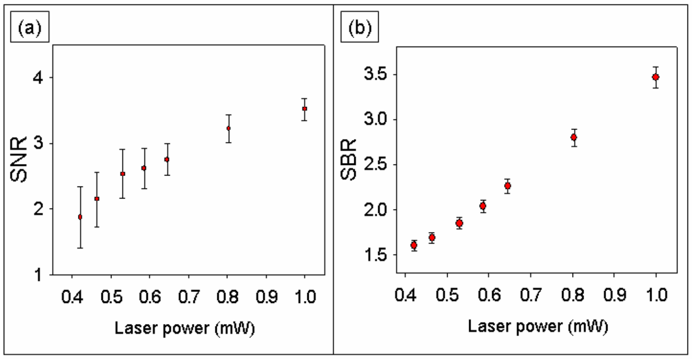

Figure 7

Excitation power dependence of (a) signal to noise and (b) signal to background ratio calculated for the sample of polystyrene microspheres (20nm in diameter) dispersed at the glass surface. Each point is an average signal collected from N=10 microspheres. Error bars are standard deviations. (Acquisition rate 5MHz, 50ms integration time, MCP gain setting 5%) When expressed in terms of power densities, this range of laser powers corresponds to 14W/cm^2 - 1 kW/cm^2 in sample plane.

As shown in figure 7a, SNR increases with excitation power for low to moderate powers and it levels off around 1mW. Higher powers produce better signal. However, the power can not be increased arbitrarily because if the rate of absorption of incident photons gets too high, molecules can not decay to the ground state fast enough and a saturation effect occurs. Further increase of incident power only produces higher background signal and consequently decreases SNR. Accordingly we made an effort to stay in a regime where the fluorescent signal exhibits linear increase with laser power.

Based on the assumption that only Poisson (shot) noise fluctuations are present, Basche at all have introduced the following equation to estimate the SNR of fluorescent dye molecules (6):

$$SNR = \frac{Signal}{(noise)_{rms}} = \frac{APt}{\sqrt{APt + C_b Pt + N_d t}} \qquad (10)$$

Here P is excitation power, t is the detector counting interval (integration time), C_b is the background count rate per watt of excitation power and N_d is the dark count rate. Factor A includes fluorescence quantum yield of the fluorophore, its absorption cross section and collection efficiency of the instrument. In the limit of negligible dark counts, SNR increases as the square root of excitation power which is in agreement with the trend we observe in figure 7a.

The background term in equation (10) arises from optical elements of the microscope (glass filters, objective and in some cases laser source) and from the sample itself. The latter includes Rayleigh scattering of the laser wavelength from the glass substrate, Raman scattering by the solvent or host matrix and residual fluorescence from impurities which is red shifted to the spectral region of molecules of interest.

Figure 7b shows the change of SBR with the laser power. When dark counts are negligible and saturation effects are absent, the signal and the background are increasing linearly with the laser power and linear increase of SBR with incident power is preserved. We note here that in some cases impurities can be bleached during the measurement which will manifest itself as the change of slope in figure 7b. Thus, SBR can be used as a measure of quality of the sample and the ability of the detection system to reduce the background. SNR however, is a more essential property since it describes the ability to detect the signal compared to noise fluctuations that are present and it helps determine the optimal laser power that should be used to image fluorescent species of interest. In addition, both SNR and SBR can be used as sensitive indicators that photobleaching is present in the system. Because it causes temporal decay of the signal under constant illumination power even slow bleaching rate will noticeably decrease SNR and SBR values in time.

2.5 Signal amplification

In all TIRF measurements performed in this work we used an intensified frame transfer CCD camera as a detection system. This camera has multichannel plates positioned between the photocathode and phosphor screen. The primary advantage of this design is that it allows for multiplication with a selected gain of photoelectron before readout. This makes the readout noise less important and increases sensitivity so that even one emitted photoelectron can be recorded. Limitations of this detector arise from excess noise that may arise from the multiplication process and nonuniform gain over different channels in the intensifier plate. Gain is controlled by an analog potentiometer that changes the voltage acceleration on the multichannel plates in a linear fashion, but the electron multiplication gain does not have a linear dependence on the voltage applied. Changes in the multiplication factor can produce additional fluctuations of signal and background values. Hence, optimizing the overall gain of the camera is of critical importance for quantitative studies as the same relative increase in sample photo-emission will appear to be significantly different at high and low gains.

In an attempt to characterize the gain parameter we imaged fluorescence polystyrene microspheres immobilized on glass coverslips and measured the signal and background as a function of intensifier gain. These measurements are performed in both EPI and TIRF setting keeping the laser power and all other experimental parameters the same. To avoid differences caused by higher pumping of evanescent wave, we adjusted the angle of incidence in the TIRF configuration so that transmitted illumination light in both settings has approximately the same value. We found that a linear increase in gain setting generates an exponential increase in both signal and background values with the same growth constant of (0.08+/-0.02) % (figure 8). This constant is called growth factor and, as a characteristic of the detection system, it is independent of illumination power.

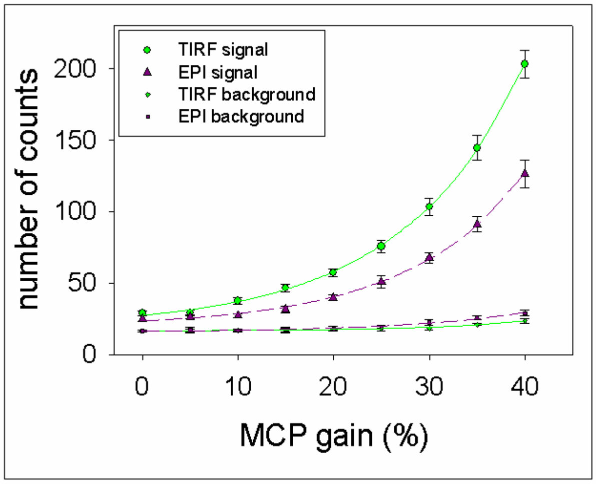

Figure 8

Plot showing signal and background for different MCP gain setting recorded from N=10 microspheres in EPI (dark purple) and TIRF (green) imaging modes. Lines represent best fit exponentials. Incident intensity is 1mW. Maximum gain can be set to 100% however, for this incident intensity detector saturation occurs at gain higher than 40%.

While the signal increases much more rapidly than the background, they both show that even small differences in fluorescent signal become pronounced for higher gain settings. Consequently, the variation in pumping intensity across the illumination profile becomes more significant and variance of fluorescent signal even across distances on the order of tens of pixels will reflect variations of amplification. High gain settings used to monitor the signal variation with time, give a more accurate estimate of the true variation in the emission of fluorescent species.

Having this in mind we evaluated SNR and SBR for the same sample (figure 9).

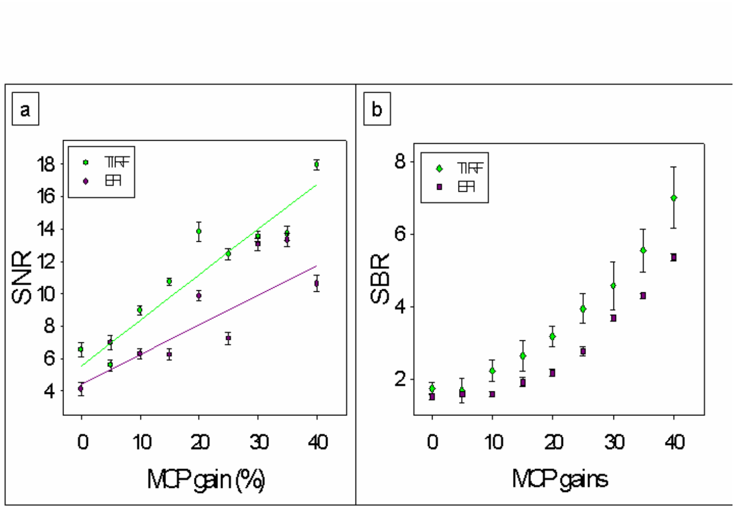

Figure 9

Signal to noise (a) and signal to background ratio (b) as a function of MCP gain setting calculated for N=10 microspheres imaged in EPI (dark purple) and TIRF (green) microscope configurations. Incident intensity is 1mW. The lines in (a) are shown to guide the eye.

For low gain settings SNR in TIRF and EPI configurations had similar values because the difference in signal and noise terms in equation (7) was minimal. As the gain setting was increased SNR increased primarily because the signal was amplified more than the background and the overall contribution from background fluctuations in the denominator of equation (7) became smaller. The best SNR value of 18 was achieved for the highest gain setting in TIRF configuration. Figure 9b plots SBR for this sample. Since both signal and background increased exponentially a nonlinear increase of SBR with gain setting was the expected trend. Based on these results we conclude that the excess noise effects caused by fluctuations in gain amplification factor and multiplication process are minimal over the range of gain settings used here.

References

1. Axelrod, D. 1981. Cell-substrate contacts illuminated by total internal reflection fluorescence. J. Cell Biol. 89:141-145.
2. Ambrose, W. P., P. M. Goodwin, and J. P. Nolan. 1999. Single-molecule detection with total internal reflection excitation: Comparing signal-to-background and total signals in different geometries. Cytometry 36:224-231.
3. Conibear, P. B., and C. R. Bagshaw. 2000. A comparison of optical geometries for combined flash photolysis and total internal reflection fluorescence microscopy. J Microsc 200:218-229.
4. Axelrod, D. 2001. Total internal reflection fluorescence microscopy in cell biology. Traffic 2:764-774.
5. Axelrod, D. 2003. Total internal reflection fluorescence microscopy in cell biology. Methods Enzymol 361:1-33.
6. Basché, T., W. P. Ambrose, and W. E. Moerner. 1992. Optical spectra and kinetics of single impurity molecules in a polymer: spectral diffusion and persistent spectral hole burning. J. Opt. Soc. Am. B 9:829-836.

Chapter 3

3. Quantum Dot Detection: Fluorescent Signal Characteristics, Signal to Noise Ratio (SNR) and Signal to Background Ratio (SBR)

3.1 Fluorescent Signal Characteristics

To determine the ability of the microscope to detect single quantum dot fluorescence we collected a series of images of QDs immobilized on a clean glass slides as a function of illumination power. MCP gain setting was adjusted to 25% as this value allowed us to cover the largest range of laser powers, and was kept constant in all measurements described in this section. In order to minimize background signal glass slides were cleaned in piranha solution then rinsed with MiliQ water and dried using nitrogen flow. For detailed sample preparation see Ch. 3. All images were recorded in air.

Unlike in samples with microspheres, a large variability of fluorescence emission across an image of QDs was observed. This is mainly due to discrete turning on/off of a single nanocrystal during the CCD signal collection. Besides on/off behavior there was also a variation in quantum yield between dots observed as a variation in the "on" time intensity. In addition to the creation of defects and redistribution of local electric fields around the nanocrystals, changes in quantum yield of individual dots may exist because of variability of nanocrystals' structure, variations in the organic coating, and position with respect to pixels on the CCD chip. To minimize the influence of these factors on our results we collected image series from the same ensemble of dots while changing the laser illumination intensity.

Illustrative eleven consecutive images of a dot together with a time profile of the brightest pixel in each image are shown in figure 1(a). A sudden single step disappearance and subsequent recovery of the signal are typical for quantum dot blinking. The full intensity time trajectory of the same dot (figure 1(b)) suggests that some of the observed heterogeneity in fluorescence emission was due to “on” and “off” events which occurred during CCD collection time. A histogram of fluorescent intensities confirms that the trace is generated by collection of photons coming from a single dot. Because of QD blinking, the density of emitting nanocrystals can not be accurately determined from a single image.

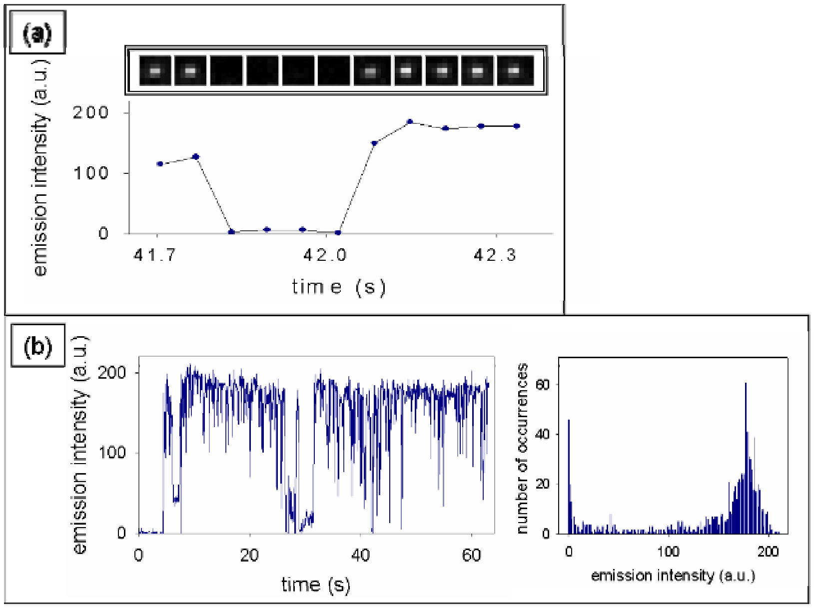

Figure 1

(a) Short section of emission intensity of a single QD is shown in the graph. Rapid rise and fall is due to the intermittent behavior of quantum dots. Boxes (2.6 x 2.6 μm) show 11 consecutive images from which the trace is extracted. (b) The full trajectory of emission time trace of the same dot contains “off” periods of variable length. Histogram of the emission intensities indicated that the trace reflects single QD behavior.

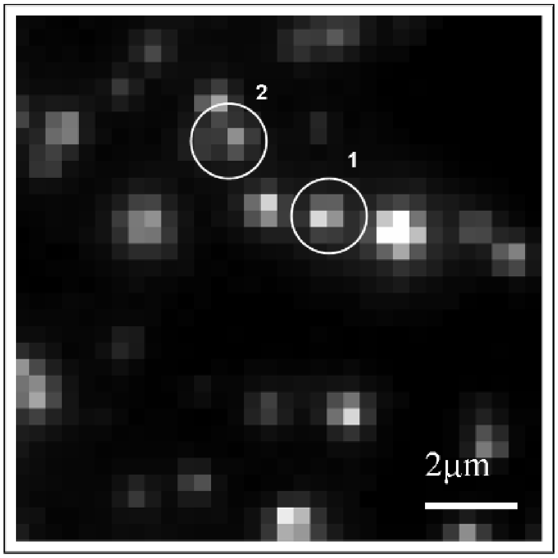

Figure 2

Sum of all 1000 images from an image sequence of QDs. Difference in brightness of individual QDs reflects different amount of time that they spent in “on” state. Intensity time trace of the dot marked as 1 is shown in figure 1 (b). Dot marked as 2 is not suitable for analysis because it is in close proximity to another dot (see figure 3).

Instead, a sum of images from each image sequence was used to establish the suitable surface density and localize single QDs. One such sum is shown in figure 2. Surface density of dots was kept low (less than one QD per 1um^2) to insure that each bright spot corresponds to only one dot. In order to discriminate between single dots and small aggregates that might have remained during sample preparation we applied the following criteria:

1) Diameter of diffraction limited spot representing a dot was equal to the size of the point spread function of the microscope (3.5+/-0.5 pixels).

2) The fluorescence time trace of each dot exhibited single step ‘on’ and ‘off’ events and the magnitude of ‘on’ intensity state is reproducible among all single dots in an image sequence.

3) The intensity distribution of each fluorescent spot exhibited one peak corresponding to “on” times and one peak corresponding to “off” times.

As an example the dot marked with number 2 in figure 2 was excluded from the analysis because it’s time trace revealed more than one peak in the intensity distribution probably due to proximity of neighboring dots (see figure 3), while the one in figure 1b is an example of a dot suitable for analysis.

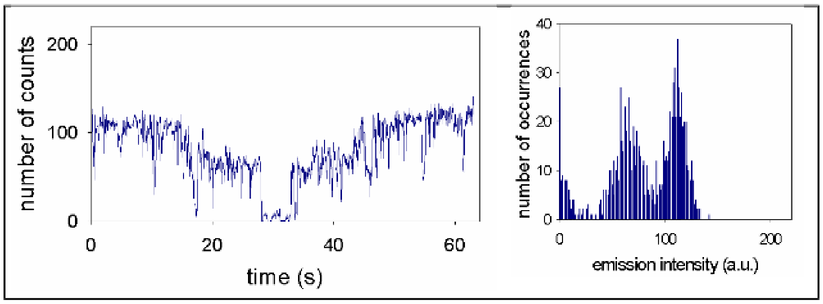

Figure 3

Fluorescence time trace of the QD marked as 2 in figure 2. From the step size in the trace it is difficult to conclude if it reflects optical properties of one or two dots. However, its emission intensity histogram shows two fluorescent peaks indicating hat this trace contains photons collected from two dots.

Our experience is that such a rigorous approach to data analysis significantly improves our ability to detect differences in fluorescent emission of QDs under different conditions.

Figure 4 shows typical emission time traces obtained for the same quantum dot at different laser powers (only the first 12s of each trace are shown). The intensity of the excitation beam was varied from 0.3mW to 3.3mW (approximately 0.01 kW/cm^2 to 0.1 kW/cm^2 in the sample plane) while keeping the gain setting of the camera constant. Several differences were apparent at low and high powers. At low powers only short ‘Off’ times were recorded. In fact, at the lowest power the emission was ‘On’ most of the time. For powers higher than 1mW, a substantial increase in the number of ‘On’/’Off’ cycles was observed and long off times were present. In agreement with previous results the length of ‘On’ times scaled inversely with excitation power (1). Non-linear dependency of QD fluorescence emission on excitation intensity was evident.

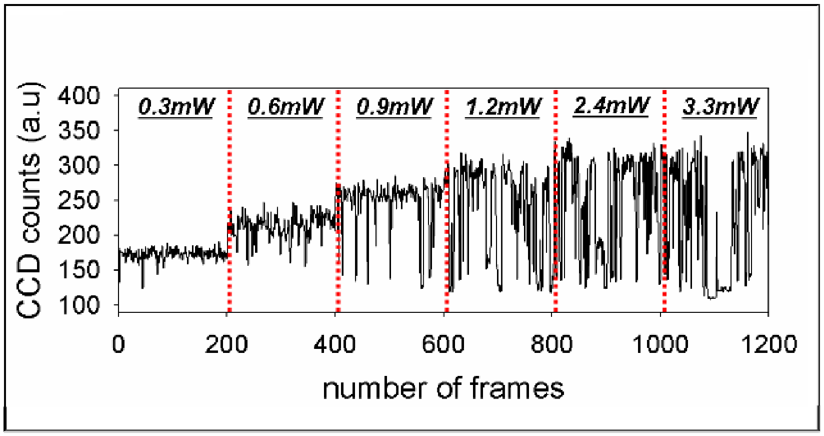

Figure 4

Fluorescence time trace of a single QD as a function of excitation intensity. An increase in both average “on” time intensity and blinking are evident with increasing laser power.

Similar characteristics have been observed previously in single molecules in which variation of fluorescent emission with laser intensity could be described as saturation occurring in two level homogeneously broadened systems (2, 3). This optical saturation is caused by partial depopulation of the ground state of the QD excitons, so that the average excitation rate is lower than the simple product of absorption cross-section and excitation light intensity.

Figure 5 shows average fluorescent emission as a function of excitation power obtained from an ensemble of 20 quantum dots. The intensity values were extracted solely from the bright intervals in each time trace and were background corrected. We found that our data were in good agreement to a relation between the fluorescence emission rate $k=F/t_{int}$ of a single emitter and the excitation intensity which has been derived for single molecules (4):

$$F = \frac{k_{\infty} t_{\text{int}}}{1 + \left(\frac{I_s}{I}\right)} \qquad (7)$$

Here F is detected fluorescence, t_{int} is the integration time of detection system, I_s is saturation intensity and I stands for laser excitation intensity.

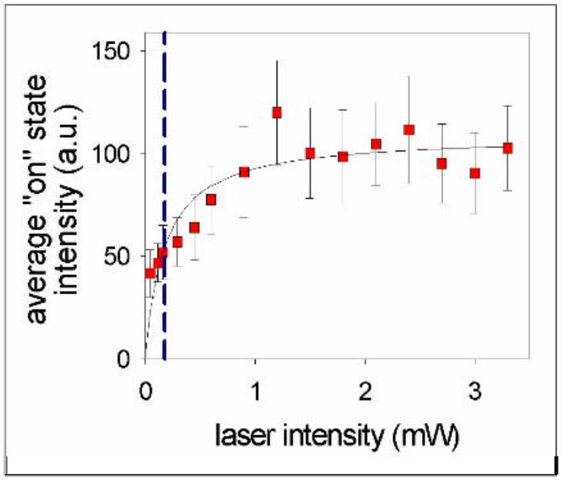

Figure 5

Saturation curve measured for an ensemble of QDs. Each point presents average “on “ time intensity from 20 dots. Error bars are standard deviations. Solid black line is a fit to a model described by equation 7. Blue line shows calculated saturation intensity.

A maximum emission rate of k_{∞} = 2180 counts/ms and excitation saturation intensity I_s = 0.18+/-0.05 mW were determined from the fit to the equation (7). The maximum emission rate constant depends on quantum yield and all excited state decay rates of quantum dots and it has been shown to differ from dot to dot (5). We found that the determination of the saturation parameters were of great importance in single QD studies to establish optimal experimental conditions. Under saturation the maximal cycling rate between the phonon excited and ground states leads to strong thermal energy dissipation as well as to a maximal probability for trapping processes leading to increased blinking and eventually to irreversible photo bleaching (6). Furthermore under saturation the background count rate usually increases faster than the emission rate and eventually decreases signal to background ratio.

3. 2 Signal to Noise Ratio (SNR) and Signal to Background Ratio (SBR)

Figure 6 shows signal to noise ratio calculated from the ensemble of QDs applying the same procedure as for microspheres. Due to variable emission intensity and transitions to ‘Off’ states during detector’s collection time, noise on quantum dots’ emission is non Poissonian. Because of that, in order to estimate correct SNR for fluorescent nanocrystals, equation (10) in Ch. 2 should contain an additional term in the denominator which takes in to account quantum dot blinking during integration time. The noise on 'On' times increases with laser power and it becomes comparable to signal value at powers higher than 0.6 mW (see figure 4).

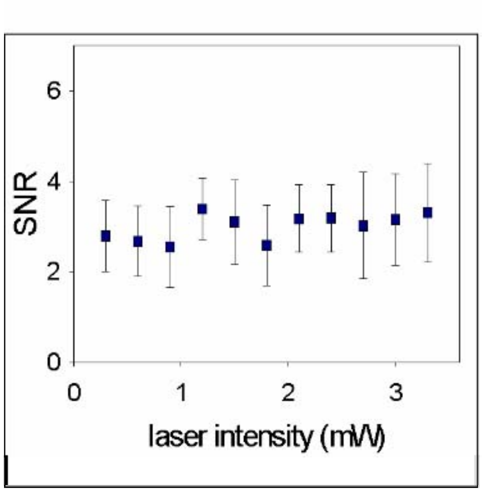

Figure 6

Signal to noise ratio stays between 2 and 4 as excitation intensity increases. This is because blinking becomes more pronounced at high laser powers therefore creating more noise in "on" times.

As a consequence, SNR stays constant in the range of excitation intensities examined here. In terms of the best SNRs we could achieve, the brightest quantum dots yielded a value between 4 and 5. SBR on the other hand is laser power dependent. The change of its value from about 2 to 6 as shown in figure 7, reflects the increase of the signal with laser power.

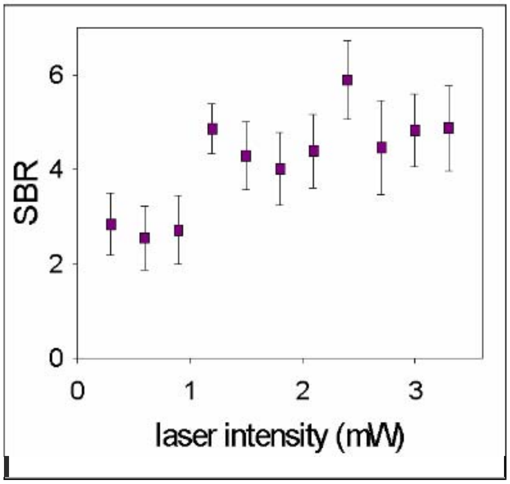

Figure 7

Signal to background ratio increases with laser power.

Both SNR and SBR can be increased by increasing the detection efficiency and reducing the background. However, the data in figure 6 suggest that SNR can not be increased by using a larger excitation power. In order to improve SNR one should make use of quantum dots' photo stability and extend integration time. Thus quantum dots as single molecule fluorescent probes are particularly suitable markers to be used in studies of relatively slow and long dynamic processes.

References:

1. Javier, A., and G. F. Strouse. 2004. Activated and intermittent photoluminescence in thin CdSe quantum dot films. Chemical Physics Letters 391:60-63.
2. Jung, G., J. Wiehler, W. Göhde, J. Tittel, T. Basché, B. Steipe, and C. Bräuchle. 1998. Confocal microscopy of single molecules of the green fluorescent protein. Bioimaging 6:54-61.
3. Dickson, R. M., A. B. Cubitt, R. Y. Tsien, and W. E. Moerner. 1997. On/off blinking and switching behaviour of single molecules of green fluorescent protein. Nature 388:355-358.
4. Ambrose, W. P., T. Basche, and W. E. Moerner. 1991. Detection and spectroscopy of single pentacene molecules in a p-terphenyl crystal by means of fluorescence excitation. The Journal of Chemical Physics 95:7150-7163.
5. Ebenstein, Y., T. Mokari, and U. Banin. 2002. Fluorescence quantum yield of CdSe/ZnS nanocrystals investigated by correlated atomic-force and single-particle fluorescence microscopy. Applied Physics Letters 80:4033-4035.
6. Pandey, A., and P. Guyot-Sionnest. 2008. Slow Electron Cooling in Colloidal Quantum Dots. Science 322:929-932.

One of the most intriguing features of QD photophysics is the poorly understood property of fluorescence intermittency, or blinking.

The observed “on” and “off” time probability density, $P(t_{on(off)})$, has the form of an inverse power law with measured exponents in the range between 1.1 and 2.2, peaking at about 1.5 (1-3).

We found that the exponent values depend significantly on how the raw data were analyzed. The usual approach is to calculate the probability density for the occurrence of “on” or “off” events using histogram analysis which is then fit to a power law. The method which involves the least data manipulation uses the following definition of the probability density:

$$P(t_{on(off)}) = \frac{N(t_{on(off)})}{N_{on(off)}^{tot}} \times \frac{1}{\Delta t}$$

but it heavily depends on the experimental duration and time resolution Δt. When the distribution is calculated in this manner the undersampling of rare events occurring only a few times or not at all during a particular experiment leads to an incorrect calculation of the probability of those events. This shows as a plateau at long times in the distribution. To overcome this limitation Kuno at al., used a weighting procedure which takes in to account the time duration of the adjacent events (1, 2, 4). The distribution can be additionally smoothed by choosing a logarithmically increasing bin length (3) and then it can be fitted either directly to a power law, or log[P($t_{on(off)}$)] can be calculated and a linear fit applied. Each of these alterations of raw data changes the best-fit power-law exponent leading to a conclusion that the variation of exponents in the literature is probably partly due to how the raw data were analyzed. In addition, histogram analysis itself requires setting of an intensity threshold value to separate “on” and “off” times, which can also affect the analysis results.

To overcome these shortcomings we characterized blinking dynamics using the fluctuation method image correlation spectroscopy (ICS). Our findings are presented in the next chapter.

1. Kuno, M., D. P. Fromm, H. F. Hamann, A. Gallagher, and D. J. Nesbitt. 2000. Nonexponential blinking kinetics of single CdSe quantum dots: A universal power law behavior. J. Chem. Phys. 112:3117-3120.
2. Kuno, M., D. P. Fromm, H. F. Hammann, A. Gallagher, and D. J. Nesbitt. 2000. Nonexponential "blinking" kinetics of single CdSe quantum dots: A universal power law behavior. J. Chem. Phys. 112:3117-3120.
3. Shimizu, K. T., R. G. Neuhauser, C. A. Leatherdale, S. A. Empedocles, W. K. Woo, and M. G. Bawendi. 2001. Blinking statistics in single semiconductor nanocrystal quantum dots. Phys. Rev. B 63:2053161.

4. Kuno, M., D. P. Fromm, H. F. Hamann, A. Gallagher, and D. J. Nesbitt. 2001. "On"/"off" fluorescence intermittency of single semiconductor quantum dots. J. Chem. Phys. 115:1028.

Chapter 4

4. Characterization of Blinking Dynamics in Quantum Dot Ensembles Using Image Correlation Spectroscopy

Reprinted with permission from:
Characterization of Blinking Dynamics in Quantum Dot Ensembles using Image Correlation Spectroscopy, A. Bachir, N. Durisic, B. Hebert, P. Grutter, P. W. Wiseman. J. Appl. Phys. 99: 064503-1-064503-7 (2006).

4.1 Introduction

Semiconductor (CdSe)ZnS quantum dots (QDs) are luminescent and highly photostable nanocrystals with dimensions smaller than about 10 nm.[1] Their band gap increases when the size of the particle decreases due to quantum confinement effects[2] which produces distinctive size dependent photophysical properties that have received much attention recently.[3,4] Their potential for biophysical studies was confirmed in late 1998 in experimental applications that demonstrated that semiconductor nanocrystals could be made biocompatible and used as photostable fluorescent probes to study biomolecules within living cells.[5,6] However, QDs also exhibit fluorescence emission intermittency (so called QD blinking),[7] and this photophysical property limits quantitative application of these nanoparticles for certain biophysical applications. The blinking cannot easily be blocked or attenuated under cell physiological conditions, and the variations in fluorescence emission complicate the interpretation of analytical techniques, such as correlation spectroscopy, that rely on intensity as a reporter of particle mobility. In certain techniques, the blinking can fundamentally limit the statistics of individual measurements, such as in fluorescence microscopy based single particle tracking (SPT), where a switch to a dark 'off' state leads to an abrupt termination of tracking of the QD tagged macromolecule of interest.[8] Nevertheless, trajectories in which QDs remain 'on' for long durations can be selected to ensure accurate and precise determination of mobility coefficients by SPT. On the other hand, in correlation spectroscopy studies of diffusion, the measurement is ultimately based on statistical analysis of fluorescence fluctuations, so systematic errors cannot be avoided if blinking is not appropriately modeled. [9] Mathematical models have been developed that incorporate the effects of probe blinking into correlation spectroscopy theory. These have been applied in fluctuation spectroscopy experiments that use certain organic dyes and fluorescent proteins which exhibit single exponential blinking kinetics with a single characteristic fluctuation time scale.[10, 11] However, the major challenge in adapting the correlation spectroscopy methods for QD blinking is that intermittency periods follow power law statistics with contributions over many orders of magnitude in time,[12] so the single state blinking models cannot be applied.

To date, characterization of blinking in QDs has relied on the measurement of the probability distribution function through histogram binning of the 'on' and 'off' durations for fluorescence intensity time traces recorded from single QDs .[7,12,13] Several theoretical studies have derived mathematical models for the correlation function decay of blinking phenomena with power law statistics,[14,15] but these have not been applied in confocal microscopy or other highly-sensitive optical experimental studies. Although there have been a large number of studies on blinking dynamics in quantum dots, a full understanding of how it affects fluorescence correlation measurements is still lacking.

In this TIRF-ICS time series study, we characterize the blinking of an ensemble of spatially resolved immobile QDs on a glass substrate to restrict the measured fluctuations to those from the QD intermittency. We determine the ensemble intensity correlation function of the ‘blinking’ process at various laser excitation powers. We show that the improved sampling inherent in the combined spatial and temporal image correlation analysis allows us to characterize QD blinking statistics from relatively short (< 1 minute) image time series. We verify that the variation in blinking statistics is indeed reflected in the measured ensemble correlation function by analyzing simulations of spatially distributed point emitters with set blinking power laws. As well, we determine the limits of temporal sampling and the necessary number of QDs imaged that are needed for accurate and precise measurement of the blinking statistics using ICS.

4.2 Experimental Method

We used streptavidin functionalized (CdSe)ZnS quantum dots (QD605-streptavidin, Quantum Dot Corp. Hayward, Ca) with emission wavelength centered at 605 nm. The QD samples were sonicated for 15 min and then deposited on freshly cleaned coverslips prior to use. Microscope coverslips (Fisher Scientific) were rinsed with ethanol, boiled in 1:1 mixture of chloroform and ethanol for 15 min, then rinsed again with copious amounts of ethanol and deionized water, and blown dry under nitrogen gas. Solutions of the QDs in water were deposited immediately on the dried glass coverslips. Excess QD solution was removed by nitrogen flow shortly after deposition to prevent formation of aggregates on the surface of the glass due to cohesion forces during the drying process.

We used objective type total internal reflection fluorescence microscopy (TIRFM) for time series imaging of the QDs on the glass substrates. The TIRFM apparatus, shown in Fig. 1, was custom built around a Zeiss Axiovert S100TV inverted microscope using an optical setup similar to that of M. Paige et al.[16] The 488 nm line from a CW Ar^+ laser (Melles Griot 35 LAP 431) was used for evanescent excitation through a Zeiss Planapo 100x 1.45 NA objective lens. The excitation power was attenuated using neutral density (ND) filters. Fluorescence from the sample plane was filtered with an emission filter centered at 605nm with bandwidth of 55nm (Croma Technology, Rockingham, VT). Image time series were recorded using an intensified PentaMax CCD camera (Princeton Instruments, Trenton, NJ) with 50 ms integration time and 25 ms readout time so that the time between images is 75ms.

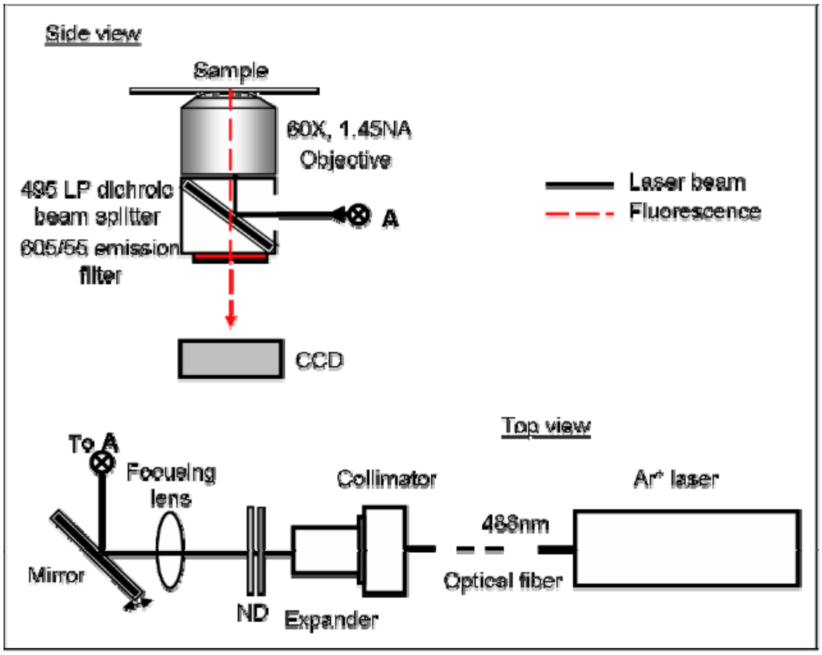

Figure1

Experimental set-up scheme.

During the collection time and during the readout time the dots are blinking. Due to the self similarity property of Levy statistics, the information, which is not accounted for during the readout time does not alter the on and off probability distribution exponents. To confirm that, we conducted experiments with integration to readout time ratios varying from 0.4 to 28 and obtained similar results (data not shown).

Computer simulations of image time series of ensembles of spatially resolved blinking point sources were run using programs written in Interactive Data

Language (IDL 6.0, RSI Colorado). Random pixel positions were selected for the point source particles according to a set particle number variable. Each pixel was then convolved with a 2D Gaussian function of 0.3 μm e^{-2} radius to simulate the spatial form of the detected point fluorescence emission profile due to the point spread function (PSF) of the optics. The 'on' and 'off' time durations were governed by inverse power laws with set variable exponents that were produced using the transformation method of uniformly distributed random numbers: [17]

$$P(t_{On/Off}) \propto \frac{1}{t_{On/Off}^{m_{On/Off}}} \tag{1}$$

Since the power-law decays for exponents greater than one are non-integrable near the origin, we chose the time step between images, Δt as the minimum dwell time of the 'on' or 'off' state while infinitely long 'on' and 'off' times were allowed. The 'off' time distribution exponent, m_{Off} was set to 1.5, while the 'on' time distribution exponent, m_{On} was varied from 1.5 to 1.9. The choice of exponents was based on observed experimental values for capped (CdSe)ZnS quantum dots .[13,18,19] CCD camera integration and readout time were not simulated.

The discrete normalized ensemble intensity autocorrelation function for an image time series was calculated as follows: [20]

$$\mathrm{r}(\mathrm{s}) = \frac{1}{\mathrm{N-s}} \sum_{\mathrm{q=1}}^{\mathrm{N-s}} \frac{1}{\mathrm{M_1 M_2}} \sum_{\mathrm{x=1}}^{\mathrm{M_1}} \sum_{\mathrm{y=1}}^{\mathrm{M_2}} \frac{\mathrm{i(x,y,q)\,i(x,y,q+s)}}{\langle \mathrm{i} \rangle_{\mathrm{c}} \langle \mathrm{i} \rangle_{\mathrm{c+s}}} \tag{2}$$

where s is the discrete image lag variable and is evaluated in integer steps from $s = 0$ to N-1, M_1 and M_2 are the number of pixels in the horizontal and vertical dimensions of a rectangular planar analyzed subregion of interest in the image, and N is the total number of images in the time series. The $<i>_{c \text{ or } c+s}$ indicates spatial averaging of the intensity across the subregion in image c or c+s respectively. This discrete approximation to the temporal lag autocorrelation function ($r(\tau)$) was obtained by simply converting the discrete image lag independent variable, s, to a discrete time lag: $\tau = s\,\delta t$ where δt is the time step between sequential image frames.

4.3 Results and Discussion

A TIRF image of immobilized and spatially resolved streptavidin functionalized capped (CdSe)ZnS QDs is presented in Fig. 2a. The fluorescence intensity imaged on the CCD from spatially distributed QDs on the substrate follows an extended 2D Gaussian intensity profile characteristic of evanescent field illumination. The normalized ensemble intensity time correlation functions of blinking QDs were calculated from time series stacks of 15 by 15 μm^2 area, selected from the central region of the image series as highlighted in Fig. 2a.

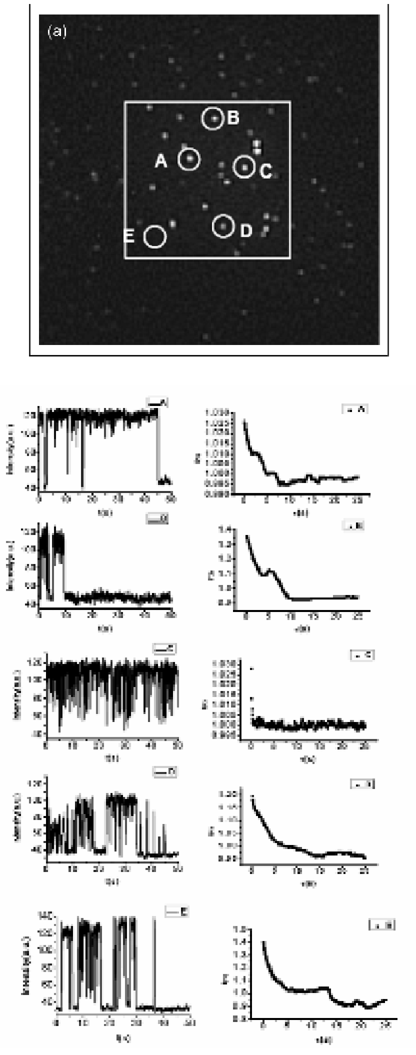

Figure 2

(a) TIRFM image of streptavidin functinonalized (CdSe)ZnS QDs immobilized on a glass coverslip. (b)Intensity time traces of selected individual QDs. (c) Corresponding normalized intensity time correlation function of single QDs intensity time trace presented in (b).

In this region, the extended Gaussian illumination profile decays by less than 10 % in intensity at the periphery as determined from the signal obtained from fluorescent dye uniformly spread on a glass coverslip. Single pixel intensity traces selected from the centroids of the highlighted QDs from Fig. 2a are presented in Fig. 2b and the corresponding single trace intensity autocorrelation functions in Fig. 2c. Figure 2 illustrates some of the problems inherent in single dot intensity correlation analysis for the case when there is limited time sampling. Clearly, for dots A and B, the autocorrelation decays reflect the step function like behavior of the intensity traces, and effective under sampling of the distributions. The autocorrelation functions are disproportionately affected by the long ‘on’ time in case A, and the long ‘off’ time in case B. It is not possible to accurately fit such autocorrelation functions and they would have to be excluded from the analysis. Quantum dot C produces a signal that fluctuates rapidly in time so long time correlation is absent. In this case, the autocorrelation function decays too rapidly as no long time blinking events are sampled. The autocorrelation functions for dots D and E can be accurately fit and analyzed as the parent intensity time traces contain a (random) sampling of blinking events over a range of time scales. We find that in cases where time sampling is necessarily limited, careful selection of intensity traces must be exercised to obtain accurate results from intensity autocorrelation analysis of single QDs. This result is not surprising considering the long integration times (> 10 min) employed in previous single dot histogram studies of QD blinking properties.[12,13] However, it is important to note that this type of data selection is difficult to perform without introducing experimental bias into the analysis.

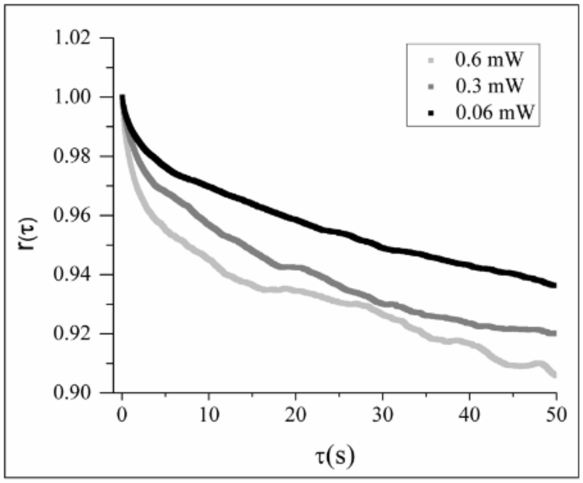

Figure 3

Normalized intensity time correlation functions for various laser excitation powers as calculated from 2000 frame image time series with 50ms/frame integration time for blinking streptavidin functionalized (CdSe)ZnS QDs on a glass substrate. 0.06mW(■) and 0.3mW(■) and 0.6mW(■) excitation laser powers. Intensity correlation functions are normalized to 1 for comparison.

In contrast, we find that for these inherently short sampling times, the ensemble ICS analysis can be performed without excluding any of emitters, and we obtained results that accurately reflect the underlying distribution of on and off blinking times.

In ensemble analysis of streptavidin functionalized (CdSe)ZnS QDs on a glass substrate, the observed normalized intensity time autocorrelation functions are slowly decaying power laws with no single characteristic decay time (Fig. 3). The same type of decay was observed for the intensity time autocorrelation functions of non functionalized single capped (CdSe)ZnS quantum dots and interpreted qualitatively based on the fact that in capped (CdSe)ZnS quantum dots, the ‘on’ and ‘off’ time durations follow inverse power law distributions.[21] ‘On’ times on the order of the total measurement time are likely to occur for a fraction of quantum dots. They will appear as long range correlations in the correlation function causing it to decay slowly over the time scale of the measurement, as is observed in Fig. 3. The intensity autocorrelation functions presented in Fig. 3 show an increased rate of decay at higher excitation laser intensities as a result of the shorter ‘on’ events observed at high laser powers.[22]

To quantify the rate of decay of the ensemble time autocorrelation functions, we fit using a three parameter power law:

$$r(\tau) = A - B\tau^{\alpha} \qquad (3)$$

where A, B and α are the fitting parameters. We use the fitting exponent α as a measure of the rate of decay of the correlation function since it reflects the underlying 'on' and 'off' time distribution exponents. The coefficients A and B depend on the underlying blinking statistics as well as the average on time of the ensemble of QDs. An explicit dependence of these parameters on the fitting exponents has been proposed by Verberk and Orrit who model the non-normalized intensity correlation function of capped (CdSe)ZnS QDs.[23] It is worth noting that their model applies to the intensity time correlation function of a single QD, whereas our correlation functions are calculated for an ensemble of QDs. The distinction is of relevance given the non-stationary and non-ergodic properties of power law distributions, where the average 'on' time of an ensemble of blinking QDs is time dependent and doesn't correspond to the average 'on' time of a single QD calculated with infinite collection time. These properties greatly complicate the derivation of closed form analytical expressions for theoretical single dot and ensemble correlation functions. Margolin and Barkai have presented full theoretical treatments of the non-ergodic properties of time averaged correlation functions in single QDs[15] and the aging properties of correlation function in ensembles of QDs.[14] However, our experimental results show that for the sampling regimes we explored, the ensemble intensity autocorrelation function decays of protein functionalized capped (CdSe)ZnS QDs are well modeled by the simple three parameter power law.

A plot of the mean recovered α exponent as a function of laser power is presented in Fig. 4. We observe a decrease in α from 0.46 ± 0.08 at 0.01 mW laser power to 0.18 ± 0.05 at 0.6 mW. We also found that the ensemble autocorrelation function cannot be properly fit by the three parameter power law (Eq. 3) outside of this range of excitation power.

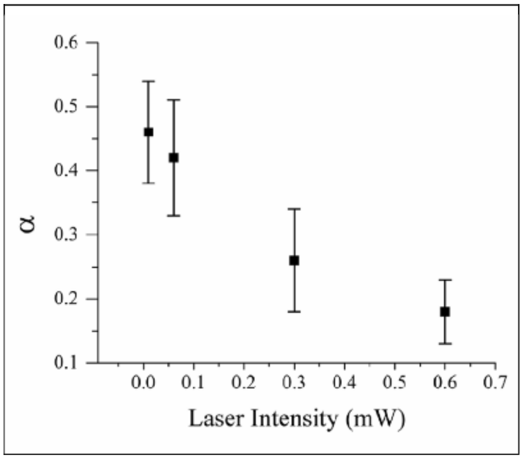

Figure4

Plot of α as a function of laser power. Each value is an average from 15 measurements. Error bars are standard deviations.

At powers lower than 0.06 mW, longer ‘on’ events dominate and remain correlated over the time scale of the measurement resulting in a correlation function which barely decays. At powers higher than 0.6 mW, the opposite effect is observed and the correlation function rapidly decays and the autocorrelation function cannot be modeled by a slowly decaying power law. The latter case is a possible explanation as to why the correlation functions of single CdSe QDs in the study reported by Kobistski et al. fail to fit to Verberk and Orrit's power law decay model.[24] In that study the absence of a passivating ZnS shell reduced the observation of long 'on' time events. It is important to stress that the measured α exponent values reported at different laser intensities, and the autocorrelation function decay model may differ depending on the type of functionalization of (CdSe)ZnS QDs.

We compared our experimental results to computer simulations to model what is expected for pure power law decays and to probe the precision and detection limits of the ICS method. By performing ICS analysis on simulated image time series of point emitters blinking according to set power law distributions, we tested the sensitivity of the method as a function temporal sampling and of number of emitters sampled.

The normalized intensity time autocorrelation functions calculated from the simulated image time series decay as slow power laws (see Fig. 5) as is expected based on the set distribution parameters for the simulation. A qualitative comparison of Fig. 3 and Fig. 5 shows that the experimental autocorrelation decays compare well with the autocorrelation functions from the simulations.

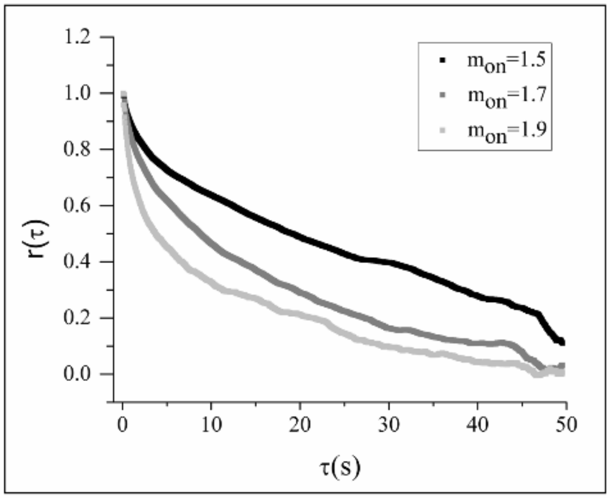

Figure 5

Normalized intensity correlation functions calculated from 1000 frames simulated image series with an image time step of 0.05s. Each image consists of 300 point emitters. The ‘Off’ time probability distribution exponent is 1.5 for all simulated image series. The ‘On’ time distribution exponents are 1.5 (■), 1.7 (■) and 1.9(■) respectively.

Changes in the set ‘on’ time distribution exponents for the simulations are directly reflected by changes in the rate of decay of the calculated ensemble autocorrelation functions. In distributions with larger exponents, short ‘on’ times dominate, causing the correlation function to decay more rapidly; an effect similar to what is observed at high laser excitation intensities. We use Eq. 3 to fit the ensemble correlation functions and recover the best fit exponent parameter α.

Table I presents a summary of the exponent α determined by ensemble correlation analysis from image time series simulations with 1000 frames, m_{On} values ranging from 1.5-1.9, and for different numbers of blinking point emitters within the ensemble. The recovered α values from the simulations show that the image correlation method is sensitive to changes in the power law distribution exponents, but the sensitivity and precision of the measurement is dependent on the total number of emitters sampled.

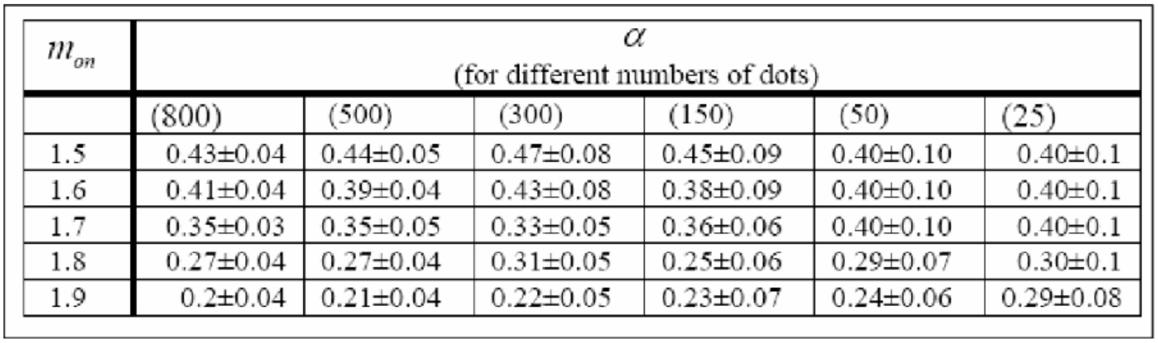

m_{on}	α (for different numbers of dots)					
	(800)	(500)	(300)	(150)	(50)	(25)
1.5	0.43±0.04	0.44±0.05	0.47±0.08	0.45±0.09	0.40±0.10	0.40±0.1
1.6	0.41±0.04	0.39±0.04	0.43±0.08	0.38±0.09	0.40±0.10	0.40±0.1
1.7	0.35±0.03	0.35±0.05	0.33±0.05	0.36±0.06	0.40±0.10	0.40±0.1
1.8	0.27±0.04	0.27±0.04	0.31±0.05	0.25±0.06	0.29±0.07	0.30±0.1
1.9	0.2±0.04	0.21±0.04	0.22±0.05	0.23±0.07	0.24±0.06	0.29±0.08

Table 1

Summary of the mean fitting exponent α for the normalized intensity correlation functions of simulated image time series with different m_{On} values and for different number of dots ranging from 800 to 25. m_{Off} is set to 1.5. Number of blinking point emitters is included in brackets. Each α value is an average from 20 simulations. Uncertainties are standard deviations.

For example, we observe an average 50% decrease in the standard deviation of the mean recovered α exponent when the number of point emitters within the ensemble increases from 50 to 500. Also, ensembles containing more point emitters are more sensitive to variations in underlying blinking dynamics due to the improved sensitivity and precision of the recovered α exponent.

We found that an increase in temporal sampling improves the sensitivity of the ICS method and can be used to improve the measurement resolution for ensembles containing small numbers of point emitters. The results in Table 2 show that for a system of 150 point emitters, increasing the temporal sampling from 100 to 10 000 image frames results in an average 14% decrease in the standard deviation on the mean recovered α exponent.

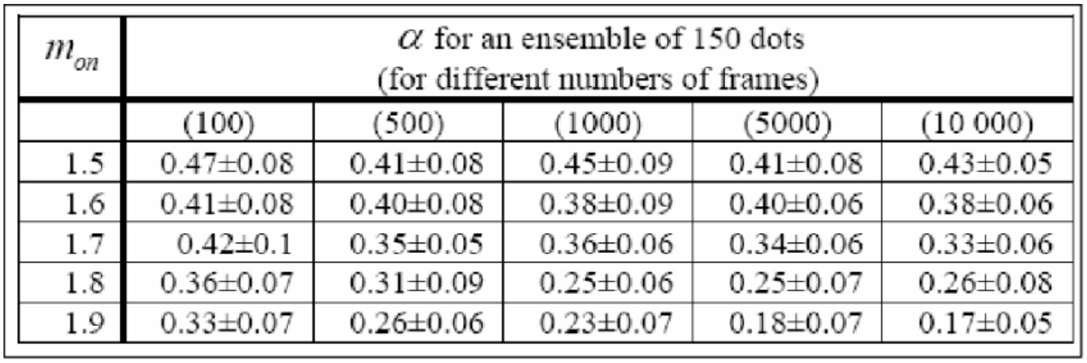

m_{on}	α for an ensemble of 150 dots (for different numbers of frames)				
	(100)	(500)	(1000)	(5000)	(10 000)
1.5	0.47±0.08	0.41±0.08	0.45±0.09	0.41±0.08	0.43±0.05
1.6	0.41±0.08	0.40±0.08	0.38±0.09	0.40±0.06	0.38±0.06
1.7	0.42±0.1	0.35±0.05	0.36±0.06	0.34±0.06	0.33±0.06
1.8	0.36±0.07	0.31±0.09	0.25±0.06	0.25±0.07	0.26±0.08
1.9	0.33±0.07	0.26±0.06	0.23±0.07	0.18±0.07	0.17±0.05

Table 2

Summary of the mean fitting exponent α for the normalized intensity correlation functions of simulated image time series for an ensemble containing 150 point emitters with different m_{On} values and for different number of frames ranging from 100 to 10000. m_{Off} is set to 1.5. Each α value is an average from 20 simulations. Uncertainties are standard deviations.

In the sampling regimes we investigated, the temporal sampling has a much smaller influence on the precision of the measurements. In comparing the results for ensembles containing 800 and 150 point emitters in Tables 1 and 2, we note that more than an order of magnitude increase in temporal sampling is required to achieve the same sensitivity of resolution of the measured α value as is achieved with a five fold increase in the number of point emitters sampled. For small ensembles containing less than 50 blinking point emitters, we increased the temporal sampling to 100,000 frames in the simulated image time series, but were not able to resolve changes in α, and hence were unable to detect variations in the blinking dynamics (data not shown).

The conclusions drawn from our results are important for fluorescence intermittency studies in different types of QDs or other fluorescent molecules with underlying power law blinking statistics. Many studies of fluorescence intermittency rely on the measurement of a time correlation function from intensity time traces of single molecules for use as a statistical tool to characterize the photophysical processes underlying the observed fluorescence dynamics.[25,26] A single molecule approach is adopted for these studies due to its sensitivity to dynamic and population heterogeneities that are often masked by the averaging inherent in the ensemble approach. However, to characterize variations in blinking dynamics in QDs through correlation analysis with limited time sampling, a single molecule approach could not be used. Instead, measurements should be done on ensembles of QDs. We showed in Fig 2 that the single dot time correlation functions of some of the QDs in the sample could be fit by a three parameter power law. However, changes in the underlying blinking dynamics could not be resolved due to the large dot to dot variation in the recovered alpha exponent. Even for long imaging times, there exists a minimum lower bound on the size of the ensemble required to resolve variations. Power spectral measurement of blinking QDs has shown that ensemble measurements can provide the same information on blinking statistics as do single dot measurements.[27] We further investigated the effect of temporal sampling and the number of point emitters in ensemble correlation measurements and demonstrated that the ability to resolve blinking distribution changes depends on the number of dots in the ensemble as well as the extent of temporal sampling.

Our simulation results support the conclusion that we were able to experimentally resolve differences in the underlying blinking statistics of the QDs via ICS measurement of the α exponent. The standard deviation on the α value decreases at higher laser intensities and the same trend is observed in simulations with large 'on' distribution exponents. The results shown in Fig. 4 demonstrate that we can resolve changes in α as a function of laser power. Using the simulation results, we were able to confirm that these measurements were performed in a suitable sampling regime. The experimental results shown in Fig. 4 were obtained from systems containing approximately 100 emitting QDs in the analyzed area. Atomic force microscopy (AFM) measurements performed on the analyzed regions of the samples confirm that there are approximately 250

QDs within these areas, of which, on average 100 are fluorescently active as determined from the extracted fluorescence intensity traces (data not shown). The number of emitting QDs in Fig. 2 appears to be significantly less than 100 due to the significant fraction of QDs being in a dark state in the selected time series image frame.

In this study we measured systems with well separated (optically resolved) nanoparticles. The probability for a transition to a dark state in a QD is related to the distribution of trap states in its surroundings and the rate of formation of localized electron-hole pairs.[28] The latter is dependent on the excitation intensity. We assume that the distribution of trap states around the spatially separated QDs is constant on average, and use the variable excitation laser intensity as a tool to change underlying ‘on’ time distribution. As our studies were conducted on systems where single QDs were optically resolved, we can be certain that our fluorescence measurements do not include contributions from resonance energy transfer or the absorption of energy from neighboring QDs due to recombination of high energy excitons. This density regime places a limit on the number of QDs that can be present in the sample. We can estimate 450 as the maximum number of QDs in a 64 x 64 pixels^2 area if we assume that fluorescence from a single dot spreads over an image area of 3 x 3 pixels^2. Direct application of the same analysis technique is possible for higher density samples where QDs are not fully spatially resolved as long as the QDs are not in very close proximity (< 10 nm) of each other and is the subject of our future work.

Conclusion

In conclusion, we characterized the ensemble intensity time correlation function of blinking QDs using TIRF–ICS and computer simulation models. We show that the correlation function can be fit to a three parameter power law. The change in the rate of the decay of the correlation function is a measure of the change in the underlying ‘on’ time distribution. We found that detection of changes in the blinking distribution critically depend on adequate sampling, and was most sensitive to the total number of emitters in the ensemble. We emphasize that the ensemble ICS method can successfully characterize blinking dynamics in cases where temporal sampling is limited. Thus, it will be important to account for the blinking in future studies that employ ICS to measure mobility of QD labeled macromolecules in cellular systems. This study provides a basis for extending ICS mobility experiments to systems that employ QD labels where blinking fluctuations will be present.

Based on this work, we expect to be able to measure changes in the blinking of QDs as a function of other environmental parameters apart from laser intensity. It has been previously shown that, due to their intrinsic sensitivity to the surrounding chemical environment, modifications of the surface interface of nanocrystals significantly affect their photophysical properties.[19, 29] Moreover, recent reports suggest that reducing agents affect quantum dot blinking,[30] further suggesting that this process may be modulated and exploited for the development of sensing technologies. Thus, accurate characterization of the variation in the blinking dynamics under controlled experimental conditions is of particular relevance to future applications utilizing fluorescence of QD nanoparticles for sensing purposes.

References:

[1] M.A Hines, P Guyot-Sionnest., J. Phys. Chem. 100,468 (1996).

[2] M. Nirmal , L. Brus, Acc. Chem. Res. 32, 407 (1999).

[3] D. J. Norris, M. G. Bawendi, Phys. Rev. B 53, 24 (1996).

[4] X. Michalet, F.F. Pinaud, L.A. Bentolila, J.M. Stay, S. Doose, J.J. Li, G. Sundaresan, A.M. Wu, S.S. Gambhir, and S.Weiss, Science 307, 538 (2005).

[5] M. Bruchez, M. Moronne, P. Gin, S.Weiss, A.P. Alivisatos, Science 281, 2013 (1998).

[6] W.C. Chan, S. Nie, Science 281, 2016 (1998).

[7] M. Nirmal, B.O. Dabbousi, M.G. Bawendi , J.J.Macklin, J.K. Trautman , T.D. Harris , and L.E. Brus Nature (London) 383, 802 (1996).

[8] M. Dahan, S. Levi, C. Luccardini, P. Rostaing, B. Riveau, and A. Triller, Science 302, 442 (2003).

[9] S. Doose, J.M. Tsay, F. Pinaud, S. Weiss, Anal. Chem. 77, 2235 (2005).

[10] J. Widengren, U. Mets, R. Rigler, J.Phys. Chem. 99, 13368 (1995).

[11] P. Schwille, S. Kummer, A.A. Heikal, W.E Moerner, W.W. Webb, PNAS 97,151(2000).

[12] M. Kuno, D.P. Fromm, H.F. Hamann, A. Gallagher, D.J. Nesbitt, J. Chem. Phys. 112, 3117 (2000).

[13] M. Kuno, D.P. Fromm, H.F. Hamann, A. Gallagher, D.J. Nesbitt, J. Chem. Phys. 115 1028 (2001).

[14] G. Margolin, E. Barkai, J.Chem.Phys. 121, 1566 (2004).

[15] G. Margolin, E. Barkai, Phys. Rev. Lett. 94, 080601 (2005).

M.K. Kuno, D.P. Fromm, H.F. Hamann, A. Gallagher, and D.J. Nesbitt, J. Chem. Phys. 115, 1028 (2001).

[16] M.F. Paige, E.J. Bjerlend, and W.E. Moerner, Single Molecules 2, 191(2001).

[17] W.H. Press, B.P. Flannery, S.A. Teukolsky, and W.T. Vetterling, Numerical Recipes in C: The Art of Scientific Computing (Cambridge University Press, Cambridge, England, 1993), 2nd ed.

[18] W.G.J.H.M.van Sark, P.L.T.M. Frederix, A.A. Bol, H.G. Gerritsen, and A. Meijerink, ChemPhysChem 3, 871 (2002).

[19] R. Verberk, J.W.M. Chon, M. Gu, and M.Orrit, Physica E 26, 19 (2005).

[20] P.W. Wiseman, J.A. Squier, M.H. Ellisman, and K.R. Wilson, J. Microsc. 200, 14 (2000).

[21] G. Messin, J.P.Hermier, E. Giacobino, P. Desbiolles, and M. Dahan, Opt. Lett. 26, 1891 (2001).

[22] K.T. Shimizu, R.G. Neuhauser, C.A. Leatherdale, S.A. Empedocles, W.K. Woo, and M.G. Bawendi, Phys. Rev. B 63, 205316 (2001).

[23] R. Verberk and M. Orrit, J. Chem. Phys. 119, 2214 (2003).

[24] A.Y. Kobitski, C.D. Heyes, G.U. Nienhaus, Appl. Sur. Sci. 234, 86 (2004).

[25] K.D. Weston, P.J. Carson, H. Metiu, and S.K. Buratto , J. Chem. Phys. 109, 7474 (1998).

[26] R.M. Dickson, A.B. Cubitt, R.Y. Tsien, and W.E. Moerner*,* Nature 388, 355 (1997).

[27] M. Pelton, D.M. Grier, and P. Guyot-Sionnest, Appl. Phys. Lett. 85, 819 (2004).

[28] I.S. O’sad’ko, JERP Lett. 79, 416 (2004).

[29] S. R. Cordero, P. J. Carson, R. A. Estabrook, G. F. Strouse, and S. K. Buratto, J., Phys. Chem. B 104*,* 12137(2000)

[30] Sungchul Hohng and Taekjip Ha, J. Am. Chem. Soc. 126, 1324 (2004)

Correlation based techniques such as fluorescence correlation spectroscopy (FCS), image correlations spectroscopy (ICS) and their variants are widely used as quantitative analysis techniques in biophysics. They measure fluorescence fluctuations due to changes in fluorophore occupation number within a microscopic observation volume of a sample defined by the focus of a laser beam and provide information on the transport dynamics of the labelled macromolecules in the system. Most organic dyes and fluorescent proteins have intermittent emission that introduces an additional source of correlated fluctuations, but they usually have single exponential blinking statistics which can be accounted for in the correlation analysis. QDs do not have a characteristic fluctuation time scale due to the power law nature of the fluorescence blinking. In the previous chapter we showed that image correlation analysis can be used to distinguish different blinking distribution regimes for immobilized QDs. Since in most biologically relevant studies the fluorescently labelled macromolecules of interest are mobile (or at least a fraction of the population is mobile), in the next chapter we examine how blinking affects mobility parameters recovered from correlation analysis and investigate a new approach for dealing with the luminescent blinking for such mobility studies.

Chapter 5

5. Detection and Correction of Blinking Bias in Image Correlation Transport Measurements of Quantum Dot Tagged Macromolecules

Reprinted with permission from:
Detection and correction of blinking bias in image correlation transport measurements of quantum dot tagged macromolecules, N. Durisic, A. I. Bachir, D. L. Kolin, B. Hebert, B. C. Lagerholm, P. Grutter, P. W. Wiseman, Biophys. J. 93: 1338-1346 (2007)

5.1 Introduction

Fluorescence microscopy is the most commonly used method for imaging studies of dynamic processes in living cells, moreover, fluorescence based biophysical methods are also widely employed. Consequently, there has been much research devoted to developing novel fluorescent probes for these types of applications. Advances in nanoscience have led to the development of photostable luminescent semiconductor nanocrystals or quantum dots (QDs) that have been touted as superior probes for biological imaging applications (1-3). The QDs typically consist of an inorganic semiconductor core and shell (e.g., CdSe/ZnS) with an outer organic coating for water solubility and biocompatibility. Recent improvements in QD synthesis and surface functionalization strategies have made the conjugation of quantum dots to various biomolecules more feasible, thus increasing their applications to cell and animal biology (4-8). Some of the photophysical properties of QDs are superior to conventional organic fluorophores. In particular, their broad absorption spectra and high quantum yields make them significantly brighter than many common fluorescent dyes (9), while their greater photostablity permits longer observation times than conventional organic fluorophores (10, 11). Additionally, experiments have shown that QDs have very large two-photon absorption cross-sections which make them promising labels for multiphoton microscopy applications (12).

These photophysical properties of luminescent nanoparticles would also be advantageous for optimizing fluorescence fluctuation measurements of macromolecular transport coefficients using techniques such as fluorescence correlation spectroscopy (FCS) and its imaging analog temporal image correlation spectroscopy (TICS) (13-16). In fluorescence fluctuation methods, the signal-to-noise ratio increases as the number of fluorescence photons emitted per molecule per second increases (17, 18) so having a label with a large quantum yield and absorption cross-section is desirable. The enhanced photostability of the QDs is also advantageous for fluorescence fluctuation measurements because photobleaching of the fluorophore can lead to systematic errors in transport coefficients measured by temporal correlation analysis (19).

However, the photophysics of QDs is also characterized by non-stationary emission or fluorescence intermittency that is commonly referred to as luminescent “blinking” (20). As techniques such as FCS and TICS measure molecular transport parameters by temporal correlation analysis of fluorescence fluctuations, it is not surprising that the blinking emission of QDs will contribute to the decay of the calculated time correlation function (21, 22). The usual goal of an FCS or TICS experiment is to measure the transport coefficients of a labeled macromolecule by correlation analysis of the detected fluorescence fluctuations arising from changes in the number of fluorophores in a laser beam focus as the macromolecules move in and out of the focal region (see Fig. 1A and B). However, the luminescent blinking of the QDs will contribute additional fluctuations to the intensity time record (Fig. 1B).

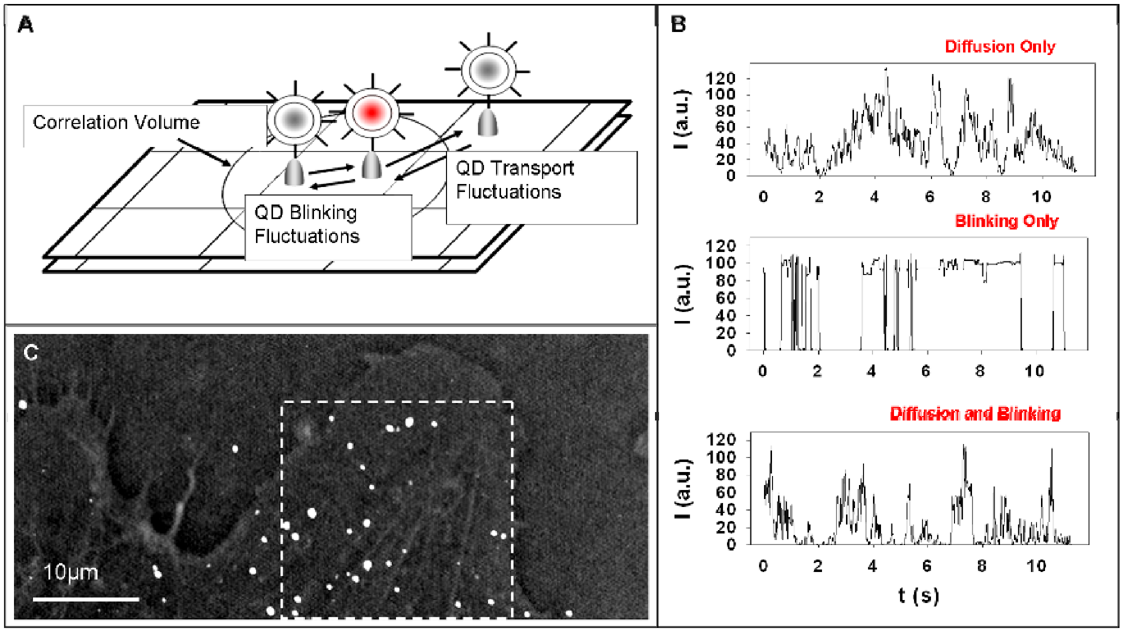

Figure 1

Schematic representation of the correlation volume on an area detector. Fluorescent fluctuations due to quantum dot mobility cannot be distinguished from blinking since they both result in a change in the signal level from the correlation volume.

(B) Intensity time traces of a single pixel from three different simulations: in the first simulation fluorescent particles were diffusing in two dimensions but blinking was absent, in the second particles with power law blinking were immobilized and in the third simulation fluorescent particles were diffusing and blinking. All simulations contained 500 images, each with an image area of 128 x128 pixels and temporal sampling of 10 frames/s. The diffusion coefficient was set to 0.1μm^2/s and the PDF blinking exponent was m_{on} =1.5.

(C) Superimposed DIC and fluorescence image of CD73 protein labeled with quantum dots in the basal membrane of a fibroblast. The subregion analyzed is outlined in white. It contained 1798 images collected at the video rate.

In principle, it is possible to model the decay of time correlation function by including kinetic terms that incorporate the contributions of all microscopic processes that contribute fluorescence fluctuations on the time scale of the sampling (23). However, unlike many organic dyes (24) and fluorescent proteins (25) (where similar blinking fluctuations have exponential kinetics with time constants usually one order of magnitude smaller than the characteristic molecular diffusion time) QD blinking is especially difficult to separate from other fluctuations of interest since the probability distribution function (PDF) of the “on” and “off” blinking time durations has a form of inverse power law (26, 27):

$$P(t_{On/Off}) \propto \frac{1}{t_{On/Off}^{m_{On/Off}}} \quad . \qquad (1)$$

This power law distribution entails that fluctuations due to blinking will occur over many time scales, and this prevents any characteristic correlation time from being linked with the blinking emission via correlation analysis. We thus predict that QD blinking will contribute a systematic error to mobility measurements made by TICS depending on the actual PDF of the nanoparticle blinking.

In Ch 4, we showed that the blinking of static QDs immobilized on glass substrates could be studied by TICS to characterize the decay rates of blinking autocorrelation (22). In this chapter, we show that fluctuations due to luminescent blinking of the QDs will systematically bias transport measurements made by TICS when such nanoparticles are employed as labels. Using a model system of QDs diffusing between two cover slips in a glycerol medium, we were able to obtain total internal reflection fluorescence microscopy image time series with different laser excitation powers to systematically adjust the exponent of the blinking power law (20, 28). Analysis of these image series by TICS illustrated that the change in blinking clearly affected the correlation function decay; moreover, a simple 2D diffusion model fit the decays well, but yielded different characteristic diffusion times for the different excitation powers. The experimental results were corroborated by computer simulations of image series of blinking/diffusing point emitters where the blinking, transport, and collection conditions were systematically controlled. The experimental and simulation image series were also analyzed using the new k-space image correlation spectroscopy (kICS) which separates the contributions of fluctuations due to photophysics from those due to transport (29). We show that the transport coefficients can be accurately recovered by kICS without the systematic and hidden bias of the photophysical fluctuations that perturb the temporal image correlation. Finally we demonstrate the application of TICS and kICS to measure the diffusion of a GPI-anchored protein, CD73, in the membrane of IMR-90 fibroblasts and compare the results to those obtained for the model system and the simulations.

5.2 Materials and methods

5.2.1 Model Sample Preparation

Streptavidin functionalized (CdSe)ZnS quantum dots (QD605-streptavidin, Invitrogen Canada Inc. Burlington, ON) with emission wavelength centered at 605 nm were used in all model system experiments. We prepared sample chambers for the model diffusive transport measurements by etching 100 nm deep wells in 10 mm x 10 mm glass cover slips (Fisher Scientific, Ottawa, ON). Prior to use, all cover slips were boiled in a 1:1 ethanol and chloroform mixture for 30 min, rinsed with copious amounts of milliQ water and treated with 30% bovine serum albumin (BSA) solution (Sigma Aldrich, Oakville, ON) as a blocking step to reduce nonspecific adhesion of the QDs to the glass. Stock QD solution was first diluted by a factor of 107 in milliQ water and mixed with glycerol so that the final density was approximately 150 quantum dots per 1 µL of glycerol water mixture. The mixture was then sonicated for 30 min before being deposited on the etched wells. A second coverslip was placed on top to close the wells and the assembly was sealed and mounted on a microscope slide for fluorescence imaging. These samples provided a reasonable model for 2D diffusion because the QDs diffused within the 100 nm wells and were imaged by TIRF with an ~100 nm depth of field.

5.2.2 Total Internal Reflection Fluorescence Microscopy (TIRF) Imaging

All fluorescence microscopy measurements on the model QD samples were conducted on a home built total internal reflection microscope described in detail previously (22). The samples were mounted on an inverted microscope (Zeiss Axiovert S100TV, Jena, Germany) equipped with a Zeiss Planapo 63x 1.45 NA oil immersion objective lens and illuminated by through objective evanescent mode with the 488 nm line from a CW Ar+ laser (Melles Griot 35 LAP 431, Ottawa, ON). The excitation power was attenuated using neutral density (ND) filters. A Q 495 Lp dichroic mirror and 605/55nm emission filter combination (Chroma Technology, Rockingham, VT) were used for all measurements. The back collected fluorescence was focused onto an intensified PentaMax CCD camera (Princeton Instruments, Trenton, NJ) with 50-70 ms integration time and 13 ms readout time for imaging. Rectangular sub-regions chosen for correlation analysis were all selected from within the center of the imaged field of view where the evanescent excitation intensity was fairly (~ 10 %) constant.

5.2.3 Computer Simulations

Computer simulated image time series of point emitters were generated using programs written in either IDL (RSI, Denver, CO) or MATLAB R14 (The MathWorks, Natick, MA). The programs placed point emitters at random pixel positions with a set particle density of 6 emitters/µm^2. The particle matrix was convolved with a 2D Gaussian function of defined radius to yield an image matrix. In all simulations, we set the image size either to 64 x 64 or to 128x128 pixels with 0.1 µm pixel diameter and the radius of the Gaussian convolution function was set to 3 pixels (i.e. 0.3 µm). An image time series was generated in which the diffusion coefficients and the on/off emission statistics of the point emitters were input by the user. For diffusion simulations, periodic boundary conditions were used at the image boundaries, and displacements in x and y were computed at every time step for each particle, according to normally-distributed, floating-point, pseudo-random numbers with a mean of zero and a standard deviation of $\sigma = (2D\Delta t)^{1/2}$ where D is the diffusion coefficient and Δt the time step between images. The “on” and “off” time durations for particle emission were randomly selected according to inverse power law probability distributions with a set off time distribution exponent (m_{off}) of 1.5 and on time distributions exponents (m_{on}) varying between 1.5 and 2. The minimum “on” and “off” times were set to the image time step of the simulation and for each set of distribution exponents, we varied the time step between images between 2.25 and 100 ms. The simulation image series were then analyzed by both temporal and k-space image correlation techniques.

5.2.4 Cell Tissue Culture, Labelling and Imaging

IMR-90 human fibroblasts (ATCC) were grown in Dulbecco’s Modified Eagle’s Medium (D-MEM; Invitrogen, Carlsbad, CA) supplemented with 10% fetal bovine serum (FBS), 100 units/mL penicillin, 100 µg/mL streptomycin, and 0.1 mM minimum essential amino acids. One to two days before an experiment cells were plated in 35 mm glass bottom culture dishes (MatTek, Ashland, MA).

Cells in glass bottom dishes were washed in phosphate buffered saline containing 1 mM CaCl2 and 1 mM MgCl2 (PBS). Cells were subsequently stained with 1 mL of 9.5 μg/mL monoclonal mouse anti-human CD73 (clone AD2, kind gift of L. Thompson, Oklahoma Medical Research Foundation, Oklahoma City, OK) and 0.5 μg/mL of the same biotinylated antibody (3.8 biotin/IgG) in PBS with 1% bovine serum albumin (BSA) for 10 minutes. Cells were then washed in PBS and stained with 100 μL of 2 nM steptavidin conjugated 605 nm quantum dots (sAv605-Qdots; Invitrogen, Carlsbad, CA) in PBS with 1% BSA for 1 minute after which a few drops of a biotin blocking solution (Streptavidin/Biotin Blocking Kit, Vector Laboratories, Burlingame, CA) was added to prevent further cross-linking. Cells were then washed 3X in PBS containing free biotin, as before, and finally in D-MEM/F-12 containing 15 mM HEPES but no phenol red (Invitrogen, Carlsbad, CA) additionally supplemented with 10% FBS and free biotin. All of these steps were done at room temperature.

Fluorescence time-lapse movies were acquired on an Olympus IX-81 microscope equipped with a XR/MEGA-10Z ICCD (Stanford Photonics, Palo Alto, CA). We used a 100W Hg-arc lamp and a 460/50 nm excitation filter for exciting the Qdots and a 610/20 nm emission filter (Chroma, Rockingham, VT) for detection. Time-lapse sequences were imaged at 30 frames per second.

5.2.5 Image Analysis

Temporal Image Correlation Spectroscopy (TICS)

For a given image time series, i(x, y, t), we define a temporal intensity fluctuation autocorrelation function:

$$r(0,0,\tau)=\frac{<\delta i(x,y,t)\delta i(x,y,t+\tau)>}{<i(x,y,t)>_t<i(x,y,t+\tau)>_{t+\tau}} \quad (2)$$

where $\delta i(x,y,t)$=i(x, y, t) - <i(x,y,t)>t is the fluorescence intensity fluctuation at pixel location (x, y) in the image recorded at time t, τ is the temporal lag variable and "< >" denote spatial averaging over all pixel positions in an image (16). The temporal autocorrelation decay can be fit by a variety of models depending on the dynamic processes that contribute fluctuations on the time scale of the image sampling. We fit our data to the standard 2D diffusion model (16):

$$r(0,0,\tau)=g(0,0,0)\left(1+\frac{\tau}{\tau_d}\right)^{-1}+g_\infty \quad . \quad (3)$$

The fit parameters are the zero lag amplitude, g(0,0,0), the characteristic diffusion time, τ_d, and an offset, g_∞. The diffusion coefficient, *D*, is calculated from the characteristic diffusion time and the mean beam radius:

$$D = \frac{<\omega_0>^2}{4\tau_d} \quad . \tag{4}$$

The mean beam radius, $<\omega_o>$, is calculated from the beam radii obtained by fitting spatial correlation functions to each image in the series as has been described previously (16).

k-Space Image Correlation Spectroscopy (kICS)

The details of the kICS method were recently published (29). Briefly, a k-space time correlation function, $r_k(k,\tau)$, is obtained by temporal correlation of the image series after 2D spatial Fourier transforms have been calculated for each image:

$$r_k(\mathbf{k},\tau) = \langle \tilde{i}(\mathbf{k},t)\tilde{i}^*(\mathbf{k},t+\tau)\rangle \tag{5}$$

where $\tilde{i}(\mathbf{k},t)$ is the Fourier transform of the image acquired at time t, $\tilde{i}^*(\mathbf{k},t)$ denotes its complex conjugate, and the angular brackets denote temporal averaging in this case. For a system undergoing 2D diffusion, $r_k(k,\tau)$ has the following analytical form:

$$r_k(\mathbf{k},\tau) = N I_0^2 q^2 \langle \Theta(t)\Theta(t+\tau)\rangle \exp\left[-D\tau|\mathbf{k}|^2\right](\Omega(\mathbf{k}))^2 \qquad (6)$$

where D is the diffusion coefficient, q is the quantum yield, N is the number of particles in the image, I_0 is the incident laser intensity, and Ω(k) is the optical transfer function of the imaging system. The fluorescence emission function, Θ(t) (= 1 for on and = 0 for off), does not depend on spatial coordinates and it models the photophysics of the fluorophore assuming that fluorescence emission is independent of other dynamic processes. By dividing r_k(k,τ) by r_k(k,0), and log-transforming, we obtain a point spread function independent k-space time correlation function:

$$\ln\left[\frac{r_k(\mathbf{k},\tau)}{r_k(\mathbf{k},0)}\right] = \ln[\langle \Theta(t)\Theta(t+\tau)\rangle] - D\tau|\mathbf{k}|^2 \, . \qquad (7)$$

For each image series analyzed, D was calculated as follows. First, ln[r_k(k,τ)/ r_k(k,0)] was circularly averaged. Next, a linear regression of ln[r_k(k,τ)/ r_k(k,0)] as a function of $|k|^2$ was performed for each discrete value of τ, yielding slopes of Dτ. Finally, the slope of a linear regression of a plot of these slopes as a function of τ was equal to *D*. Since the diffusion coefficient is calculated independently of fluorescence emission function, the kICS method yields a transport coefficient that is free of systematic errors caused by blinking or other photophysics contributions.

5.3 Results and Discussion

5.3.1 QD Blinking Systematically Affects TICS Transport Measurements

We imaged streptavidin functionalized (CdSe)ZnS quantum dots freely diffusing in two dimensions in the etched cover slip wells by TIRF microscopy at a variety of laser powers but at constant temperature. Other groups have demonstrated that the exponent of the QD blinking power law PDF can change as a function of excitation power (20, 28, 30). Using the same type of QDs as employed in this study, we have shown previously that temporal correlation functions measured by TICS from samples of static QDs decay more rapidly as the illumination laser power is increased (22). We found that the decay of the temporal autocorrelation function measured for an ensemble of immobilized blinking quantum dots was fit well by a power law:

$$r(\tau) = \mathrm{A} - \mathrm{B}\tau^{\alpha} . \qquad (8)$$

The fitting exponent α reflects the variation in the underlying “on” time distribution and it can be related to the “on” time blinking probability distribution function exponent m_{on} as $\alpha=2-m_{on}$ (31, 32) and it decreases as excitation laser power increases (22). At higher laser powers the QDs blink more frequently, and shorter "on" events are observed on average which leads to the observed increased rate of correlation function decay.

We, therefore, expect that the same excitation intensity dependent decay due to blinking will be manifest in the temporal decay of correlation functions measured by TICS for the diffusing quantum dots, similar to what has been shown by Weiss and co-workers for faster time scale FCS measurements on semi-conductor nanoparticles (21). As with all fluctuation/correlation methods, the relative contribution is going to depend on the sampling time scale, the characteristic transport time and the blinking time(s).

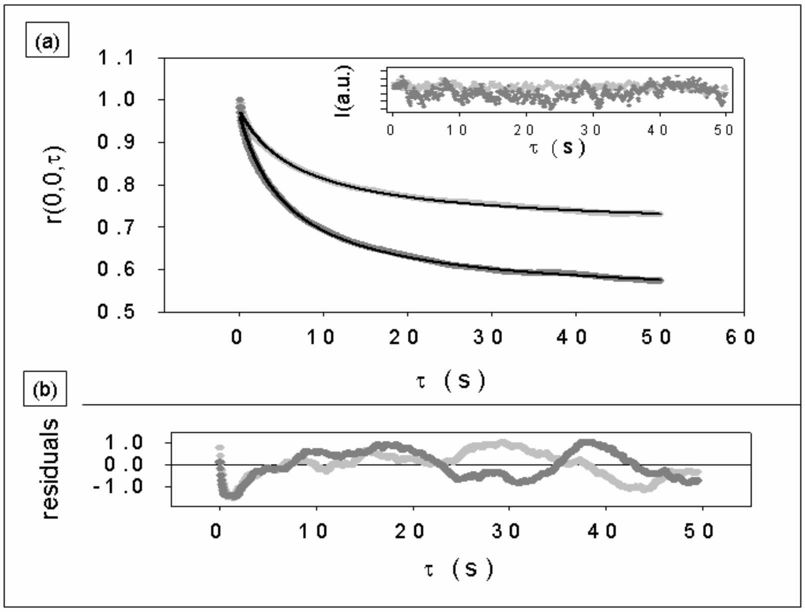

Figure 2

Typical normalized intensity time correlation functions for two different excitation powers calculated from the same sample of quantum dots diffusing and blinking. Excitation laser powers are 4.5 W/cm^2 (light grey) and 13.5 W/cm^2 (grey). Correlation functions and the average fluorescent intensity per frame in the image stack (inset) are normalized to 1 for comparison. A fit to 2d-diffusion model is shown in black with residuals for both fits below the plot. Average fluorescence intensity per frame changes from 0.92 to 1.04 and does not decay in time. Each image stack contained 2000 images with 63 ms time resolution.

Figure 2 shows normalized temporal autocorrelation functions measured by TICS from the same sample of diffusing QDs, but at two different laser excitation powers: 4.5W/cm^2 and 13.5W/cm^2. The overall shape of the autocorrelation functions does not change significantly, but fits of these decays to the standard 2D diffusion model (Eq. (3)) yield two different characteristic diffusion times: τ_1=7.38+/-0.05s s and τ_2=5.96+/-0.06s s which correspond to D=(1.88+/-0.02) x 10-2 $\mu m^2/s$ and (2.15+/-0.01) x 10-2 $\mu m^2/s$ respectively for the lower and higher powers. The average fluorescence intensity per image remained constant throughout the entire stack of 2000 images, thus eliminating the possibility that the differences in the measured D are due to changes in the brightness or bleaching of quantum dots with time (see inset Fig. 2). As the temperature remained constant throughout both measurements, we expect the diffusion coefficient to be the same for both samples. Clearly, the fluorescence intermittency introduces a systematic error into the TICS measurement obtained with the standard 2D diffusion fit model. More importantly, under these measurement conditions, the temporal autocorrelation functions fit reasonably well to the simple 2D model (see residuals in Fig. 2B) so an experimenter might erroneously assume that blinking was not significant and remain unaware of this systematic deviation due to blinking.

5.3.2 Accurate Measurement of Diffusion Coefficients using Image Correlation Methods

The QD sample that was imaged and analyzed to generate the temporal autocorrelation functions shown in Fig. 2 contained a mixed population of mobile and static nanoparticles. The presence of a static population of fluorescent emitters is known to account for the incomplete decay (offset) of the temporal autocorrelation function as measured by TICS (14). It might be argued that the difference between the TICS measured D at the two different laser powers is really reflecting contributions of the blinking of the static QD population to the decay of the temporal autocorrelation function as we have previously measured this effect for stationary nanoparticles (22). To test whether or not this is the case, we imaged two different model systems of QDs while systematically increasing the excitation laser power. One sample was prepared so that the QDs diffused relatively slowly and were intermixed with a significant fraction (~40%) of immobile nanoparticles. The second sample was prepared so that the QDs were diffusing more quickly (approximately an order of magnitude faster) with almost no static nanoparticles present. Furthermore we analyzed all sets of measurements for both samples by TICS and the reciprocal space variant kICS. It has been previously shown that the transport coefficients measured by kICS are independent of fluorophore photophysics (29). We did not calculate a Stokes-Einstein diffusion coefficient for these samples because it is known that glycerol readily absorbs water making it difficult to know the true viscosity of the sample, and because our sample chamber geometry was effectively a thin film of ~ 0.1 µm thickness.

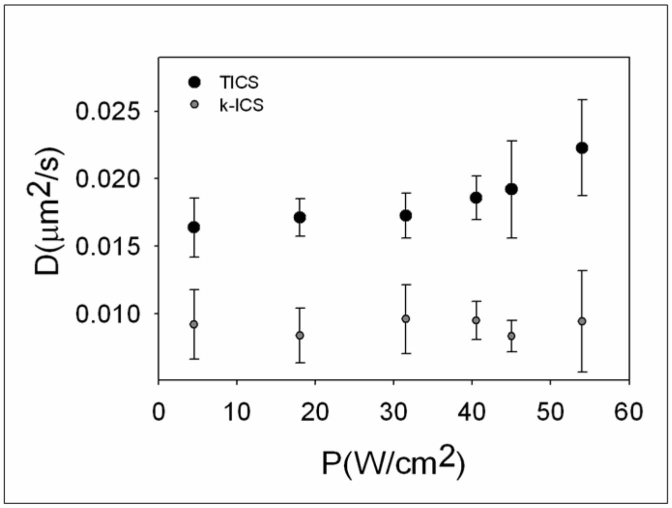

Figure 3

A plot of the diffusion coefficient as a function of laser power obtained from the sample that contained a static population of quantum dots. Diffusion coefficients calculated from TICS analysis (black circles) and from kICS (grey circles). The two dimensional diffusion model (Eq. 3) is used to fit TICS correlation functions. Each point is an average of 6 measurements. Error bars are the standard deviation.

Figure 3 shows the D as measured by TICS and kICS for the slow/static QD sample as a function of excitation laser power. At the lowest excitation power of 3 W/cm2 where the contribution of blinking fluctuations should be minimized, there is a systematic difference between the measured D_{TICS} = (1.6 ± 0.2) x10-2 $\mu m^2/s$, the kICS measured diffusion coefficient at the same power, and the average diffusion coefficient calculated from the kICS measurements at each power sampled ($<D_{kICS}>$ = (0.8 ± 0.2) x10-2 $\mu m^2/s$). This difference, where the D_{TICS} is systematically at least 50% greater than $<D_{kICS}>$, is constant for low to moderate laser powers and then begins to increase for powers greater than 31 W/cm^2. This trend shows the interplay between the characteristic transport fluctuation time and the time scales of the nanoparticle blinking which change as a function of laser power. More importantly, it demonstrates that even at the lowest excitation power, there is a systematic error in the TICS measured D for this sample because the measurement did not account for the blinking.

The results for the sample containing more rapidly diffusing QDs with a negligible static population are shown in Fig. 4. Again, the TICS measured D increases as a function of laser excitation power while the kICS measured D remains essentially constant within error over the range of powers used for imaging. The average diffusion coefficient calculated from the kICS measurements at each power sampled was <D_{kICS}> = (8.6 ± 0.2) x10-2 μm^2/s and this value differed from the TICS measured D by almost 50% for the highest powers used. At the lowest laser power, the D_{TICS} is slightly greater than D_{kICS}, but the error bars for these points overlap so the difference is within the statistical uncertainty.

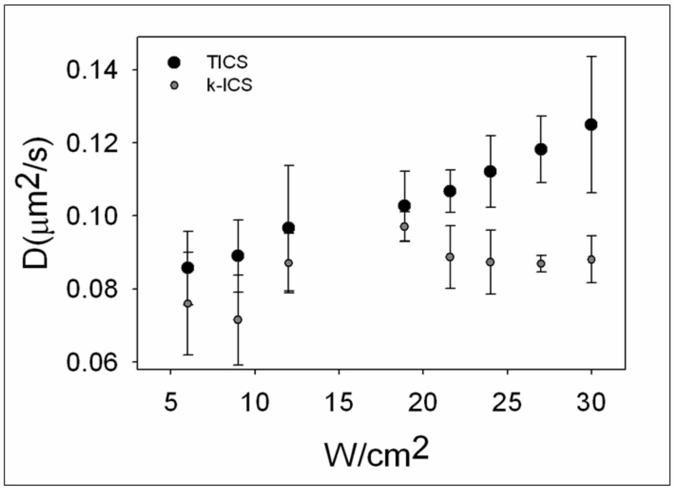

Figure 4

A plot of the diffusion coefficient as a function of laser power obtained from TICS analysis for a sample that did not contain a static population of quantum dots (black circles), when a simple two dimensional diffusion model is used to fit correlation functions. Diffusion coefficients calculated using kICS analysis are not affected by blinking (grey circles). Each value is an average of 4 measurements performed on the same sample. Error bars are standard deviations.

This overlap in D_{TICS} and D_{kICS} was not observed at the lowest laser power for the slow/static sample. For both of these samples, we assume that the exponent of the blinking power law distribution will be the same (identical excitation powers) and hence the time scales of the QD emission intermittency will be similar. However, for the slow/static QD sample, the characteristic diffusion time is approximately an order of magnitude larger than that of the rapid/mobile sample. Consequently the blinking fluctuations make a greater contribution to the decay of the TICS autocorrelation function for the slow/static sample because more on/off events can occur during the longer residency time of the QDs within each correlation area. In the rapid/mobile sample, the shorter characteristic diffusion time reflects that fewer on/off blinking events are sampled before the QDs exit each correlation area by diffusive transport. Hence the blinking contributes less to the decay of the TICS autocorrelation function and the D_{TICS} and D_{kICS} are the same within the statistical uncertainty. As the laser excitation power is increased, the QD blinking becomes more rapid and the nanoparticles exhibit on/off blinking events of shorter duration so more blinking fluctuations are sampled over the time scale of the characteristic transport time. Hence, we observe that D_{TICS} is systematically greater than D_{kICS} for the higher laser powers for this sample.

The lowest excitation power we used to image the model samples (3 W/cm^2) is similar to the lowest powers used in single molecule experiments (33). One might be tempted to use higher laser powers to increase the signal-to-noise ratio in such imaging studies because the QDs are more resistant to photobleaching. However, this would result in a greater systematic error for a TICS diffusion measurement that would not be detected if the standard diffusion fitting model is used. According to equation (7) an intercept of the k-space time correlation function, $\ln [\langle \theta(t)\, \theta(t + \tau) \rangle]$, reflects emission properties of fluorescent species. Therefore, a kICS measurement would detect changes in the blinking statistics as variations in the intercept of the k-space time correlation function and would measure an unbiased diffusion coefficient from the slope of this function (29).

5.3.3 Computer Simulation Results

We generated computer simulated image time series of point emitters with user set 2D diffusion and on/off emission probability distribution parameters for direct comparison with the model system experimental results and to investigate the role of temporal sampling in more detail. As was observed for the TICS experiments on the model QD samples, the normalized intensity fluctuation time autocorrelation functions calculated from the simulated image time series were well fit by the 2D diffusion model (data not shown), and the characteristic diffusion time decreased as m_{on} increased. Figure 5 presents the simulation results for the measurement of D_{TICS} and D_{kICS} as a function of m_{on}. As m_{on} increases, the systematic overestimation of the diffusion coefficient measured by TICS increases whereas the kICS measured transport coefficient matches the set D within statistical error. This trend is completely in accord with our experimental measurements.

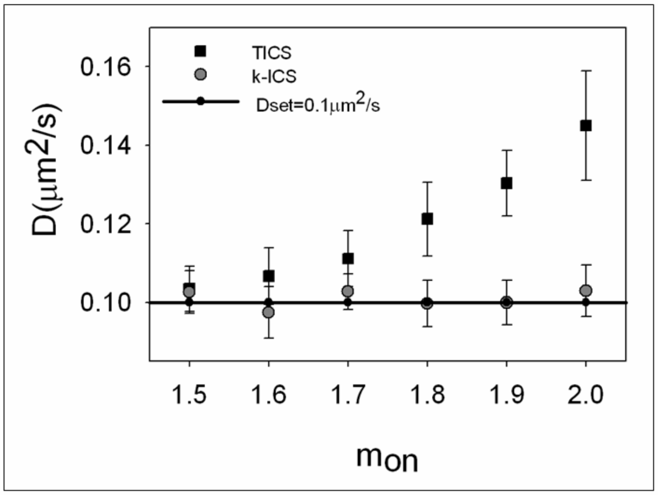

Figure 5

Diffusion coefficients calculated from TICS analysis of combined blinking and diffusion simulations of point emitters with varying “on” time PDF exponents and “off” time PDF exponent set to 1.5 (black squares). kICS results do not change with “on” time PDF exponent (gray circles). Parameters in simulations were set to mimic experimental conditions in model systems that did not contain a static population of QDs. Each image time-series was 2000 frames long, with an area of 64 x 64 pixels, time lag of 60ms between images and around 250 quantum dots per frame. The diffusion coefficient was set to $10 \times 10^{-2} \mu m^2/s$. Each value is an average from 20 simulations. Error bars are standard deviations.

5.3.4 The Effect of Temporal Sampling

Previous work has shown that the number of image frames sampled per correlation time (i.e. the ratio of the characteristic transport time, τ_d , to the image acquisition time) can determine the precision with which the characteristic correlation time can be measured by TICS (19). It was found that precision was optimized with sampling of two image frames per characteristic time and higher sampling rates did not increase the precision. However, since the quantum dots have no characteristic blinking time scale, we decided to use the computer simulations to generate image series with a variety of image frame sampling times to determine how this parameter would affect TICS measurements with this type of label. In practice, the frame-to-frame image sampling time can be adjusted over several orders of magnitude in imaging systems equipped with area detectors, by changing the CCD integration time. We adjusted the number of images sampled per characteristic diffusion time from 2.25 to 100 while keeping the total number of images in the time series constant.

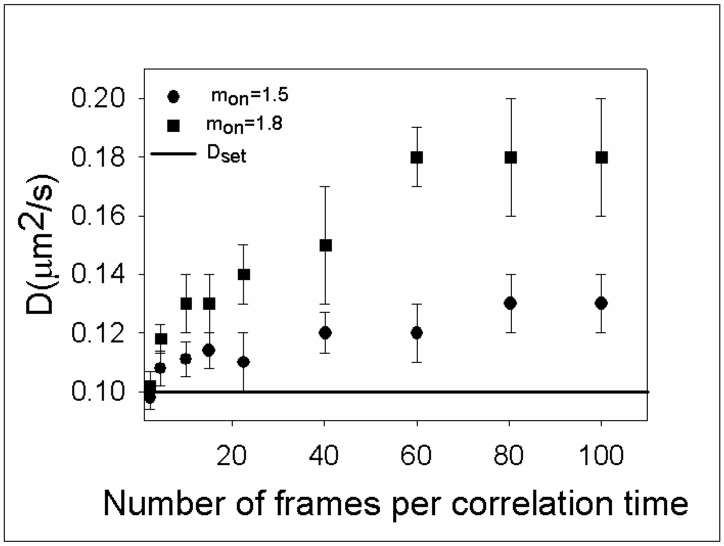

Figure 6

A plot of the recovered diffusion coefficient from simulated blinking and diffusing point emitters as a function of the number of frames per characteristic diffusion time when the two dimensional diffusion model is used to fit TICS data. The diffusion coefficient was set to 0.1μm^2/s. “on” time PDF exponents are set to 1.5 (circles) and 1.8 (squares). Error bars are standard deviation calculated from 20 simulations. The image series simulations contained 500 images, each with an image area of 128 x 128 pixels and around 900 particles per frame.

Figure 6 shows the TICS measured D as a function of the number of image frames sampled per characteristic diffusion time for two sets of simulations with m_{on} set at 1.5 and 1.8 while D was fixed at 0.10μm^2/s. The results show that the TICS measurement can recover this D within error for a temporal sampling ratio of around 2. However, as the sampling ratio is increased, the measured D deviates as an increasing systematic overestimation from the set value. This is due to the fact that it is the faster time scale blinking fluctuations which are now being sampled as the temporal sampling ratio is increased and this contributes to a more rapid decay of the autocorrelation function. In experimental applications, it would not be possible to optimize the temporal sampling without a priori knowledge of the characteristic diffusion time.

To further investigate this effect, we generated simulation image series with a fixed D while varying the m_{on} for the blinking power law distribution and two different interframe times were set so that sampling occurred at 13 and 130 frames per characteristic diffusion time. The image series were analyzed by both TICS and kICS to measure the diffusion coefficient.

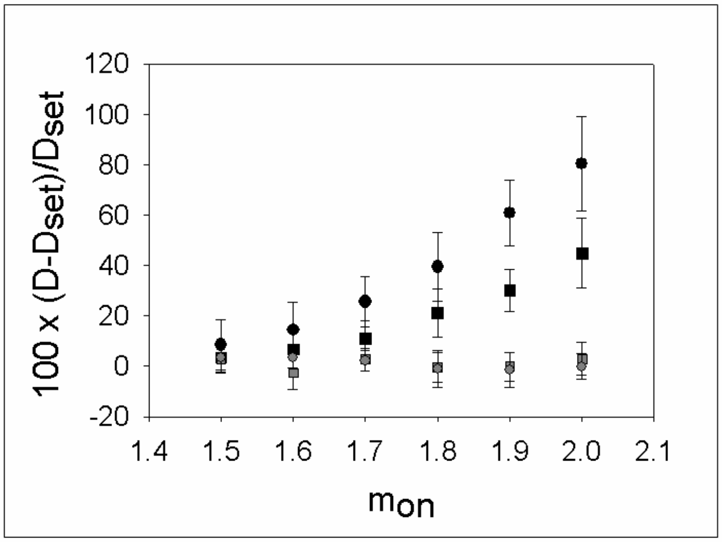

Figure 7

A plot of the relative error for recovered diffusion constants from TICS analysis of simulated point emitters blinking and diffusing in two dimensions as a function of “on” time PDF exponent for temporal sampling of 13 frames/ τ_d (black circles) and 130 frames/ τ_d ((black squares). kICS results (grey squares and circles) are insensitive to the blinking regime and temporal sampling. In all simulations D_{set} D_{set} t=0.1μm^2/s. Error bars are mean +/- standard deviation from 20 simulations. The simulations contained 2000 images, each with an image area of 64 x 64 pixels and 250 particles.

Figure 7 plots the results as the relative percent error in the measured diffusion coefficient as a function of m_{on}. Once again, it is clear that the TICS measurement can have a large systematic error depending on the relative contribution of the blinking fluctuations and how frequently they are sampled relative to the characteristic diffusion time. In contrast the kICS measurement recovers the set D with low error and is not affected by the temporal sampling ratio or the blinking fluctuations. This assumes that the imaging rate is sufficiently high so that a minimum of two images are recorded per characteristic diffusion time to properly sample the transport process.

5.3.5 Live Cell Measurements

To compare TICS experiments on cells with results obtained from simulations and model systems we measured diffusion of CD73 protein labeled with quantum dots. CD73 or ecto-5'-nucleotidase (5’-NT) is a glycosyl phosphatidylinositol (GPI) anchored protein. It is involved in T cell activation (34), lymphocyte adhesion to the endothelia (35), and its activity has been found to be upregulated in a variety of tumor types (36). Along with other GPI-anchored proteins, CD73 is thought to reside in hypothesized lipid raft nano-domains in the cellular plasma membrane. As such it is one of many potential molecular markers in the on-going search for in vivo lipid rafts.

To date, most quantitative studies of molecular dynamics with quantum dots as probes have focused on single particle tracking (SPT) techniques (37). One of the great strengths of fluorescence fluctuation techniques such as TICS is their ability to measure the dynamics of fluorescent particles at a relatively high density. In contrast, SPT can only be performed on samples in which the average particle spacing is significantly greater than the frame-to-frame particle displacements. The region of the membrane of the IMR-90 cell where the analysis was performed is outlined in Figure 1C. To verify that the CD73 protein is diffusing freely in that region, we examined the trajectories of several quantum dots whose traces could be resolved using SPT and did not find signs of confined diffusion (data not shown).

We made an effort to minimize QD blinking during data collection so we could expect TICS and kICS methods to give similar results. The temporal autocorrelation function measured by TICS from the analyzed region of the cell is shown in Figure 8A.

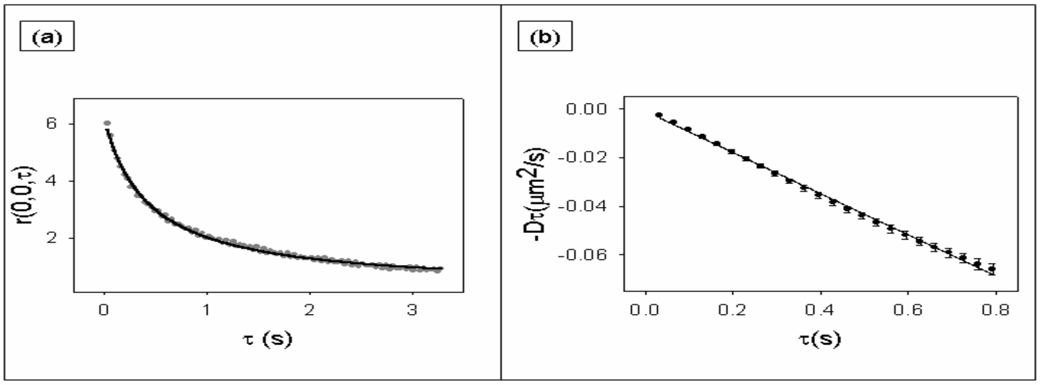

Figure 8

(A) The experimental time correlation function calculated for the 213x235 pixels cell region highlighted in Figure 1 (grey circles). Solid line is a fit to 2d-diffusion model (Eq. 3). Image time series contained 1798 frames with the time step of 33ms. The precision of the measurement was calculated using Ref. 29.

(B) Result obtained from kICS analysis. Every point is a slope recovered from Eq. 7 at each time lag τ, -Dτ,, plotted as a function of τ for a subregion of the CHO cell outlined in white in Figure 1C. The slope of this plot is – D_{kICS}.. The error bars are the error of the corresponding linear regressions.

We calculated the diffusion coefficient to be D_{TICS}=(0.109+/-0.008) μm^2/s from a fit of the 2D diffusion model to this correlation function. Analysis of the same image sub-stack using kICS gave D_{kICS}=(0.088 +/- 0.008) μm^2/s. Once again, kICS measures a smaller diffusion coefficient which is expected since the transport coefficient measured by the reciprocal space method is not affected by photophysical fluctuations. Thus, even for a sample where QD blinking did not appear by eye to be significant, luminescent blinking of the nanoparticles leads to a small systematic error.

5.4 Conclusion

We have calculated normalized intensity time correlation function of biocompatible CdSe/ZnS quantum dots blinking and diffusing in two dimensions and found that it fits well to a decay model that takes only diffusion into account (Eq. 3). However, this approach leads to significant systematic errors in the recovered diffusion coefficients due to quantum dot blinking. We found that the TICS measured diffusion coefficients are highly sensitive to experimental conditions, such as illumination power and temporal sampling, that change the blinking statistics or the sampling of this distribution. We have shown that the kICS measured diffusion coefficients are not affected by quantum dot blinking and that the reciprocal space method is the approach of choice for correlation measurements of transport in 2D systems where nanoparticle densities are high enough to make SPT impractical. We have demonstrated that the kICS approach can also be used to measure the transport of quantum dot labeled receptors on cells with the same advantages as were shown for the model systems.

References

1. Bruchez, M. Jr., M. Moronne, P. Gin, S. Weiss, and A. P. Alivisatos. 1998. Semiconductor nanocrystals as fluorescent biological labels. Science. 281:2013-2016.

2. Alivisatos, P. 2004. The use of nanocrystals in biological detection. Nature Biotech. 22: 47-52.

3. Wu, X.Y., J. H. Liu, Q. J. Liu, N. K. Haley, A. J. Treadway, P. J. Larson, F. N. Ge, F. Peale, and P. M. Bruchez. 2002. Immunofluorescent labeling of cancer marker Her2 and other cellular targets with semiconductor quantum dots. Nat. Biotech. 21:41-46.

4. Pellegrino, T., L. Manna, S. Kudera, T. Liedl, D. Koktysh, L. A. Rogach, S. Keller, J. Rädler, G. Natile, and W.J. Parak. 2004. Hydrophobic nanocrystals coated with an amphiphilic polymer shell: a general route to water soluble nanocrystals. Nano Lett. 4:703-707.

5. Gao, X., Y. Cui, M. R. Levenson, K. W. L. Chung, and S. Nie. 2004. In vivo cancer targeting and imaging with semiconductor quantum dots. Nat. Biotech. 22:969-976.

6. Howarth, M., K. Takao, Y. Hayashi, and A.Y. Ting. 2005. Targeting quantum dots to surface proteins in living cells with biotin ligase. Proc Natl. Acad. Sci. USA. 102:7583–7588.

7. Michalet, X., F. F. Pinaud, L. A. Bentolila, J. M. Tsay, S. Doose, J. J. Li, G. Sundaresan, A. M. Wu, S. S. Gambhir, and S. Weiss. 2005. Quantum dots for live cells, in vivo imaging and diagnostics. Science. 307:538-544.

8. Medintz, I.L., H.T. Uyeda, E.R. Goldman, and H. Mattoussi. 2005. Quantum dot bioconjugates for imaging, labelling and sensing. Nat. Mater. 4:435-446.

9. Warren, C. W. C., and S. Nie. 1998. Quantum dot bioconjugates for ultrasensitive nonisotopic detection. Science. 281:2016-2018.

10. Michalet, X., F. Pinaud, T.D. Lacoste, M. Dahan, M.P. Bruchez, A.P. Alivisatos, and S. Weiss. 2001. Properties of fluorescent semiconductor nanocrystals and their application to biological labeling. Single Molecules. 2:261–276.

11. Dubertret, B., P. Skourides, D.J. Norris, V. Noireaux, A.H. Brivanlou, and A. Libchaber. In vivo imaging of quantum dots encapsulated in phospholipid micelles. 2002. Science. 298:1759-1762.

12. Larson, D. R., W. R. Zipfel, R. M. Williams, S. W. Clark, M. P. Bruchez, F. W. Wise, and W. W. Webb. 2003. Water-Soluble quantum dots for multiphoton fluorescence imaging in vivo. Science 300:1434 – 1436.

13. Magde, D., E. Elson, and W. W. Webb. 1972. Thermodynamic fluctuations in a reacting system-measurement by fluorescence correlation spectroscopy. Phys. Rev. Lett. 29:705-708.

14. Wiseman, P. W., C. M. Brown, D. J. Webb, B. Hebert, N. L. Johnson, J. A. Squier, M. H. Ellisman and A. F. Horwitz. 2004. Spatial mapping of integrin interactions and dynamics during cell migration by Image Correlation Microscopy. J. Cell Sci. 117:5521-5534.

15. Hebert, B., S. Costantino, and P. W. Wiseman. 2005. Spatiotemporal image correlation spectroscopy (STICS) theory, verification, and application to protein velocity mapping in living CHO cells. Biophys. J. 88:3601–3614.

16. P. W. Wiseman, J. A. Squier, M. H. Ellisman, and K. R. Wilson. 2000. Two-photon image correlation spectroscopy and image cross-correlation spectroscopy. J. Microsc. 200:14-25.

17. Saffarian, S., and E. L. Elson. 2003. Statistical analysis of fluorescence correlation spectroscopy: the standard deviation and bias. Biophys. J. 84:2030–2042.

18. Koppel, D. E., 1974. Statistical accuracy in fluorescence correlation spectroscopy. Phys. Rev. A 10:1935-1945.

19. Kolin, L. D., S. Costantino, and P. W. Wiseman. 2006. Sampling effects, noise, and photobleaching in temporal image correlation spectroscopy. Biophys. J. 90:628–639

20. Nirmal., M., B. O. Dabbousi, M. G. Bawendi, J. J. Macklin, J. K. Trautman, T. D. Harris, and L. E. Brus. 1996. Fluorescence intermittency in single cadmium selenide nanocrystals. Nature 383:802-804.

21. Doose, S., J. M. Tsay, F. Pinaud, and S. Weiss. 2005. Comparison of photophysical and colloidal properties of biocompatible semiconductor nanocrystals using fluorescence correlation spectroscopy. Anal. Chem. 77:2235-2242.

22. Bachir, I. A., N. Durisic, B. Hebert, P. Grütter, and P.W. Wiseman. 2006. Characterization of blinking dynamics in quantum dot ensembles using image correlation spectroscopy. J. Appl. Phys. 99:064503-064510.

23. Krichevsky, O., and G. Bonnet. 2002. Fluorescence correlation spectroscopy: the technique and its applications. Rep. Prog. Phys.65: 251-297.

24. Ha, T., T. Enderle, D. S. Chemla, P. R. Selvin, and S. Weiss. 1997. Quantum jumps of single molecules at room temperature. Chem. Phys. Lett. 271:1-5.

25. Dickson, R.M., A.B. Cubitt, R.Y. Tsien, and W.E. Moerner. 1997. On/off blinking and switching behaviour of single molecules of green fluorescent protein. Nature. 388:355-8.

26. Kuno, M., D. P. Fromm, H. F. Hamann, A. Gallagher, and D. J. Nesbitt. 2001. ‘‘On’’/‘‘off’’ fluorescence intermittency of single semiconductor quantum dots. J. Chem. Phys. 115:1028-1040.

27. Kuno, M., P. D. Fromm, F. H. Hamann, A. Gallagher, and J. D. Nesbitt. 2000. Nonexponential "blinking" kinetics of single CdSe quantum dots: A universal power law behavior. J. Chem. Phys. 112:3117-3120.

28. Shimizu, K. T., G. R. Neuhauser, A. C. Leatherdale, A. S. Empedocles, K. W. Woo, and M. G. Bawendi. 2001. Blinking statistics in single semiconductor nanocrystal quantum dots. Phys. Rev. B, 63:205316- 205321.

29. Kolin L. D., D. Ronis, and P. W. Wiseman. 2006. k-Space image correlation spectroscopy: a method for accurate transport measurements independent of fluorophore fhotophysics. Biophys. J. 91:3061–3075.

30. Kobitski, A. Y., C. D. Heyes, and U. G. Nienhaus . 2004. Total internal reflection fluorescence microscopy-a powerful tool to study single quantum dots. Appl. Surf. Sci. 234:86-92.

31. Margolin, G., and E. Barkai. 2004. Aging correlation functions for blinking nanocrystals, and other on–off stochastic processes. J. Chem. Phys. 121:1566-1577.

32. Margolin, G., and E. Barkai. 2005. Nonergodicity of blinking nanocrystals and other Le´vy-walk processes. Phys. Rev. Lett. 94:080601- 080604.

33. Moerner, E. W., and D. P. Fromm. 2003. Methods of single-molecule fluorescence spectroscopy and microscopy. Rev. Sci. Instr. 74:3597-3619.

34. Thompson L.F., J.M. Ruedi, A. Glass, M.G. Low, and A.H. Lucas. 1989. Antibodies to 5'-nucleotidase (CD73), a glycosyl-phosphatidylinositol- anchored protein, cause human peripheral blood T cells to proliferate. J. Immunol. 143:1815-1821.

35. Airas, L., J. Hellman, M. Salmi, P. Bono, T. Puurunen, D.J. Smith, and S. Jalkanen.1995. CD73 is involved in lymphocyte binding to the endothelium: characterization of lymphocyte-vascular adhesion protein 2 identifies it as CD73. J. Exp. Med. 182:1603-1608.

36. Sadej, R., J. Spychala, and A.C. Skladanowski. 2006. Ecto-5'-nucleotidase (eN, CD73) is coexpressed with metastasis promoting antigens in human melanoma cells. Nucleosides Nucleotides Nucleic Acids 25:1119-1123.

37. Dahan M., S. Levi, C. Luccardini, P. Rostaing, B. Riveau, and A. Triller. 2003.Diffusion dynamics of glycine receptors revealed by single-quantum dot tracking. Science. 302:442–445.

A significant body of work has been published which examined properties that affect QD blinking, including light excitation power (1-3), the shell material around the QDs (4), environmental conditions (5) and the surrounding medium (6, 7). From these studies, several physical models have been proposed in an attempt to explain the inverse power law behaviour of the QD blinking statistics.

Given the wide range of proposed blinking models, it is not possible to predict the effects of protons on the QD photophysical properties. In the next chapter, we experimentally probe how the presence of H^+ changes the blinking and dark (non-emitting) fraction of QDs. This is of relevance not only for development and unification of theoretical models which aim to explain the power law behaviour of blinking statistics, but also for the understanding of biochemical interactions of QDs within subcellular environments.

This time we used standard histogram analysis for easier comparison to the previously published studies and because we were interested in the change of both, “on” and “off” time intervals.

1. Kobitski, A. Y., C. D. Heyes, and G. U. Nienhaus. 2004. Total internal reflection fluorescence microscopy - a powerful tool to study single quantum dots. Appl. Surf. Sci. 234:86-92.
2. Bachir, A., N. Durisic, B. Hebert, P. Grutter, and P. W. Wiseman. 2006. Characterization of Blinking Dynamics in Quantum Dot Ensembles using Image Correlation Spectroscopy. J. Appl. Phys. 99:064503.
3. Doose, S., J. M. Tsay, F. Pinaud, and S. Weiss. 2005. Comparison of Photophysical and Colloidal Properties of Biocompatible Semiconductor Nanocrystals Using Fluorescence Correlation Spectroscopy. Anal. Chem. 77:2235-2242.
4. Heyes, C. D., A. Y. Kobitski, V. V. Breus, and G. U. Nienhaus. 2007. Effect of the Shell on Blinking Statistics in Single Core-Shell Quantum Dots - A Single Particle Fluorescence Study. Phys. Rev. B 75:125431.
5. Banin, U., M. Bruchez, A. P. Alivisatos, T. Ha, S. Weiss, and D. S. Chemla. 1999. Evidence for a thermal contribution to emission intermittency in single CdSe/CdS core/shell nanocrystals. J. Chem. Phys. 110:1195-1201.
6. Pelton, M., D. G. Grier, and P. Guyot-Sionnest. 2004. Characterizing quantum-dot blinking using noise power spectra. Appl. Phys. Lett. 85:819-821.
7. Issac, A., C. v. Borczyskowski, and F. Cichos. 2005. Correlation between photoluminescence intermittency of CdSe quantum dots and self-trapped states in dielectric media. Phys. Rev. B 71:161302.

Chapter 6

6. A Common Mechanism Underlies the Dark Fraction Formation and Fluorescence Blinking of Quantum Dots

Reproduced from:
A common mechanism underlies the dark fraction formation and fluorescence blinking of quantum dots, N. Durisic, P. W. Wiseman, P. Grutter, C. Heyes, ACS Nano 3(5): 1167-1175 (2009)

6.1 Introduction

It has been known for over a decade that quantum dots (QDs) exhibit fluorescence blinking with power-law statistics over several orders of magnitude in time (1-3). However, a complete understanding of the physical mechanism underlying this phenomenon has remained elusive. Several models have been proposed to explain the temporary dark (“off”) state including tunneling of a charge carrier from the excited QD to an external trap state (4-6) or trapping at sites internal to the QD, particularly at the surface (7-9) In principle, power-law dynamics can be explained by a model containing static trap sites for the charge carriers (3, 10) but in order for QDs to be “on” long enough to be observed by fluorescence at the single QD level, a trap state must lie close to the QD. This would then lead to exponential blinking dynamics for these observed QDs (see the recent review by Cichos et al.(11) for a more complete discussion). Thus, to observe long on-times with power law dynamics at the single QD level, there must be a stochastically fluctuating component to the mechanism, such as fluctuations in the energy and/or position of the external trap sites5 or fluctuations of energy levels within the QD (8, 12).

Various observations have been made which lend support to one or another of these models. Issac et al. observed that blinking of CdSe-ZnS core-shell QDs is correlated to the dielectric constant of the environment surrounding the QDs (6), which was interpreted with the view that the traps are external. Krauss and Brus used STM to show that blinking is associated with the QD adopting a positive charge, indicative of electron ejection (4). However, Pelton et al. found that blinking statistics are independent of the external environment, seeding doubt in the external trap model (13). Heyes et al. later observed that the blinking of CdSe-ZnS core-shell QDs is independent of the shell thickness (9), which added to the uncertainty in the external trap model. These observations are consistent with a model in which the holes are trapped at the electron-rich surface of the QD or at the core-shell interface for the case of core-shell QDs (7-9). Subsequent experiments on CdSe-CdxZnyS core-multishell QDs with very thick (18 monolayers) and highly crystalline shells has revealed that blinking can be suppressed (14) Similar experiments on CdSe-CdS core-shell QDs, also with very thick and highly crystalline shells, showed reduced blinking (15) The key to these studies are the reduced lattice strain between the core and shell compared to the more commonly used ZnS shell material together with the thickness and high crystallinity of the shell, suggesting that trap sites can exist in the shell at crystal defects or at the core-shell interface (9) Recently, Pelton et al. measured the power spectral density of fluctuations and extended the timescale of blinking observations to the microsecond scale (16). They observed a change in the blinking behavior below a critical time of a few milliseconds, supporting a diffusion-controlled blinking model with the critical time depending on the characteristic diffusion time on the energy surface. In contrast, Sher et al. found that the blinking behavior of QDs is the same on the nanosecond timescale and on the hundred millisecond to second timescale (17), and FCS experiments have shown similar behavior on the microsecond timescale (10), implying that the blinking dynamics is unchanged across many orders of time. Chemical effects on the QD blinking have also been reported, but with conflicting observations. Hohng and Ha reported that blinking of core-shell QDs can be suppressed by the thiolated molecule, β-mercaptoethanol (BME) (18), while Kramm and coworkers reported that blinking was not suppressed by BME, but that the fluorescence intensity of single QDs was reduced (19) In fact, the effects of thiolated molecules on the fluorescence properties of QDs were shown to be very complex (20, 21). Fomenko and Nesbitt recently observed that blinking can also be suppressed by the presence of propyl gallate (22) The presence of electron donating moieties such as oligo (phenylene vinylene) (23), mercaptoethylamine (24) and dopamine (25) was shown to influence blinking. One study revealed that the intensity of the “on” state switches between different levels, with each level showing a different fluorescence lifetime (26). An earlier theoretical paper had proposed the existence of various “on” state intensities based on the presence of localized external charges near the surface of the QD (27). These apparently conflicting effects highlight the need for further experimental studies and theoretical development to understand the blinking mechanism more thoroughly.

Another surprising observation was made in 2002 by Ebenstein and Banin (28). Simultaneous AFM and fluorescence microscopy identified that a given sample of surface-immobilized QDs contains a fraction of dark particles – a subpopulation of QDs that are non-fluorescent. A similar experiment using QDs with a different surface functionalization highlighted the ubiquitous nature of the effect (29) The dark fraction was also shown to exist for QDs in solution, demonstrating that the observed effect was not a result of the surface immobilization (30) A significant fraction of dark particles was also found by photothermal detection (31) Additionally, the single particle quantum yield was shown to be very different from the ensemble quantum yield (28, 32) and, the ensemble quantum yield was found to be correlated largely to the dark fraction (30) Heyes et al. later showed that the “on” state average intensity was only slightly higher for higher quantum yield QDs (9), supporting the idea that the dark fraction plays a major role in determining the ensemble quantum yield.

In this study, we analyze the blinking statistics and the dark fraction of QDs as a function of pH. We show that reducing the pH of the solution surrounding the QDs from 9 to 6 changes both the blinking statistics and the dark fraction in a systematic way, which suggests a coupled role of H^+ ions in the underlying mechanism. From these observations, we propose a model by which the H^+ ions interact with the QD, changing the number and/or energies of trap states, which first change the blinking dynamics and then affect the dark fraction.

6.2 Results

Fig. 1(a) schematically depicts the experimental immobilization of streptavidin-functionalized QDs to a biotinylated glass surface. Immobilization is necessary for the water-soluble QDs so that blinking can be observed for long time periods as aqueous buffer solutions were placed over the samples and would otherwise wash them away from the surface. In order to check that the presence of the BSA surface did not affect the blinking, we performed the experiment by adsorbing the QDs to bare glass. The results were identical with the exception that analysis was complicated by the fact that many of the soluble QDs were washed away from the surface by the addition of buffer. Fig. 1(b) shows maximum intensity projection images as a function of pH calculated from image series of 100 s for fluorescent CdSe QDs (taken from different areas of the same sample). For comparison, a projection image of fluorescent QDs for a sample in air is also presented (Fig. 1(c)). Fig. 1(d) plots the relative number of fluorescent QDs present on the surface as a function of pH, and in air (normalized to 1 at pH 9). It is clear that the dark fraction significantly increased as pH is lowered from 9 to 6 (at pH 5, no fluorescent QDs were visible). Furthermore, there is virtually no difference between the number of fluorescent QDs observed in air and at pH 9, suggesting that OH^- ions have a negligible effect on the dark fraction compared to H^+ ions and that a concentration of H^+ ions of 10^{-9} M is too low to have an effect. Fig. 1(e) presents the maximum “on” state brightness averaged over many QDs as a function of pH. There is a clear trend for the QDs in the “on” state toward dimmer emission as pH is lowered from 9 to 6.

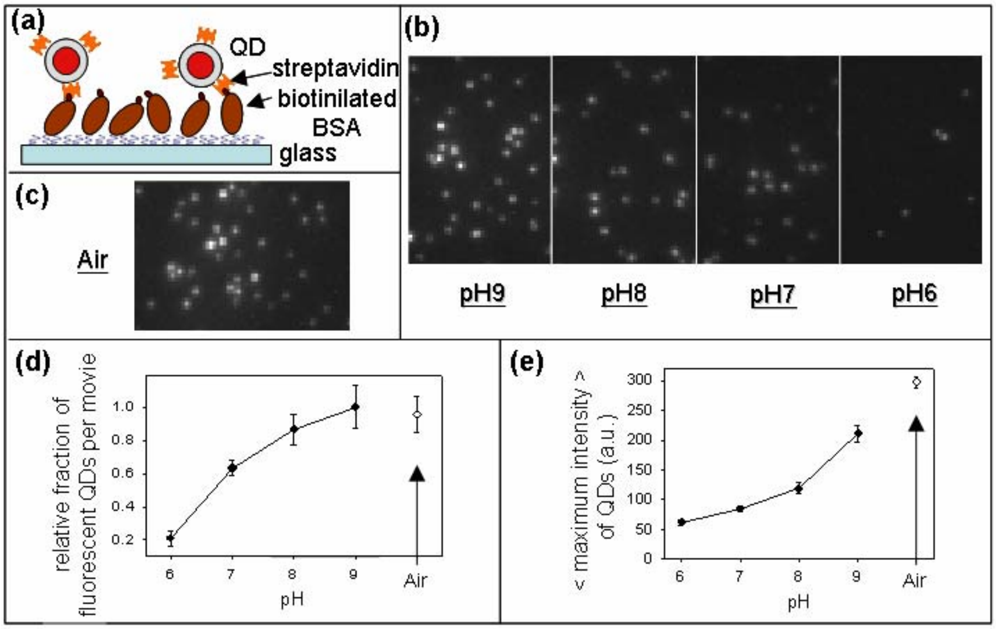

Figure 1

(a) Schematic representation of the immobilization of streptavidin-functionalized core-shell QDs onto biotinylated BSA-coated glass surfaces. (b) Fluorescence microscopy maximum intensity projection images of QDs as a function of pH. Each image is formed by displaying the maximum intensity of each pixel from each frame of a 2000 frame image series. (c) Fluorescence microscopy image of QDs in air as a comparison to those under different pH buffer conditions. (d) Quantification of the relative number of fluorescent QDs as a function of pH (normalized to 1 at pH 9) to determine the effect of pH on the dark fraction. (e) Average of the maximum intensity of each QDs in the “on” state as a function of pH.

To ensure that the QDs were not washed away by the various pH buffered solutions, AFM was used to image the same QDs upon exposure to different pH buffers. These data are presented in Fig. 7 at the end of this chapter.
The QDs remained bound to the surface after changing buffer solutions providing clear evidence that the reduction in the number of observed fluorescent QDs in Fig. 1 is related to the change in the dark fraction and is not the result of the unbinding of the QDs upon change of solution.

The probability to observe “on” or “off” events of a given time duration as a function of pH is presented in Fig. 2(a) and 2(b), respectively.

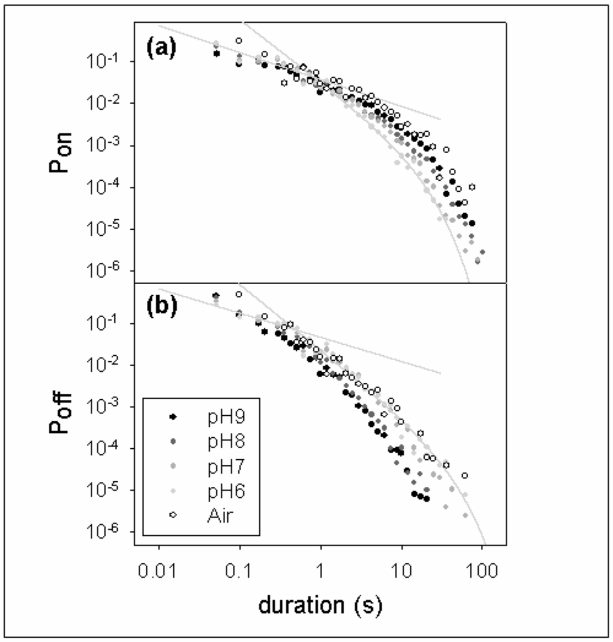

Figure 2

(a) Probability distributions of observing “on” events of a particular duration as a function of pH and in air. (b) Probability distributions of observing “off” events of a particular duration as a function of pH and in air.

There is a clear trend toward observing shorter “on” events and longer “off” events as the pH is lowered. The probability distributions have complex shapes and we attempted to fit the data to several functions based on a number of models in the literature. These included single power law (3), exponential (10), single power law with exponential cutoff (2, 9, 12), as well as a stretched exponential function. A power law with exponential cutoff is found to fit the data well at longer time durations, as has been observed previously for “on” times (2, 9), but we also observe it here for “off” times on approximately the same time scales. Additionally, at short binning times (<1 s), a second power law behavior is evident for both "on" and "off" times. This additional behavior only occurs for samples exposed to pH solution, and not for those in air. A recent paper by Pelton et al. (16) also observed the change in power law exponent at faster timescales and fit the fast timescale region with one power law (when t«tc) and fit the slower timescales region with a different power law (when t» t_c). By using this fitting method we were able to obtain excellent fits to our experimental data at the various pH values. Recent theoretical and experimental papers have discussed the possible origins of this short-time scale behavioral change in the framework of a diffusion-controlled mechanism underlying the blinking process (12, 16, 33). Intermittent diffusion of the energy levels across a certain boundary defining the transition from an "on" to an "off" state, solved as a first-passage time problem, yields a power law probability density function for blinking in the form (8, 12)

$$P(t) \propto t^{m} \qquad (1)$$

with m = –(1 +v). Theoretical studies have suggested v = 0.5, in agreement with many experimental observations showing m ≈ –1.5 (8, 12, 33). Equation (1) holds only for times longer than a critical time, t_c, below which it takes the form (12, 33)

$$P(t) \propto t^{a} \qquad \text{for } t \ll t_c \qquad (2)$$

where a = –(1 – ν). A value of t_c in the range ~5-35 ms was recently found experimentally for QDs in air (16). However, it was discussed that t_c varied from sample to sample. Finally, the probability density function often shows an exponential damping tail at long times (2, 8, 9, 12, 33), leading to an extension of equation (1) to the form

$$P(t) \propto t^{m} \exp\left(-{}^{t}\!/\!{}_{\tau}\right) \text{ for t » } t_c \qquad (3)$$

where ṿ is the characteristic time of the exponential tail.

We have fit our experimental data to equations (2) and (3) for the short timescales (< t_c) and the long timescales (>t_c), respectively, and extracted four parameters for both “on” and “off” time distributions: the lower-power law slope at short timescales, $\alpha = -(1 - v)$, the power law slope at intermediate timescales, $m = -(1+v)$, the characteristic time describing the exponential roll off at longer timescales, τ, and the time at which the two power law functions intersect, t_c. An example fit is shown for pH 6 in Fig. 2. Due to the log scales, in order that the data at low probability is able to be adequately fit, the chi-squared values of the low probability data are logarithmically weighted accordingly (i.e. the data is fit by linearizing the log scale, see Heyes et al. (9). All pH data were fit in the same way and were of similar quality. The extracted parameters for all samples (including in air) are presented in Fig. 3(a-d) for “on” times and Fig. 3(e-h) for “off” times.

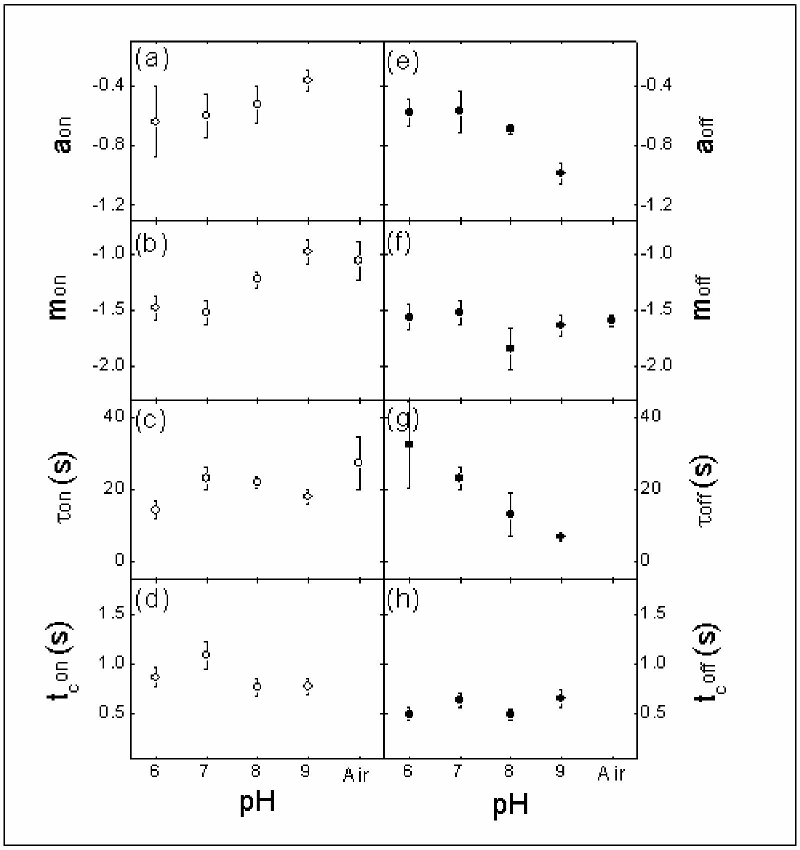

Figure 3

Extracted parameters from equations (2) and (3) to describe the blinking dynamics (a-d) for “on” events and (e-h) for “off” events: the lower-power law slope at short timescales, a (a, e), the power law slope at intermediate timescales, m (b, f), the characteristic time describing the exponential roll off at longer timescales, τ (c, g), and the time at which the two power law functions intersect, t_c (d, h).

The decrease in “on” times duration and increase in “off” times duration evident from Fig. 2 are manifest in the extracted fit parameters as follows: For “on” times, the power law slope, m, increases in steepness from –1 at pH 9 to –1.5 at pH 6, whereas it is approximately constant at –1.6 for “off” times over the same pH range. The power law slope, α, becomes more negative (steeper) for “on” times and less negative (flatter) for “off” times as pH is lowered. The characteristic time describing the exponential roll-off, τ, increases for “off” times as pH is lowered, but remains relatively constant for “on” times between pH 9 and 6. Finally, the extracted t_c value describing the critical time at which the power law behavior changes slope, shows no systematic variation over the pH range studied for both “on” and “off” times, varying between 500 ms and 1 s. However, t_c tends to be slightly lower for “off” times as compared to “on” times. In air, no change in power law slope is observed at shorter timescales for both “on” and “off” times, and thus both α and t_c are not extracted. Furthermore, the “off” times did not show the exponential roll off in air, in agreement with previous data (1, 2, 5, 6, 9, 16, 34, 35), which estimated τ_{off} ff to be on the thousand second timescale for a QD sample dried in air (35).

We also performed the same experiments on uncapped CdSe QDs (consisting of only a CdSe core and TOPO/HDA ligands). In general, the results agree very well with those of the core-shell QDs. The detailed data are given in Fig. 4.

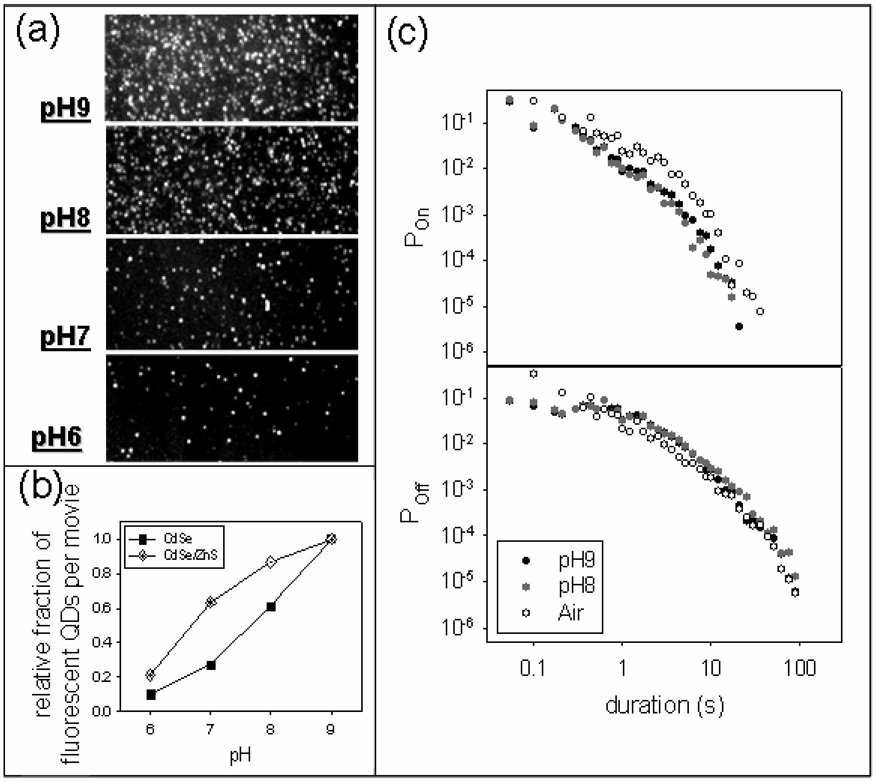

Figure 4

(a) Fluorescence microscopy image of QDs as a function of pH. The images are formed the same way as in Fig. 1. (b) Quantification of the relative number of fluorescent QDs as a function of pH (normalized to 1 at pH 9) to determine the effect of pH on the dark fraction. Both capped and uncapped QDs are shown for comparison. (c) Probability distributions of observing “on” and “off” events of a particular duration in air and at pH 9 and 8.

Specifically, an increase in the dark fraction is observed as pH is lowered from 9 to 6. However, the effect was significantly stronger for uncapped QDs than for core-shell QDs. This result is expected due to the lack of a protective shell layer which offers some shielding of the CdSe core. Furthermore, there is already a large difference in the blinking statistics between pH 9 buffer and air, suggesting that a concentration of H+ of 10^{-9} M is already sufficient to produce a strong effect. This observation is in contrast to the core-shell QDs, which show very similar results for the air and the pH 9 buffer samples (Fig. 1). Upon addition of pH 9 buffer, the "on" times decrease and the "off" times increase significantly. Lowering to pH 8 causes an additional slight change, but it is apparent that the effect of H^+ ions is practically saturated at pH 9. On the other hand, the presence of the shell in the core-shell QDs requires a lower pH in order to see the same magnitude of change (Fig. 2). For the uncapped QD samples, image time series at pH values lower than 8 contained too few fluorescent QDs to allow a statistically significant analysis. Therefore, no further analysis was performed for the uncapped QDs. In any case, the results on uncapped CdSe QDs support our results on core-shell QDs which suggest a proton induced effect on both the dark fraction and the blinking statistics.

The fact that the core-shell QDs did show an effect on the observed dark fraction and blinking as a function of pH was initially a surprising result. This prompted us to perform a TEM characterization of the sample to determine the morphology and homogeneity of the ZnS shell. An example image is presented in Fig. 5, which clearly shows that the ZnS shell is highly inhomogeneous and rod-like in shape.

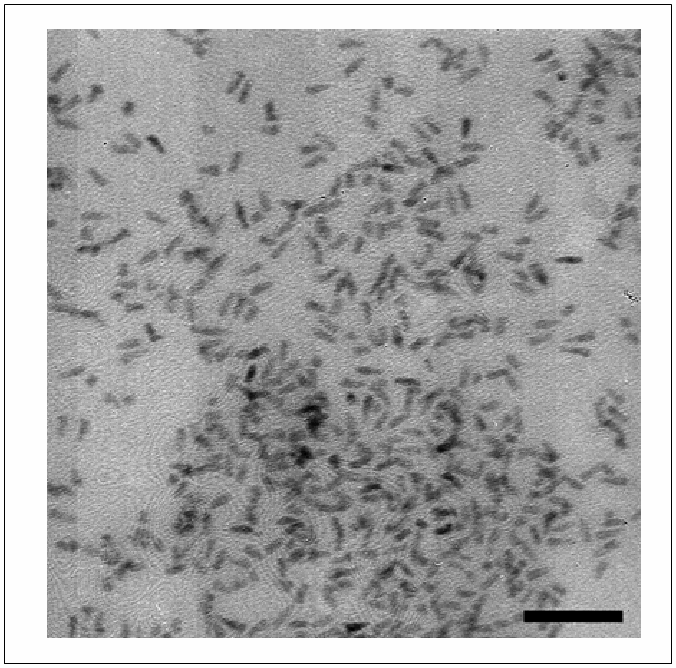

Figure 5

Transmission electron microscopy image of streptavidin-functionalized core-shell QDs. The particles are clearly non-spherical due to their inhomogeneously grown shell highlighting the fact that the protection offered by the ZnS shell is not ideal. Scale bar = 50 nm.

Non-uniform shell growth is often observed, and has been characterized in the literature (36-39). Unpolarized QD emission confirmed that this is also the case in our sample (data not shown). There is a wide distribution of shell thickness and morphology both within a single QD and for different nanoparticles, which clearly does not offer optimal uniform protection of the CdSe core from the external environment. Thin sections of the shell (or small holes in the shell layer) would allow H^+ ions to interact with the CdSe core which would affect their fluorescence properties, and this is supported by our observations.

6.3 Discussion

The coupled observation of changing of the blinking statistics and the dark fraction of the QDs as a function of pH suggests that the mechanisms underlying these effects are related. The variation in power law exponent and exponential bending tail was discussed theoretically by Tang and Marcus (12, 33). In their model, the power law exponent, m, for “on” and “off” times was related to the diffusion of rate constants for the transitions from the bright state to the dark state, γ_L and γ_D, respectively, shown in Fig. 6(a).

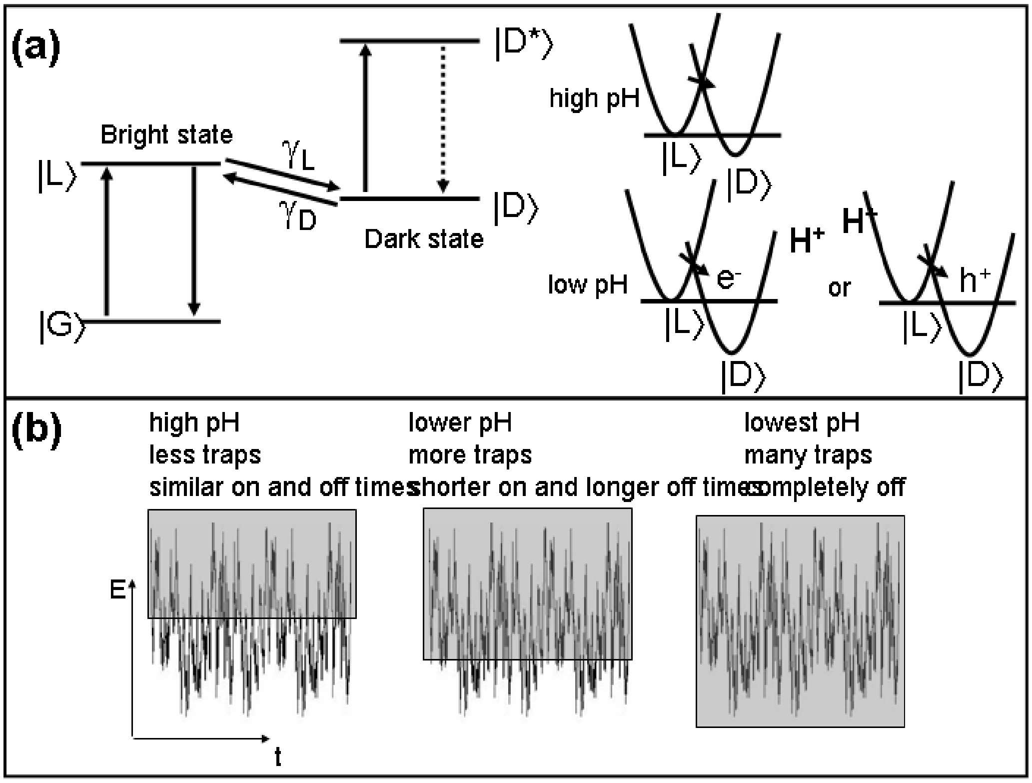

Figure 6

Models describing the effects of pH on the blinking statistics and the dark fraction.

(a) using the Tang-Marcus model (12, 33), blinking is described as a diffusive transition between a bright state and a dark state on a potential energy surface. The possible effects of H^+ ions are presented to explain our observations of increased “off” times and decreased “on” times with decreasing pH.

(b) using the Frantsuzov-Marcus model (8), blinking is described as diffusion of the transition energy between the 1Se and the 1Pe conduction band electronic energy levels which cross a transition region between being in (shaded area) and out of (non-shaded area) resonance with the energy difference between the $1S_{3/2}$ valence band hole state and a number of hole trap states lying deep in the band gap. Increasing the number of hole trap states (and/or decreasing their energy relative to the $1S_{3/2}$) will cause a reduced crossing probability thereby increasing the “off” times and decreasing the “on” times duration.

Our data suggest that m_{on} varies with pH but that m_{off} remains relatively constant (Fig. 3). In the framework of the Tang-Marcus model (12, 33) this is consistent with γ_{L} being affected by pH but γ_{D} not. If the ratio of γ_{L} to γ_{D} is large enough, the QD will spend the majority of its time in the dark state, ”D”, keeping the QD “off” and effectively increasing the observed dark fraction. In the same model, the exponential cutoff tail was related to the depth of the potential well of the dark state, ”D”, relative to the bright state, ”L”. A deeper potential well for ”D” relative to ”L” would increase the probability of observing longer “off” times resulting in an increase in τ_{off} off. Our observation that decreasing the pH causes an increase in the τ_{off} off is consistent with greater number of H^+ ions reducing the depth of the ”D” state potential well relative to ”L”. A possible explanation for this observation may be related to the presence of H^+ ions at the surface either assisting the trapping of an electron adjacent to it or trapping a hole at the opposite side of the QD due to Coulomb repulsion (Fig. 6(a)), thereby reducing the depth of ”D” relative to ”L”. Changing the depth of ”D” relative to ”L” should also change the relative slopes at the intersection of the two states. In particular, the presence of external positive charges such as H^+ ions, has been shown to affect the electron and hole wavefunctions (27), and one would expect them to change the shape of the potential wells of ”D” and/or ”L”. Thus, the H^+ ions would affect the intersection between these states. Since m_{on} and m_{off} are related to diffusion on these potential energy surfaces, it is not surprising that pH affects m_{on} and/or m_{off}. The presence of an electric field was shown to influence the spectral diffusion in QDs due to rearrangement of charges within the QD (40) which is also consistent with our hypothesis. Our observation of the change in m_{on} with pH implies that the H^+ ion affects the ”L” to ”D” transition more than the ”D” to ”L” transition, which would mean that the H^+ ion interacts more strongly with ”L”. This is consistent with the ”D” state being a hole trap rather than an electron trap state. This hole-trapping mechanism is also in accordance with the Auger-assisted hole trapping model proposed by Frantsuzov and Marcus, highlighting the coupled nature of these two models (8).

An alternative explanation of the pH effect on blinking and dark fraction would be that H^+ ions cause a chemical change at the QD surface which increases the number of hole-trap states (and/or reduces their energy). In the framework of the Frantsuzov-Marcus diffusion-controlled Auger-assisted hole trapping model (8), such an effect is described by an increase in the width of the shaded area as shown in Fig. 6(b), thereby increasing the time in which the transition energy between the hole trap states and the $1S_{3/2}$ valence band state remains in resonance with the transition energy from the 1Se to the 1Pe excited electronic state (the QD is in the “off” state). If the number of trap states increases sufficiently (and/or the energies of the trap states are lowered enough), the resonance condition will always be met, and the QD will always be dark – thus increasing the dark fraction. Naturally, one would expect that the number and/or position of trap states follows a certain distribution over the QD ensemble at a given pH. As pH is lowered, more trap states are formed, which leads to a shift in the distribution so that, on average as pH decreases, one first observes longer “on” times, then shorter “on” times (longer “off”) and finally completely “off”. It should be noted here that these results have shown that the OH- ions at high pH have little effect on blinking but that the effects increase as pH is lowered, suggesting that it is specifically the H^+ ions that are responsible for the observations. We assume that the H^+ ions cause these effects by interaction with the QD surface but it should be clarified that we show no direct evidence of H^+ ions at the QD surface. It may be possible that if other small ions were to interact with the QD surface, they could cause a similar effect. However, our initial experiments with varying NaCl concentration showed little effect. A possible reason for this is that that the Na+ and Cl- ions may be too large to cause an effect on the core through the shell material. Future investigations on the effect of other small positive ions are necessary to make any further conclusions.

The tendency for the QDs to be less bright in the "on" state as pH is lowered (Fig. 1(e)) is in agreement with ab initio calculations performed by Wang (27). The calculations showed that the presence of a charge close to the surface of the QD affects the overlap of the electron and hole wave functions in the "on" state thereby reducing the fluorescence intensity (27). Our data in Fig 1(e) provide experimental evidence for these calculations, and support our hypothesis that H^+ ions indeed interact with the QD core. Furthermore, the observation of a decrease in "on" state intensity between air and pH 9 shows that the intensity is already affected by the presence of 10^{-9} M H^+ ions. However, as described above, the blinking is not yet affected at this pH for core-shell QDs (but the same does not hold for uncapped QDs, evident from the difference in blinking between air and pH 9, Fig 6). Then, as more H^+ ions are added, the blinking dynamics begin to be affected and finally, when a certain number of H^+ ions interact with the core, the QD enters a permanent "off" state.

We have also observed the change in power law slope at shorter timescales as was recently observed by Pelton et al (16). However, the value of t_c found for the QD samples measured in this study is on the 500 ms to 1 s timescale, about 2 orders of magnitude longer than the QD samples measured by Pelton et al. Other experiments on the 0.2 ms timescale did not show a change in the power law slope(3), as did experiments on the nanosecond timescale(17). It has been previously discussed that the value of t_c may depend on a variety of parameters such as sample preparation, temperature, excitation intensity and environmental conditions. We found a t_c on the 500 ms – 1 s timescale only for samples exposed to the pH buffers, but not for samples dried in air. This t_c observation was true for both the core-shell QDs and uncapped QDs under the same experimental conditions, suggesting that the exact nature of the experimental conditions may play a larger role in determining t_c than the actual sample preparation does. Most previous QD blinking experiments have been performed either on QDs dried in air or encapsulated within polymers(1, 2, 5, 6, 9, 16, 34), and the only evidence of t_c under these conditions was found on much shorter timescales (~5-35 ms) (16). It appears that the presence of solution (solvent and/or solute) molecules increases t_c from the several millisecond timescale to the several hundred millisecond timescale. The slightly lower value of t_c for "off" times compared to "on" times for these samples may be related to the idea that the presence of interacting species (e.g. solvent and/or solute) affects diffusion on the potential energy surface of the bright state more than the dark state, also in agreement with the fact that m_{on} changes more than m_{off}. However, more experiments are necessary to pinpoint the exact determinants of t_c.

In conclusion, we have observed that solution pH affects both the blinking dynamics and the dark fraction of QDs in a systematic way. A diffusion-controlled model may be used to describe a coupled effect of H^+ ions on blinking and dark fraction. The presence of H^+ ions affects the transition probability to a dark state either by increasing the rate of diffusion to the dark state, or by increasing the number of available trap states, or both. When the diffusion rate to the trap states and/or the number of trap states increases above a certain point, the QD will always be in an “off” state, thereby increasing the dark fraction. Our experimental results support a mechanism connecting QD blinking and dark fraction via a diffusion-controlled model. However, other possible interpretations cannot be ruled out at the present time. Although several studies have shed doubt onto the external trap model (9, 13), other reports suggest that blinking does change with environmental factors such as the dieletric constant of the environment6 or the addition of electron donating species to the solution (18, 24). The external traps may also react to H^+ ions, which then may affect blinking. In core-shell QDs with reasonably thick shells, external traps are expected to be at least several nanometers from the emitting core, so the traps should be strongly affected by pH if they do play a role in blinking. An additional interpretation on blinking was provided by Dutta et al. with the hypothesis that fluctuations in the surface charge density of double layer screening charges around the QDs can lead to power law blinking dynamics (41). This is only relevant for QDs in solution and not for samples dried in air or trapped in a solid matrix. However, this double layer potential fluctuation may be affected by pH and does provide a possible alternative relevant mechanism of blinking in solution to that in air or in a solid matrix. From the conflicting reports published in the literature, it is likely that a number of different mechanisms may be responsible for blinking. These results are particularly important for developing a more complete theory of QD blinking, but are also relevant in various applications of QDs, especially for quantitative biological imaging applications where pH variations exist between the cytoplasmic and extracellular spaces and within organelles (42).

6.4 Materials and Methods

6.4.1 QD samples

We used commercially-available streptavidin-functionalized CdSe/ZnS quantum dots (QD605-streptavidin, Invitrogen Canada Inc., Burlington, ON) with emission wavelength centered at 605 nm. Two different batches of QDs were used to ensure that effects observed were not batch-specific. Additional experiments on uncapped CdSe QDs were performed with QDs synthesized in our laboratory (emission wavelength 605 nm) in trioctylphosphine oxide (TOPO) and hexadecylamine (HDA) and using CdO as a precursor following standard procedures (43, 44). All chemicals were purchased from Sigma-Aldrich (St. Louis, MO), unless otherwise stated.

6.4.2 Attaching QDs to glass cover slips

The microscope cover slips (Fisher Scientific #1) were first cleaned in Piranha solution (3:1 concentrated sulfuric acid: 30% hydrogen peroxide). Glass surfaces were then amino functionalized using 2% (v/v) 3-aminopropyltriethoxylsilane (Pierce, Rockford, IL) in anhydrous acetone. The amino groups were next modified with a 10 mM aqueous Sulfo-LC-SPDP solution (Pierce) to render the surface reactive to sulfohydryl groups. Biotinilated BSA was reduced in 50 mM DTT, exposed to the glass surface and stored over night at 4°C to allow the sulfohydryl group of the BSA to covalently bind to the functionalized glass cover slip. Residual unconjugated BSA was removed from the surface by rinsing with PBS-EDTA buffer (Pierce).

The commercial QD stock solution (~2 mM) was diluted by a factor of ~100 in MilliQ water (>18 MΩcm-1) and sonicated for 15 min prior to deposition on the protein-coated glass coverslip. The coverslip was then rinsed with MilliQ water to remove unbound QDs. Home-made, uncapped CdSe QDs were deposited directly from a dilute toluene solution onto a Piranha-cleaned glass cover slip.

The QD solution was dried by air flow shortly after deposition to minimize the formation of aggregates on the glass caused by cohesive forces during slow drying. Since the uncapped CdSe QDs have water-insoluble ligands on their surface, they are not washed away by exposing them to aqueous pH buffer solutions, and thus covalent immobilization was unnecessary. All samples were imaged immediately after preparation.

6.4.3 Fluorescence microscopy measurement and analysis of single QDs.

To investigate the effects of base or acid on QD fluorescence, HCl or NaOH was added to PBS buffer (Fisher Scientific, Pittsburgh, PA) to prepare solutions with pH values ranging from 9 to 5. The buffer was deposited directly on the glass cover slips to which the QDs were attached.

Image time series consisting of 2000 frames with 50 ms frame resolution of spatially resolved QDs were collected on a home-built objective-type total internal reflection fluorescence (TIRF) microscope with an intensified PentaMax charge-coupled device (CCD) camera (Princeton Instruments, Trenton, NJ) as previously described45. The 488 nm line from a CW Ar+ laser (Melles Griot 35 LAP 431, Carlsbad, CA) was used for excitation through a Zeiss Planapo 100×, 1.45 NA objective lens. We adjusted the laser power to ensure that no photobleaching occurred, while achieving maximum brightness. We determined a laser power of ~0.3 mW to be optimal, which gives a power density at the sample of ~3 Wcm^{-2}. Fluorescence from the sample was collected using the same objective and filtered with an emission filter centered at 605 nm with a bandwidth of 55 nm (Chroma Technology, Rockingham, VT) and imaged onto the CCD camera.

Histogram analysis was performed as previously described (9, 34), with slight modification. A maximum intensity projection image is calculated by recording the maximum intensity of each pixel for all frames in the time series in a single projected image frame. This method allows the displayed intensity of each QD to be independent of its blinking statistics and only dependent on its maximum integrated brightness within a single frame. This image is used to calculate the number of fluorescent QDs in the sample area, and subsequently to identify the coordinates of single QDs. The fluorescence from each QD as a function of time is extracted from the image series, a threshold is set, determined by the local background intensity, to distinguish “on” events from “off” events, and the duration of times that the QD spends in each state is calculated. This procedure is repeated for several hundred individual QDs.

6.4.3 Atomic force microscopy (AFM).

AFM images were acquired using a Bioscope I with Nanoscope IIIa controller (Veeco Instruments, Woodbury, NY) operating in contact mode. The scan rate was set to 1 Hz over a total area of 5 × 5 μm^2 at 512 × 512 pixels. All images were obtained in liquid using silicon nitride tips (Veeco Instruments).

6.4.4 Transmission electron microscopy (TEM).

A drop of QD solution was placed on a TEM grid (Electron Microscopy Sciences, Hatfield, PA) and left to dry in a desiccator for ~2 h. TEM images were acquired on a Philips CM200 electron microscope operating at 200 kV.

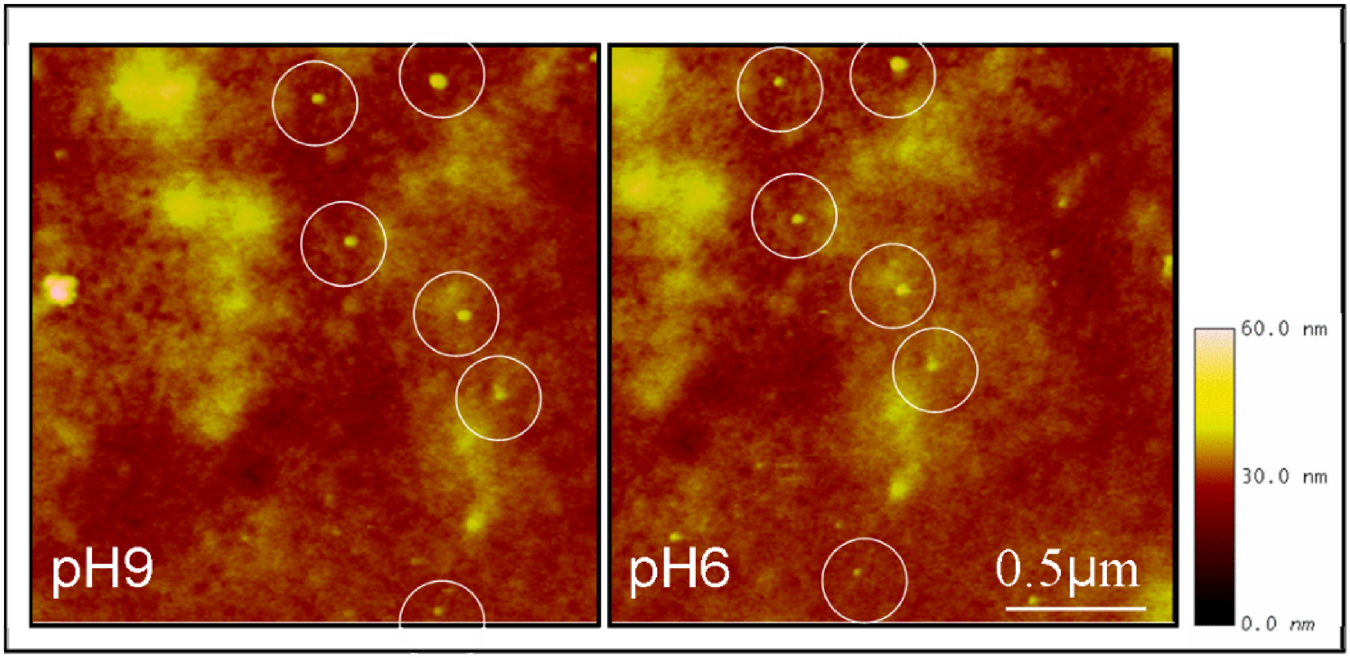

Figure 7

Atomic force microscopy images of the same immobilized QDs in pH 9 buffer (left) and in pH 6 buffer (right) highlighting the fact that QDs are not removed from the surface after exposure to these buffers.

References

1. Nirmal, M.; Dabbousi, B. O.; Bawendi, M. G.; Maklin, J. J.; Trautman, J. K.; Harris, T. D.; Brus, L. E. Fluorescence Intermittency in Single Cadmium Selenide Nanocrystals. Nature 1996, 383, 802-804.

2. Shimizu, K. T.; Neuhauser, R. G.; Leatherdale, C. A.; Empedocles, S. A.; Woo, W. K.; Bawendi, M. G. Blinking Statistics in Single Semiconductor Nanocrystal Quantum Dots. Phys. Rev. B 2001, 63, 205316.

3. Kuno, M.; Fromm, D. P.; Hamann, H. F.; Gallagher, A.; Nesbitt, D. J. Nonexponential Blinking Kinetics of Single CdSe Quantum Dots: A Universal Power Law Behavior. J. Chem. Phys. 2000, 112, 3117-3120.

4. Krauss, T. D.; Brus, L. E. Charge, Polarizability, and Photoionization of Single Semiconductor Nanocrystals. Phys. Rev. Lett. 1999, 83, 4840-4843.

5. Kuno, M.; Fromm, D. P.; Johnson, S. T.; Gallagher, A.; Nesbitt, D. J. Modeling Distributed Kinetics in Isolated Semiconductor Quantum Dots. Phys. Rev. B 2003, 67, 125304.

6. Issac, A.; Borczyskowski, C. v.; Cichos, F. Correlation Between Photoluminescence Intermittency of CdSe Quantum Dots and Self-Trapped States in Dielectric Media. Phys. Rev. B 2005, 71, 161302.

7. Osad'ko, I. S. Power-Law Statistics of Intermittent Photoluminescence in Single Semiconductor Nanocrystals. JETP Lett. 2004, 79, 522-526.

8. Frantsuzov, P. A.; Marcus, R. A. Explanation of Quantum Dot Blinking Without the Long-Lived Trap Hypothesis. Phys. Rev. B 2005, 72, 155321.

9. Heyes, C. D.; Kobitski, A. Y.; Breus, V. V.; Nienhaus, G. U. Effect of the Shell on Blinking Statistics in Single Core-Shell Quantum Dots - A Single Particle Fluorescence Study. Phys. Rev. B 2007, 75, 125431.

10. Verberk, R.; Oijen, A. v.; Orrit, M. Simple Model for the Power Law Blinking of Single Semiconductor Nanocrystals. Phys. Rev. B. 2002, 66, 2332021-2332024.

11. Cichos, F.; von Borczyskowski, C.; Orrit, M. Power-Law Intermittency of Single Emitters. Curr. Opin. Colloid Interface Sci. 2007, 12, 272-284.

12. Tang, J.; Marcus, R. A. Mechanisms of Fluorescence Blinking in Semiconductor Nanocrystal Quantum Dots. J. Chem. Phys. 2005, 123, 054704.

13. Pelton, M.; Grier, D. G.; Guyot-Sionnest, P. Characterizing Quantum-Dot Blinking Using Noise Power Spectra. Appl. Phys. Lett. 2004, 85, 819-821.

14. Chen, Y.; Vela, J.; Htoon, H.; Casson, J. L.; Werder, D. J.; Bussian, D. A.; Klimov, V. I.; Hollingsworth, J. A. "Giant" Multishell CdSe Nanocrystal Quantum Dots with Suppressed Blinking. J. Am. Chem. Soc. 2008, 130, 5026-+.

15. Mahler, B.; Spinicelli, P.; Buil, S.; Quelin, X.; Hermier, J. P.; Dubertret, B. Towards Non-Blinking Colloidal Quantum Dots. Nat. Mat. 2008, 7, 659-664.

16. Pelton, M.; Smith, G.; Scherer, N. F.; Marcus, R. A. Evidence for a Diffusion-Controlled Mechanism for Fluorescence Blinking of Colloidal Quantum Dots. Proc. Natl. Acad. Sci. U. S. A. 2007, 104, 14249-14254.

17. Sher, P. H.; Smith, J. M.; Dalgarno, P. A.; Warburton, R. J.; Chen, X.; Dobson, P. J.; Daniels, S. M.; Pickett, N. L.; O'Brien, P. Power Law Carrier Dynamics in Semiconductor Nanocrystals at Nanosecond Timescales. Appl. Phys. Lett. 2008, 92, -.

18. Hohng, S.; Ha, T. Near-Complete Suppression of Quantum Dot Blinking in Ambient Conditions. J. Am. Chem. Soc. 2004, 126, 1324-1325.

19. Heuff, R. F.; Marrocco, M.; Cramb, D. T. Saturation of Two-Photon Excitation Provides Insight into the Effects of a Quantum Dot Blinking Suppressant: A Fluorescence Correlation Spectroscopy Study. J. Phys. Chem. C 2007, 111, 18942-18949.

20. Jeong, S.; Achermann, M.; Nanda, J.; Ivanov, S.; Klimov, V. I.; Hollingsworth, J. A. Effect of the Thiol-Thiolate Equilibrium on the Photophysical Properties of Aqueous CdSe/ZnS Nanocrystal Quantum Dots J. Am. Chem. Soc. 2005, 127, 10126-10127.

21. Breus, V. V.; Heyes, C. D.; Nienhaus, G. U. Quenching of CdSe-ZnS Core-Shell Quantum Dot Luminescence by Water-Soluble Thiolated Ligands. J. Phys. Chem. C 2007, 111, 18589-18594.

22. Fomenko, V.; Nesbitt, D. J. Solution Control of Radiative and Nonradiative Lifetimes: A Novel Contribution to Quantum Dot Blinking Suppression. Nano Lett. 2008, 8, 287-293.

23. Early, K. T.; McCarthy, K. D.; Hammer, N. I.; Odoi, M. Y.; Tangirala, R.; Emrick, T.; Barnes, M. D. Blinking Suppresion and Intensity Recurrences in Single CdSe-oligo(phenylene vinylene) Nanostructures: Experiment and Kinetic Model. Nanotechnology 2007, 18, 424027.

24. Biebricher, A.; Sauer, M.; Tinnefeld, P. Radiative and Nonradiative Rate Fluctuations of Single Colloidal Semiconductor Nanocrystals. J. Phys. Chem. B 2006, 110, 5174-5178.

25. Khatchadourian, R.; Bachir, A.; Clarke, S. J.; Heyes, C. D.; Wiseman, P. W.; Nadeau, J. L. Fluorescence Intensity and Intermittency as Tools for Following Dopamine Bioconjugate Processing in Living Cells. J Biomed Biotechnol 2007, 2007, 70145.

26. Zhang, K.; Chang, H.; Fu, A.; Alivisatos, A. P.; Yang, H. Continuous Distribution of Emission States from Single CdSe/ZnS Quantum Dots. Nano Lett. 2006, 6, 843-847.

27. Wang, L.-W. Calculating the Influence of External Charges on the Photoluminescence of a CdSe Quantum Dot. J. Phys. Chem. B. 2001, 105, 2360-2364.

28. Ebenstein, Y.; Mokari, T.; Banin, U. Fluorescence Quantum Yield of CdSe/ZnS Nanocrystals Investigated by Correlated Atomic-Force and Single-Particle Fluorescence Microscopy. Appl. Phys. Lett. 2002, 80, 4033-4035.

29. Owen, R. J.; Heyes, C. D.; Knebel, D.; Röcker, C.; Nienhaus, G. U. An Integrated Instrumental Setup for the Combination of Atomic Force Microscopy with Optical Spectroscopy. Biopolymers 2006, 82, 410-414.

30. Yao, J.; Larson, D. R.; Vishwasrao, H. D.; Zipfel, W. R.; Webb, W. W. Blinking and Nonradiant Dark Fraction of Water-Soluble Quantum Dots in Aqueous Solution. Proc. Natl. Acad. Sci. U. S. A. 2005, 102, 14284-14289.

31. Berciaud, S.; Cognet, L.; Lounis, B. Photothermal Absorption Spectroscopy of Individual Semiconductor Nanocrystals. Nano Lett. 2005, 5, 2160-2163.

32. Brokmann, X.; Coolen, L.; Dahan, M.; Hermier, J. P. Measurement of the Radiative and Nonradiative Decay Rates of Single CdSe Nanocrystals through a Controlled Modification of their Spontaneous Emission. Phys. Rev. Lett. 2004, 93, 107403.

33. Tang, J.; Marcus, R. A. Diffusion-Controlled Electron Transfer Processes and Power-Law Statistics of Fluorescence Intermittency of Nanoparticles. Phys. Rev. Lett. 2005, 95, 107401.

34. Kobitski, A. Y.; Heyes, C. D.; Nienhaus, G. U. Total Internal Reflection Fluorescence Microscopy - A Powerful Tool to Study Single Quantum Dots. Appl. Surf. Sci. 2004, 234, 86-92.

35. Chung, I.; Bawendi, M. G. Relationship Between Single Quantum-Dot Intermittency and Fluorescence Intensity Decays from Collections of Dots. Phys. Rev. B 2004, 70, 165304.

36. Dabbousi, B. O.; Rodriguez-Viejo, J.; Mikulec, F. V.; Heine, J. R.; Mattoussi, H.; Ober, R.; Jensen, K. F.; Bawendi, M. G. (CdSe)ZnS Core-Shell Quantum Dots: Synthesis and Optical and Structural Characterization of a Size Series of Highly Luminescent Materials. J. Phys. Chem. B 1997, 101, 9463-9475.

1. 37. Baranov, A. V.; Rakovich, Y. P.; Donegan, J. F.; Perova, T. S.; Moore, R. A.; Talapin, D. V.; Rogach, A. L.; Masumoto, Y.; Nabiev, I. Effect of ZnS Shell Thickness on the Phonon Spectra in CdSe Quantum Dots. Phys. Rev. B 2003, 68, 165306.

38. Borchert, H.; Talapin, D. V.; McGinley, C.; Adam, S.; Lobo, A.; de Castro, A. R. B.; Moller, T.; Weller, H. High Resolution Photoemission Study of CdSe and CdSe/ZnS Core-Shell Nanocrystals. J. Chem. Phys. 2003, 119, 1800-1807.

39. Yu, Z.; Guo, L.; Du, H.; Krauss, T.; Silcox, J. Shell Distribution on Colloidal CdSe/ZnS Quantum Dots. Nano Lett. 2005, 5, 565-570.

40. Empedocles, S. A.; Bawendi, M. G. Quantum-Confined Stark Effect in Single CdSe Nanocrystallite Quantum Dots. Science 1997, 278, 2114-7.

41. Dutta, M.; Stroscio, M. A.; Vasudev, M.; Ramadurai, D.; Torres, L.; West, B. J. Blinking Mechanism of Colloidal Semiconductor Quantum Dots: Blinking Mechanisms. J. Comput. Electron. 2007, 6, 301-304.

42. Sun, Y. H.; Liu, Y. S.; Vernier, P. T.; Liang, C. H.; Chong, S. Y.; Marcu, L.; Gundersen, M. A. Photostability and pH Sensitivity of CdSe/ZnSe/ZnS Quantum Dots in Living Cells. Nanotechnology 2006, 17, 4469-4476.

43. Talapin, D. V.; Rogach, A. L.; Kornowski, A.; Haase, M.; Weller, H. Highly Luminescent Monodisperse CdSe and CdSe/ZnS Nanocrystals Synthesized in a Hexadecylamine-Trioctylphosphine Oxide-Trioctylphospine Mixture. Nano Lett. 2001, 1, 204-211.

44. Peng, Z. A.; Peng, X. Formation of High-Quality CdTe, CdSe, and CdS Nanocrystals Using CdO as Precursor. J. Am. Chem. Soc. 2001, 123, 183-184.

45. Bachir, A.; Durisic, N.; Hebert, B.; Grütter, P.; Wiseman, P. W. Characterization of Blinking Dynamics in Quantum Dot Ensembles using Image Correlation Spectroscopy. J. Appl. Phys. 2006, 99, 064503.

In the previous chapter we characterized changes in the blinking statistics and dark fraction of the QDs caused by variation in pH of their surrounding environment. All changes were observed to be irreversible. Given the theoretical blinking models which include diffusion controlled mechanisms responsible for the QD blinking, it is plausible to assume that if the mere presence of protons was the only cause of the observed changes, once their concentration was lowered, the QD fluorescence would recover if the reaction were reversible. However we have shown that this is not the case so some permanent changes to the shell or the core of the QDs must occur. Since we did not observe any obvious signs of aggregation and did not record a spectral shift of the emission maximum, we were able to rule out the possibility that polymer coating comes off from the shell and that strong oxidation of the core takes place. This implies that more subtle changes, most probably to the shell, occur and affect electron-hole recombination.

In the next chapter we examine these assumptions and propose possible chemical modifications of the shell that would involve the formation of irreversible trap states.

Chapter 7

7. Ensemble and Single Particle Emission Properties of CdSe/ZnS Quantum Dots in Biologically Relevant pH Range

7.1 Introduction

The use of semiconductor quantum dots (QDs) for fluorescent tagging of biomolecules has experienced rapid and continued growth since the first reports of such applications in 1998 (1, 2). Their commercial availability and the development of reproducible synthesis methods have provided researchers in wide-ranging fields with an ever increasing toolbox to answer biological and biophysical questions. Many biophysical studies to date have used the QDs effectively as a brighter and more photostable replacement of organic dyes, e.g. immunofluorescent staining of intracellular and extracellular components and long timescale tracking of biomolecules, both in vitro and in vivo. Single QD-labeled biomolecules have yielded interesting insights into diffusion of membrane-bound receptors (3, 4), clustering of proteins such as transferrin (1) , movement of motor proteins (5), cancer detection (6, 7) and cellular compartmentalization (2).

Despite these attractive applications, one must be careful while extracting quantitative information from QD emission since their fluorescence properties are complex. The quantum yield of a single particle has been shown to be significantly different from the ensemble quantum yield, due to the presence of a significant dark fraction in a given sample (8-10). This dark fraction has been shown to be highly dependent on sample quality and experimental conditions, particularly pH (11, 12). Furthermore, non-radiative relaxation pathways may be enhanced by the presence of surface trap states. Surface trap states can be deep or shallow in energy relative to the band edge emission (13). Shallow trap emission is generally energetically indistinguishable from band edge emission, but has a longer fluorescence lifetime (14). Therefore, fluorescence lifetime curves monitored at the band edge are generally multi-exponential due to the contribution from these surface states. Deep traps are much lower in energy (red-shifted by more than 100 nm) and usually have weak emission (15).

Connecting the observed microscopic optical properties of single QDs to the macroscopic optical properties of a quantum dot ensemble is necessary to be able to use QDs for quantitative biophysical studies. In particular it is import to know precisely single QD brightness to be able to determine concentration of QDs in an ensemble. This is particularly important in cellular environments, where intracellular pH changes may also affect the optical properties of QDs. The concentration of QDs in cells is often calculated using their fluorescence intensity and ensemble quantum yield. However, the change of the dark fraction and changes in quantum yield can result in an underestimation of the concentration.

This discrepancy will have significant effects on both quantitative assays and toxicology, in which cells may be adversely affected by high concentrations of non-fluorescent QDs.

In this study, we have attempted to gain a more thorough understanding of the optical properties of QDs both at the single particle and ensemble level under a physiologically relevant range of pH from 6 to 9. We found that pH strongly affects the ensemble optical properties (both intensity and fluorescence lifetime) as well as the photochemical stability. We relate the ensemble properties to the previously reported single particle properties such as dark fraction and blinking to connect the mollecular origin of the pH effects in terms of current blinking and photochemical stability models (12).

7.2 Experimental

Materials.

Samples of CdSe/ZnS quantum dots were purchased from Invitrogen Canada Inc. (Burlington, ON). We used streptavidin functionalized CdSe/ZnS quantum dots (QD605-streptavidin) with emission wavelength centered at 605 nm.

To prepare buffered solutions with pH values ranging from 9 to 6 and examine effects of Lewis acid or base on QD fluorescence, HCl or NaOH was added to PBS buffer (Fisher Scientific, Pittsburgh, PA). Tries (2-carboxyethyl) phosphine (TCEP) (Sigma-Aldrich, St. Louis, MO) was diluted down to 20 mM in buffered solutions of various pHs and used to remove oxygen as needed.

Sample preparation.

Attachment of QDs to the glass surface was performed as previously described (12). Briefly, microscope cover glass (Fisher Scientific, No. 1) were first cleaned in Piranha solution (3:1 concentrated sulfuric acid:30% hydrogen peroxide) and then amino-functionalized with 3-aminopropyltriethoxylsilane (Pierce, Rockford, IL). Next the amino groups were modified with a 10 mM aqueous Sulfo-LC-SPDP solution (Pierce, Rockford, IL) and exposed to reduced biotinilated BSA (Pierce, Rockford, IL) to form covalent bonds with the protein. The QD605-streptavidin stock solution (2 μM) was diluted by a factor of 10^6 in MiliQ water (>18 MΩcm^{-1}) and sonicated for 15 min prior to deposition on biotinilated glass. In imaging experiments, pH buffered solutions were added directly to the glass-immobilized QDs and measured immediately.

Ensemble emission experiments were prepared by diluting the QD stock solution ~10^3 fold in pH- adjusted PBS buffer and placed in cuvettes immediately prior to data collection.

Methods and Instrumentation.

Steady-State Fluorescence. Fluorescence emission spectra and steady state decay kinetics were measured on a Thermo Spectronic spectrofluorometer, Aminco-Bowman series 2, (Rochester, NY, USA). Emission spectra were collected with 1nm spectral resolution in the range from 550nm to 700nm.

Time-Resolved Fluorescence. The nanosecond lifetime histograms were measured using time-correlated single photon counting method. As a pulsed excitation source, we used a PDL 800B diode laser (Picoquant, Germany) with emission wavelength at 470 nm, pulse duration 70 ps, and pulse repetition rate 2.5 MHz. For data acquisition we used a TimeHarp 200 system (PicoQuant, Germany) and recorded decay kinetics in 2900 time channels.

Single QD Fluorescence. Images of spatially resolved single quantum dots deposited on a glass surface were recorded on a home built objective-type total internal reflection fluorescence microscope (TIRFM) equipped with intensified

PentaMax charge-coupled device (CCD) camera (Princeton Instruments, Trenton, NJ). The 488nm line from an Ar+ laser (Melles Griot 35 LAP 431) was used for excitation through a Zeiss Planapo 100x, 1.45NA objective lens. Fluorescence from the sample plane was collected with the same objective and filtered with an emission filter D605/55 nm (Croma Technology, Rockingham, VT). All image time series were 2000 frames long with 50ms time resolution.

Electron Microscopy. 1μl of QD stock solution was deposited on a TEM grid and left to dry for 2 hours in a desiccator. TEM images of dried particles were recorded on a Philips CM200 electron microscope operating at 200 kV.

Data Analysis.

Histogram analysis of fluorescence from spatially resolved QDs was performed using home-made software written in Matlab 6.5 (Mathworks, Natick, MA) as previously described (12, 16, 17). The software extracts the fluorescence time trace from a time-integrated image of each dot in the image sequence and determines “On” and “Off” time durations by setting a threshold level to 2σ of the background signal around the dot. This procedure is repeated for several hundred individual QD. Then durations of times spent in the “Off” state and “On” state is calculated from all the extracted traces and plotted as a probability histogram.

Processing of fluorescence lifetime data was done using a Matlab routine originally developed by Enderlein *et al.* with slight modification (18). The algorithm was capable of fitting as well as performing numerical reconvolution to account for finite instrument response function. Since all our fluorescence decay curves had multi-exponential character we avoided predicting a form of fitting function by approximating a sum of decaying exponentials as

$$I = \Sigma\, a_i \exp(-t/\tau_i), \qquad (1)$$

where τ_i and a_i are respectively the decay times and the corresponding coefficients in the multi-exponential decay model. We assigned 100 fixed values to parameters τ_i spanning the range τ_{min}=0 to τ_{max}=2900 (the number of time channels), distributed equally as log(τ), and fit for the a_i coefficients. This type of analysis resulted in a histogram of characteristic exponential decay times weighted according to their contribution to the fit. This method allowed us to determine the number of exponential components, their charachteristic decay times, uncertainties and relative weights.

7.3 Results

Figure 1(a) shows the fluorescence intensity of QDs as a function of pH between pH 6 and 9, while Figure (b) shows the same data normalized to 1 to highlight the fact that there is only a decrease in the fluorescence intensity and no shift in the emission peak over this pH range.

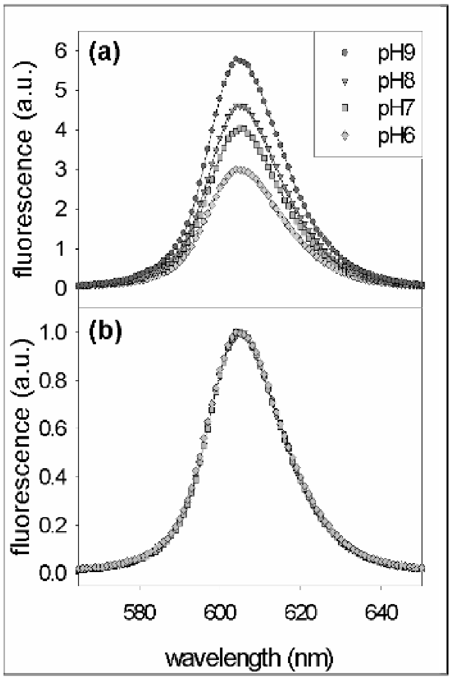

Figure 1

Effect of pH on emission spectra. Fluorescence decreases with pH (a), but the peak position does not change (b) indicating that the core size stays the same. Spectral resolution was 1nm.

Figure 2 shows representative fluorescent time traces of individual quantum dots at various pHs together with the sample area from where the trace is extracted (inset). As the pH is lowered from 9 to 8, there is a reduction in the single QD "on" time emission intensity, while the number of emitting dots is not so strongly affected. Only once the pH drops below 8, the dark fraction formation becomes more prominent. This implies that the large decrease in the ensemble emission intensity between pH 9 and 8 in Figure 1 is caused mainly by increase in non-radiative decay rates during "on" times, but between 7 and 6 the reduction occurs primarily because of the decrease in the number of fluorescent QDs.

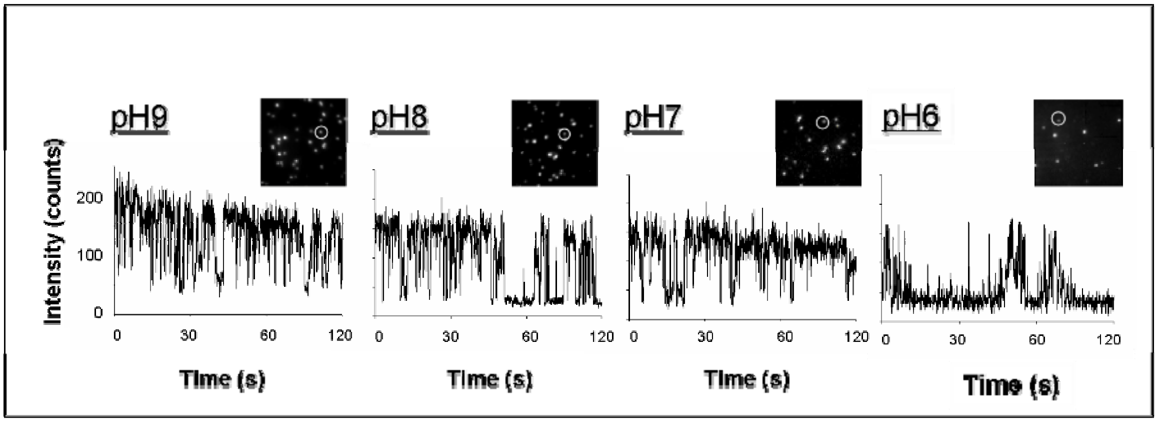

Figure 2

(a) Fluorescence time traces of single QDs in different pH environments extracted from image series of spatially resolved QDs attached to the glass surface. In the inset sum of images from an image sequence is shown with circled QD whose time trace is presented. As pH is lowered from 9 to 8, a decrease in QD brightness is more pronounced than the change in bright fraction. Only in more acidic environments a decrease in bright fraction becomes more pronounced than the change in brightness. Statistical analysis reveals the change in blinking dynamics, which is otherwise evident only in pH 6 time traces. Images were recorded on a CCD detector with time resolution of 50ms.

The change in blinking dynamics between pH9 and pH7 can not be detected by the naked eye. However, our previous study showed that probability to observe long “on” times decreases over that range (12). At pH6 long “off” times are clearly dominant and fluorescent time traces have strong resemblance to time traces of poorly passivated CdSe cores. This behavior highlights the fact that the ensemble fluorescence intensity is related to the single-particle optical properties in a very complex way, and includes the effects of blinking as well.

Figure 3(a) shows how the intensity of the emission peak changes with time of exposure to the pH solutions.

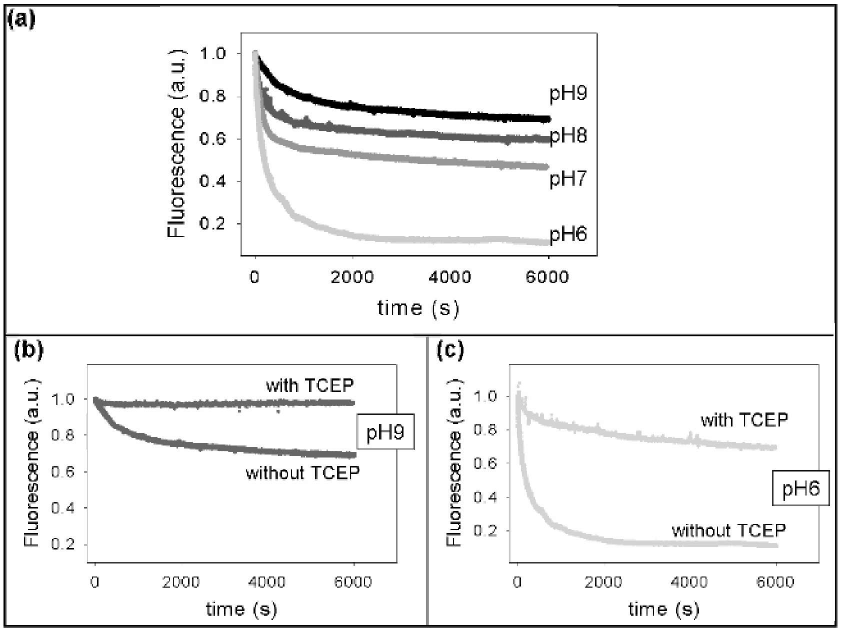

Figure 3

(a) Steady state fluorescence decay curves of freely diffusing nanocrystals as a function of pH. The decay rate increases as pH decreases. (b) and (c) show effect of oxygen removal on fluorescence quantum yield of QDs in pH9 and pH6, indicating that both oxygen and H^+ are involved in the decay. Each measurement was taken at 605nm with 1s resolution time.

The fluorescence decays in a complex manner, the rate increasing with decreasing pH. All decays are normalized at t=0. After about 30min, a plateau was reached with the fluorescence reduced for 34% of the initial value at pH 9 and for 88% at pH 6. Several factors can account for this. The commercial QDs used here consist of a CdSe core, an inorganic ZnS shell, an organic polymer layer and in this case, conjugate streptavidin protein molecules. Salts present in the PBS buffer may also act as quenchers. We examined how ionic strength of the solution affects steady-state fluorescence by changing potassium phosphate and sodium chloride content in the solution and did not discover any changes in the emission (data not shown). To investigate weather presence of dissolved oxygen in the solution affects photostability of QDs we introduced TCEP, which is known to effectively remove oxygen without changing pH. Figures 3(b) and 3(c) compare intensity decays with and without oxygen removal. In the buffer with pH 9, fluorescence stays constant when oxygen is removed, while in the solution with pH 6 it decays for only 25% over 100 min, suggesting that oxygen plays a significant role in QD photostability. Sark et al. have previously shown that oxygen induced photooxidation leads to QD bleaching (19). We believe that photooxidation of the core is less likely to be a reason for loss of fluorescence as it is preceded by a blue shift in emission peak, which we do not observe. However, chemical changes in QD shell, or on core-shell interface would affect recombination of photoinduced charge carriers (excitons) and change the optical properties of QDs.

Information on exciton dynamics can be obtained from fluorescence lifetime measurements. Given that steady-state experiments (Figure 3) indicate that most of changes in emission signal occurred during the first 30 min of QD exposure to the buffer, we measured nanosecond decay kinetics every 60s for 30 min for each pH value. Figure 4(a) shows the representative fluorescence decay curve together with the best fit line and residuals. The corresponding histogram of recovered decay times is plotted in figure 4(b). Four distinct time constants were typically found for all data sets and are tabulated in table (1).

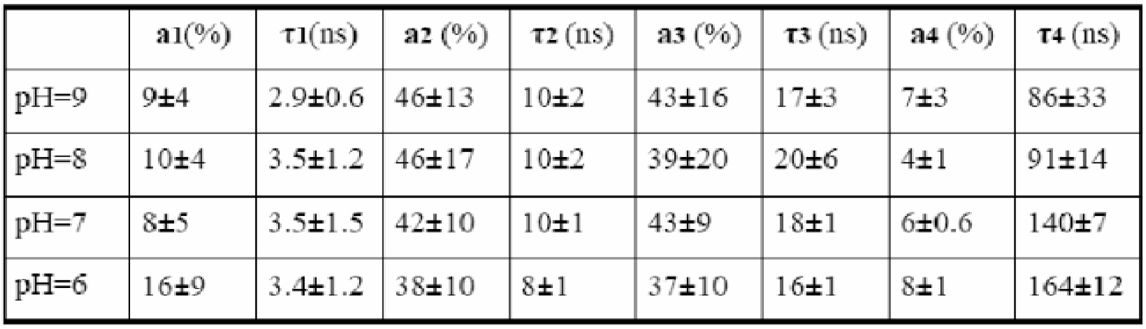

	a_1(%)	**τ_1(ns)**	**a_2 (%)**	**τ_2 (ns)**	**a_3 (%)**	**τ_3 (ns)**	**a_4 (%)**	**τ_4 (ns)**
pH=9	9±4	2.9±0.6	46±13	10±2	43±16	17±3	7±3	86±33
pH=8	10±4	3.5±1.2	46±17	10±2	39±20	20±6	4±1	91±14
pH=7	8±5	3.5±1.5	42±10	10±1	43±9	18±1	6±0.6	140±7
pH=6	16±9	3.4±1.2	38±10	8±1	37±10	16±1	8±1	164±12

Table 1

Fit parameters of the lifetime data collected from QDs exposed to buffered solutions whose pH varied from 9 to 6. Each value is an average of 30 consecutive measurements. Uncertainties are standard deviations.

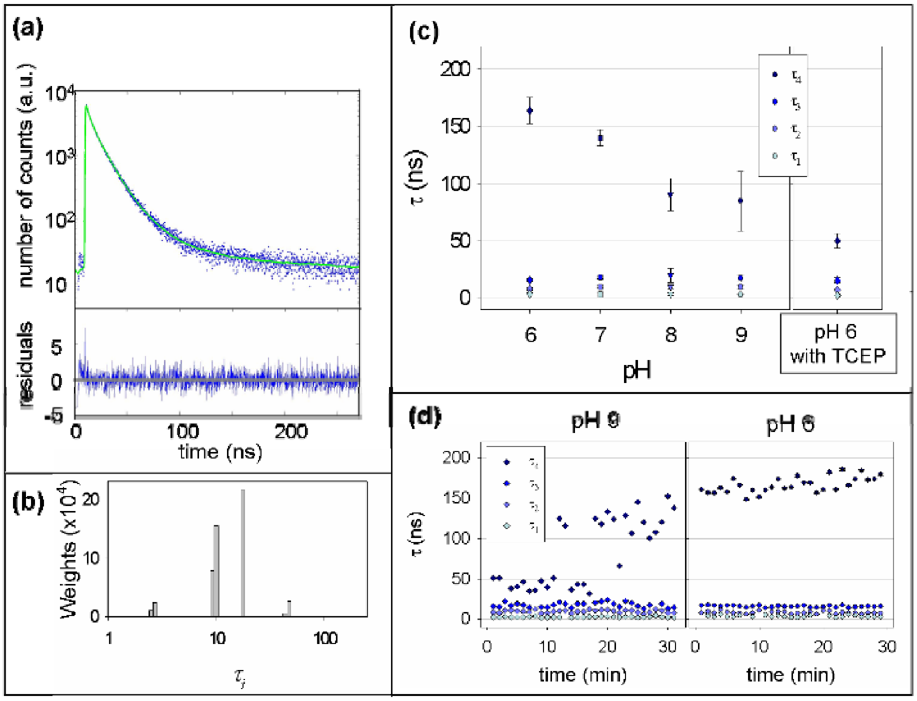

Figure 4

(a) A representative fluorescence decay kinetics of CdSe/ZnS streptavidin functionalized nanocrystals (blue dots), the best fit line to the data (green) and corresponding weighted residuals. For each pH a similar decay was measured every minute for 30 min, starting at 5 s after exposure of QDs to buffered solution.

(b) Distribution of time constants (τi) obtained from fits of lifetime decay curve in (a) to a sum of decaying exponentials $I = \Sigma\ ai\ \exp(-t/\tau i)$. We assigned 100 fixed values to parameters τi equally distributed on a log (time) axis in (a). The range of 1- 2800ns was included in to analysis. Four lifetime values were recovered for each decay curve.

(c) A plot showing how average value of each lifetime component changes as a function of pH. Error bars are standard deviation of 30 consecutive measurements. For comparison, recovered decay constants for QDs in pH 6 solution with TCEP are shown to the right. Component τ_4 has significantly smaller value than when oxygen is present and reaction (1) is feasible.

(d) The dependence of decay constants as a function of time for low H^+ content (pH 9) and high H^+ content (pH6). The longest decay time τ_4, changes over time of QD exposure to pH 9. In pH 6 its change is much faster and not possible to resolve. The other three lifetime components remain unchanged suggesting that presence of protons in QD surrounding affects only one fluorescence decay configuration.

For all pHs, components τ_2 = (9+/-2) ns and τ_3 = (18+/-3) ns account for nearly 80% of the decay. They do not change in time and show similar values for each pH (figure 4 c and d). τ_1= (3+/-1) ns also appears to be constant and τ_4 showed an increase as pH was lowered. As expected, for each subsequent run a decrease in total number of counts was observed and was most pronounced for decay curves obtained for QDs in pH 6 buffer.

Finally, to estimate the shape, shell thickness and homogeneity of QD samples we recorded transmission electron microscopy (TEM) images of dried nanocrystals and found that the ZnS shell was elongated with an average length of (12.5+/-1.1) nm and width of (4.2+/-0.6) nm (Figure 5).

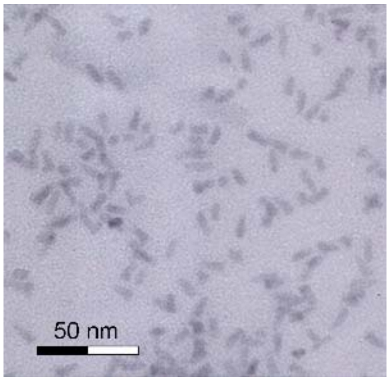

Figure 5

TEM characterization of CdSe/ZnS streptavidin functionalized QDs showing that ZnS shell is highly inhomogeneous and rod-like in shape.

7.4 Discussion

A comprehensive picture connecting the microscopic and macroscopic optical properties of QDs has so far been lacking; one of the aims of this study was to bridge such a gap. We have observed a strong effect of pH on the optical properties of QDs, which is apparent on both the ensemble and single particle level. The ensemble fluorescence intensity as well as the number of observed fluorescent QDs decreased strongly with pH, however, they did not decrease linearly. The fact that an ensemble fluorescence intensity decreased more strongly than the bright fraction between pH 9 and 8, shows that in contrast to common belief, ensemble quantum yield of QDs in biologically relevant environment is not just determined by bright to dark fraction ratio (8, 9). Quantum yield of bright dots is also susceptible to changes.

The effect of pH on fluorescence intensity and dark fraction was found to be irreversible; immersing QDs in pH 9 solution after being exposed to pH 6 did not recover the fluorescence. The observation that reducing pH caused a faster and more pronounced decrease in the fluorescence intensity upon exposure to the pH solution (Figure 3) demonstrates that protons likely effected a chemical change to the QD. The fact that the fluorescence spectrum does not change with pH (Figure 1(b)) suggests that the core size was unaffected by pH, and that any chemical changes occurred only at the core surface or in the shell.

Removing oxygen from the solution by the addition of TCEP significantly reduced the rate and extension of the reaction. These results suggest that both H^+ and O_2 are involved in the reaction. One can imagine that the low-density organic layers are easily penetrated by both H^+ and O_2. We analyzed the homogeneity and isotropy of the shell by TEM (Figure 5) and found that the core-shell QDs existed in rod-like structures, highlighting the non-isotropic ZnS shell. We estimate that the thickness of the ZnS shell varies from 1 to more than 4 monolayers both within a single QD and from QD to QD. This means that the structure of the shell changes from amorphous phase typical for thin regions, to partly crystalline thick areas providing a well passivated core surface without exposing it to high surface stress due to the lattice mismatch of ZnS and CdSe (20). We next consider possible chemical changes of ZnS shell, which can lead to formation of trap states and how they can affect optical properties of QDs.

We hypothesize that thin sections of the ZnS shell may be exposed to the process described by the following chemical reactions, slowly corroding the shell, and possibly exposing the CdSe cores. ZnS is stable under normal conditions; the dissociation of ZnS directly into Zn^{2+} and S^{2-} has a $\Delta G = +139.4$ kJmol^{-1}. However, in the presence of acid and oxygen, the reaction:

$$ZnS_{(s)} + 2H^{+}_{(aq)} + \frac{1}{2}O_{2(aq)} \rightarrow S_{(s)} + Zn^{2+}_{(aq)} + H_2O_{(l)} \tag{2}$$

has a $\Delta G = -81$ kJmol^{-1} and a low activation energy, Ea=25kJmol^{-1}, highlighting that the reaction is diffusion controlled, and thus highly dependent on pH and O_2 concentration. Oxidative dissolution of ZnS can start by proton binding and attack to $>S^{2-}$ to form surface $>SH_2$ sites, which can then transform into $> S_m^{2-}$ sites by reaction with O_2 and release of Zn^{2+} into solution. The polysulfide groups would then form a poorly ordered sulfur-rich layer (SRL), which would inhibit further Zn^{2+} dissolution.

$$(> S^{2-})_{QD} + 2H^{+}_{(aq)} \Leftrightarrow (> SH_2)_{QD} \tag{3}$$

$$x(>SH_2)_{QD}+\frac{x}{2}(1-\frac{1}{y})O_{2(aq)} \Leftrightarrow \frac{x}{y}(S_m^{2-})_{QD}+x(1-\frac{1}{y})H_2O_{(l)}+2\frac{x}{y}H^+_{(aq)} \quad (4)$$

A similar mechanism was proposed for oxidation of FeS in oxygen-bearing acidic solution (21). The formation of $>S_m^{2-}$ is a self-inhibiting process due to the SRL blocking access of O_2 to ZnS, which leads to a saturation point in the extent of reaction. Figure 3 agrees with this saturation effect, which shows a leveling off of the fluorescence intensity with time of exposure to the solution and dependence on both pH and O_2. We expect the rate of reaction (4) to be higher at first as atoms in amorphous regions of the shell are more loosely bound than those in crystalline layers. Once crystalline regions start to oxidize, the rate should decrease and the reaction will reach saturation when enough S_m^{2-} is formed to block access of O_2. However debate still exists as to whether the oxidation proceeds with the formation of $>S_m^{2-}$ or elemental sulfur, S^0. Still, due to the insolubility of S^0 in water and the difficulty to form the stable S_8 allotrope without significant rearrangement, the elemental sulfur likely remains bound to the surface of the QD. In any case, its formation is strongly dependent on pH and O_2. When O_2 content is lowered by TCEP the fluorescence intensity decays far less than with oxygen present (at either pH 6 or 9) giving support to the mechanisms above. In the various possible (and complex) forms that sulfur can exist on the QD surface, some of them could act as trap states, particularly for the binding of H^+ to the surface and the formation of a poorly-ordered SRL (*vide infra*), thereby reducing the fluorescence intensity and increasing blinking as previously reported (12). In the environment of the QD surface, where the polymeric stabilizing ligands contain complexation moieties (such as C=O groups), the Zn^{2+} may not enter the solution as free ions, but may remain close to the QD surface and contribute to trap states.

Once formed, the further oxidation of $S_{(s)}$ to $SO_{2(g)}$ is thermodynamically allowed ($\Delta G_f(SO_2)$ = -300.1 kJmol^{-1}) but is very slow, and may eventually form bisulfite and sulfite by

$$S_{(s)} + O_{2(aq)} \rightarrow SO_{2(g)} \qquad (5)$$

$$SO_{2(g)} + H_2O_{(l)} \rightarrow HSO^{-}_{3(aq)} + H^{+}_{(aq)} \overset{pK_a\,7.0}{\Leftrightarrow} SO^{2-}_{3(aq)} + 2H^{+}_{(aq)} \qquad (6)$$

Thus, over long periods of time, sections of the shell can corrode in the presence of acid and oxygen. It is unlikely that much SO_2 will be released under our experimental conditions. At the far extreme of low pH and high oxygen concentration, the oxidation may eventually penetrate to the CdSe core material and expose it to the solution, the following reaction could occur:

$$CdSe_{(s)} + 2H^{+}_{(aq)} + 1\tfrac{1}{2}O_{2(aq)} \rightarrow SeO_{2(s)} + Cd^{2+}_{(aq)} + H_2O_{(l)} \qquad (7)$$

SeO_2 has been observed by XPS for uncapped CdSe QDs exposed to air over a 24h time period (22), thus the oxidation of Se is a very slow process, especially in aqueous solution, where the concentration of O_2 is limited. Once formed, however, SeO_2 is water soluble and can eventually lead to the complete dissolution of the CdSe.

$$SeO_{2(s)} + H_2O_{(l)} \rightarrow H^+_{(aq)} + HSeO^-_{3(aq)} \overset{pK_a\,8.3}{\Leftrightarrow} 2H^+ + SeO^{2-}_{3(aq)} \qquad (8)$$

Such an extent of oxidation is not evident in the pH range of 6-9 and for the core-shell QDs used here. At pH ≥ 6, we hypothesize that the corrosion is confined to thin sections of the ZnS shell. This hypothesis is in agreement with an observation that a large fraction of the single QDs no longer fluoresce, but they are still present as observed by AFM (12). Furthermore, the lack of an observed shift in the fluorescence spectrum and the insensitivity of fluorescence lifetime components also support the hypothesis that the reaction is primarily located in the shell.

When QDs are illuminated with above band gap light, proposed oxidation of ZnS shell will undergo electron-active photooxidation and the above reactions will be accelerated. In accordance with the electron-active photooxidation model (23, 24), excitonic wavefunctions that tunnel into the thin areas of the ZnS shell catalyze the dissociation of molecular oxygen in to oxygen radicals. If oxygen radicals feature as oxidative species instead of molecular oxygen, the rate of all above reactions will increase making illuminated QDs even more sensitive to pH variations of their surrounding. This is also in agreement with our observations;

the effect of pH-buffered solutions on single QD brightness was more pronounced when QDs were exposed to laser illumination over longer periods of time. For example, during the time it takes to collect one image sequence at pH6 (~5 min) almost all initially bright dots on the glass surface become permanently "off", while changing the observation area of the sample after those 5 min reveals that approximately 60% of dots are still capable of emitting.

Previous analysis of QD blinking on the same samples also showed an effect of pH; the probability of observing long "on" times decreased while the probability of observing long "off" times increased as pH was lowered. We had previously hypothesized that there was an intrinsic connection between the blinking mechanism and the mechanism rendering the QDs dark (12). The pH effect on blinking was interpreted as the H^+ ions interacting with the core surface to facilitate the trapping of charge carriers, which has been associated with the "off" state. In one model, based on the Tang-Marcus model, the H^+ ions interact with the QD, affecting the potential energy curves of the bright and/or dark state and, by extension, their overlap, hence, modifying the trapping and detrapping rates (25, 26). In a second model, based on the Frantsuzov-Marcus model, the H^+ ions effect a change which increases the number of hole-trap states (27). In the latter model, stochastic diffusion of electronic energy levels is responsible for switching between a resonance condition in which Auger-assisted trapping occurs to produce the “off” state and a non-resonance condition in which the QD is “on”. More trap states increase the time for which the resonance condition is met. Above a certain threshold of trap states, this condition is always met and the QD is permanently “off” (contributing to the dark fraction). These models connect the two single molecule phenomena of blinking and dark fraction. Whether it is the H^+ ion directly through modification of local electric field, or a product of the H^+ reacting with the ZnS shell to form the products described above, these blinking models (and our connection of them to the dark fraction) should hold independent of the exact nature of the trap state, provided that the transition to the dark state depends on how the number and/or energies of these trap states change with pH. The observation of a reduction in the maximum “on” state intensity with decreasing pH is also consistent with the formation of trap states on the QD surface, which act to change the overlap integral of the electron and hole wave functions in the “on” state (28). Formation of these trap states also results in faster blinking dynamics reducing the number of photons emitted within the milisecond time bin (see figure (2), pH6). The changes in dark fraction, blinking statistics and “on” state intensity all contribute to a change in the ensemble fluorescence intensity (quantum yield) in a complex way. In this report and our previous study, we have decomposed these individual effects and compared them to the ensemble fluorescence intensity.

Trap states formation also affects exciton lifetime. In a recent study by Jones *et al.*, the authors found that at least 2 distributions of trap states exists; electron or hole traps localized mainly on outermost ZnS surface and interfacial trap sites localized near CdSe core (29). We will refer to them as “surface traps” and “core traps” respectively. Relating ensemble and single QD decays, they modeled lifetime decay with components around ~10 ns, ~20-60 ns and ~100-250 ns. This is in excellent agreement with our data of Figure 4, where we found lifetime components in these ranges (without *a priori* assuming the form of the decay), as well as another one with low amplitude around 2-4 ns. The majority of the decay in our samples occurred from the ~10 ns and ~20 ns components, again in excellent agreement with Jones *et al.* The slowest component, which was assigned to surface traps are shown here to be pH dependent (becoming slower as pH is lowered, Fig. 4 (c)), whereas the faster components are pH independent, and can be assigned to intrinsic exciton emission and core trap emission, respectively. The slow lifetime component in pH 9 solution does eventually increase to the same value as at pH 6, where it gradually changed from 43.7 ± 6.4 ns during the first 10min to 103.5 ± 35.8 ns over the last 20min

(Fig. 4(d)), presumably as the few H^+ ions in solution (with dissolved O_2) eventually react with the ZnS shell. The pH-dependent lifetime component is also affected by removing O_2, where adding TCEP to the pH 6 solution results in that component being the same as in pH 9 solution (Fig 4 (c)), lending further support to the assignment of surface traps and to the chemical reactions described above. Applying the model that the slow component is due to surface traps, and the hypothesis that H^+ ions can affect the number and/or surface trap energy through $>S_m^{2-}$ formation, blinking can be strongly affected by electron or hole becoming trapped in these long-lived surface trap states. In the Frantsuzov-Marcus model, trapping is accomplished by the surface hole-trap energy being in resonance with the $1S_e$ to $1P_e$ electronic transition energy. Random fluctuations of the $1S_e$ to $1P_e$ transition energy results in power law dynamics of blinking. If a large number of trap states exists (above a certain threshold), the resonance condition is always met, and QD is turned permanently “off”. This results in the formation of a dark fraction of QDs. The observation that pH effects on blinking and dark fraction are irreversible can be explained by irreversibility of the chemical reactions described above.

Jones *et al.* assumed spherical symmetry for both sets of trap distributions. Our TEM images of figure 5 show that core-shell QD samples are not always spherical, and that spherical symmetry is not always an applicable assumption, especially for the surface trap states. Appropriate symmetry depends highly on the QD samples used. The surface trap states which are occupied most readily are those closest to the core because they are the most assessable to electron and hole wave functions. In our case those are the thin regions of the shell.

Core trap states, regardless of wether they are neutral or charged, affect radiative recombination rates because they lower the symmetry of the system and lead to mixing of forbidden (dark) and allowed (bright) excitonic transitions (30). Radiative lifetimes of neutral and positively charged nanocrystal core with and without hole trap close to the interface with ZnS shell are similar but not identical and can be associated with fast lifetime components in our measurements. Changing surface-trap states on the outer surface of ZnS shell by pH is less likely to affect distant direct exitonic emission, but can affect lifetime of a population of surface trap states. This would affect single particle quantum yield, blinking, dark fraction and cause changes of the slowest component of multi-exponential fluorescence decay of a bulk solution of QDs.

In summary, we have performed a thorough, systematic study of the effects of pH on the ensemble fluorescence properties of QDs, their photochemical stability and their single particle fluorescence properties. We found an irreversible decrease in the ensemble fluorescence intensity, a decrease in the brightness of single QDs and an increase in the dark fraction with decreasing pH from 9 to 6. The irreversible decay in fluorescence intensity with time was monitored following exposure to the pH solution both with and without the addition of the oxygen scavenger, TCEP. Both H^+ and O_2 were found to be important for the fluorescence decay, suggesting that a proton-catalyzed oxidation process is responsible for the decay. Fluorescence lifetime analysis showed that the longest component, attributed to trap states primarily localized on the outer ZnS shell surface, increased with time. This result, taken with the lack of shift in the fluorescence spectrum with pH, suggests that the reactions occurred only at the QD surface but not in the core. The change in blinking statistics with pH, in which shorter “on” times and longer “off” times are observed with decreasing pH, are related to formation of deep trap states on the shell surface due to the reaction with H^+ thus affecting the probabilities of interchange between bright and dark states. Above a certain threshold number of trap states formed, the QD is trapped in a permanent “off” state thus contributing to an increase in the dark fraction. These results provide compelling support that a common mechanism underlies the dark fraction formation, fluorescence blinking and fluorescence lifetime of quantum dots, and provides a microscopic physical and chemical basis for our observations.

References

1. Chan, W. C., and S. Nie. 1998. Quantum dot bioconjugates for ultrasensitive nonisotopic detection. Science 281:2016-2018.
2. Bruchez, M., Jr., M. Moronne, P. Gin, S. Weiss, and A. P. Alivisatos. 1998. Semiconductor Nanocrystals as Fluorescent Biological Labels. Science 281:2013-2016.
3. Lidke, D. S., P. Nagy, R. Heintzmann, D. J. Arndt-Jovin, J. N. Post, H. E. Grecco, E. A. Jares-Erijman, and T. M. Jovin. 2004. Quantum dot ligands provide new insights into erbB/HER receptor-mediated signal transduction. Nat Biotechnol 22:198-203.
4. Bates, I. R., B. Hebert, Y. Luo, J. Liao, A. I. Bachir, D. L. Kolin, P. W. Wiseman, and J. W. Hanrahan. 2006. Membrane Lateral Diffusion and Capture of CFTR within Transient Confinement Zones. Biophys. J. 91:1046-1058.
5. Mansson, A., M. Sundberg, M. Balaz, R. Bunk, I. A. Nicholls, P. Omling, S. Tagerud, and L. Montelius. 2004. In vitro sliding of actin filaments labelled with single quantum dots. Biochem. Biophys. Res. Comm. 314:529-534.

6. Akerman, M. E., W. C. Chan, P. Laakkonen, S. N. Bhatia, and E. Ruoslahti. 2002. Nanocrystal targeting in vivo. Proc. Natl. Acad. Sci. U. S. A. 99:12617-12621.

7. Wu, X., H. Liu, J. Liu, K. N. Haley, J. A. Treadway, J. P. Larson, N. Ge, F. Peale, and M. P. Bruchez1. 2002. Immunofluorescent labeling of cancer marker Her2 and other cellular targets with semiconductor quantum dots. Nat. Biotechnol. 21:41-46.

8. Ebenstein, Y., T. Mokari, and U. Banin. 2002. Fluorescence quantum yield of CdSe/ZnS nanocrystals investigated by correlated atomic-force and single-particle fluorescence microscopy. Appl. Phys. Lett. 80:4033-4035.

9. Yao, J., D. R. Larson, H. D. Vishwasrao, W. R. Zipfel, and W. W. Webb. 2005. Blinking and nonradiant dark fraction of water-soluble quantum dots in aqueous solution. Proc. Natl. Acad. Sci. U. S. A. 102:14284-14289.

10. Brokmann, X., L. Coolen, M. Dahan, and J. P. Hermier. 2004. Measurement of the Radiative and Nonradiative Decay Rates of Single CdSe Nanocrystals through a Controlled Modification of their Spontaneous Emission. Phys. Rev. Lett. 93:107403.

11. Gao, X., W. C. W. Chan, and S. Nie. 2002. Quantum-dot nanocrystals for ultrasensitive biological labeling and multicolor optical encoding. Journal of Biomedical Optics 7:532-537.

12. Durisic, N., P. W. Wiseman, P. Grutter, and C. D. Heyes. 2009. A Common Mechanism Underlies the Dark Fraction Formation and Fluorescence Blinking of Quantum Dots. ACS Nano.

13. Pokrant, S., and K. B. Whaley. 1999. Tight-binding studies of surface effects on electronic structure of CdSe nanocrystals: the role of organic ligands, surface reconstruction, and inorganic capping shells. Eur. Phys. J. D 6:255-267.

14. Nirmal, M., C. B. Murray, and M. G. Bawendi. 1994. Fluorescence-line narrowing in CdSe quantum dots: Surface localization of the photogenerated exciton. Physical Review B 50:2293.

15. Underwood, D. F., T. Kippeny, and S. J. Rosenthal. 2001. Charge carrier dynamics in CdSe nanocrystals: implications for the use of quantum dots in novel photovoltaics. Eur. Phys. J. D 16:241-244.

16. Kobitski, A. Y., C. D. Heyes, and G. U. Nienhaus. 2004. Total internal reflection fluorescence microscopy - a powerful tool to study single quantum dots. Appl. Surf. Sci. 234:86-92.

17. Heyes, C. D., A. Y. Kobitski, V. V. Breus, and G. U. Nienhaus. 2007. Effect of the Shell on Blinking Statistics in Single Core-Shell Quantum Dots - A Single Particle Fluorescence Study. Phys. Rev. B 75:125431.

18. Enderlein, J., and R. Erdmann. 1997. Fast fitting of multi-exponential decay curves. Optics Communications 134:371-378.

19. van Sark, W. G. J. H. M., P. L. T. M. Frederix, D. J. Van den Heuvel, H. C. Gerritsen, A. A. Bol, J. N. J. van Lingen, C. de Mello Donega, and A. Meijerink. 2001. Photooxidation and Photobleaching of Single CdSe/ZnS Quantum Dots Probed by Room-Temperature Time-Resolved Spectroscopy. The Journal of Physical Chemistry B 105:8281-8284.

20. Baranov, A. V., Y. P. Rakovich, J. F. Donegan, T. S. Perova, R. A. Moore, D. V. Talapin, A. L. Rogach, Y. Masumoto, and I. Nabiev. 2003. Effect of ZnS shell thickness on the phonon spectra in CdSe quantum dots. Physical Review B 68:165306.

21. Chirita, P., M. Descostes, and M. L. Schlegel. 2008. Oxidation of FeS by oxygen-bearing acidic solutions. Journal of Colloid and Interface Science 321:84-95.

22. Katari, J. E. B., V. L. Colvin, and A. P. Alivisatos. 2002. X-ray Photoelectron Spectroscopy of CdSe Nanocrystals with Applications to Studies of the Nanocrystal Surface. The Journal of Physical Chemistry 98:4109-4117.

23. Young, E. M. 1988. Electron-active silicon oxidation. Applied Physics A: Materials Science & Processing 47:259-269.

24. Sharp, I. D., Q. Xu, C. W. Yuan, J. W. B. J. W. Ager, III, D. C. Chrzan, and E. E. Haller. 2007. Kinetics of visible light photo-oxidation of Ge nanocrystals: Theory and in situ measurement. Applied Physics Letters 90:163118.

25. Tang, J., and R. A. Marcus. 2005. Mechanisms of fluorescence blinking in semiconductor nanocrystal quantum dots. The Journal of Chemical Physics 123:054704.

26. Tang, J., and R. A. Marcus. 2005. Diffusion-Controlled Electron Transfer Processes and Power-Law Statistics of Fluorescence Intermittency of Nanoparticles. Physical Review Letters 95:107401.

27. Frantsuzov, P. A., and R. A. Marcus. 2005. Explanation of quantum dot blinking without the long-lived trap hypothesis. Physical Review B 72:155321.

28. Wang. 2001. Calculating the Influence of External Charges on the Photoluminescence of a CdSe Quantum Dot. The Journal of Physical Chemistry B 105:2360-2364.

29. Jones, M., S. S. Lo, and G. D. Scholes. 2009. Quantitative modeling of the role of surface traps in CdSe/CdS/ZnS nanocrystal photoluminescence decay dynamics. Proceedings of the National Academy of Sciences 106:3011-3016.

30. Califano, M., A. Franceschetti, and A. Zunger. 2005. Temperature Dependence of Excitonic Radiative Decay in CdSe Quantum Dots: The Role of Surface Hole Traps. Nano Letters 5:2360-2364.

8. Conclusion

Quantum Dots (QDs) exhibit novel nanoscale physics and are truly an interdisciplinary field of research with applications from the biomedical through to the nano-electronic, optical, and physical fields of inquiry. They are used in self-assembly to produce supramolecular structures and are combined with polymers to make a number of composite novel materials. Their potential for biophysical studies has been proven in experimental applications that demonstrate that semiconductor nanoparticels can be made biocompatible and used as photostable fluorescent probes to label biomolecules within living cells and in extracellular domains.

Despite the wide range of applications and fundamental research that has been performed, some essential questions remain unanswered. The broad range of blinking time scales characteristic of the “on” and “off” time power-law distributions observed in CdSe/ZnS QDs affect applications of these nanoparticles for quantitative biophysical studies based on correlation analysis methods. On the other hand, blinking is a very useful phenomenon which can serve as indicator of single molecule detections. If multiple “on” time intensity steps are present in QD time traces, they can serve as indicators of several QDs beeing in close proximity to each other and allowing for measurement of distances on the order of tens of nanometres. Because blinking is sensitive to immediate QD surroundings, understanding the dependence of blinking dynamics on environmental factors, such as salt concentration of the solution, ionic strength, amount of dissolved oxygen or pH, are necessary for any quantitative measurements involving single quantum dots. Traditional statistical characterization of blinking relies on histogram binning of the “on” and “off” time durations, but it is not suitable for dynamic measurements involving correlation spectroscopy for example.

We therefore measured and characterized the ensemble intensity correlation function of blinking CdSe/ZnS quantum dots immobilized on a glass surface using time image correlation spectroscopy (TICS), and showed that it could be fit to a three parameter power law characteristic of QD blinking dynamics. Determining optimal conditions for single QD studies proved to be of crucial importance for the detection of changes in blinking. Those include surface densities smaller than one QD per square micrometer, sufficient number of the emitters in the ensemble, adequate temporal sampling and laser illumination intensities smaller or equal to the QD saturation excitation. Only severe changes in blinking can be detected when QDs are in the saturation regime and those are often caused by fast degradation processes.

The information provided by the correlation measurements of fluorescence blinking of static QDs can further be utilized to examine the accuracy of the mobility parameters recovered from TICS when CdSe/ZnS nanocrystals are used as labels of diffusing receptors in the membrane of CHO cells. We observed systematic errors which were present even when blinking was minimized. This effect was especially pronounced for higher temporal sampling and illumination intensities. In general, one could use high temporal sampling at excitation intensities significantly lower than the saturation intensity to recover blinking power law exponent and use it to estimate proper diffusion coefficient, but that process is long and not always possible. Instead, k-space image correlation spectroscopy (kICS) should be used as it mathematically separates signal fluctuations caused by diffusion and blinking.

A major research thrust has tried to explain the inverse power law distribution functions describing the durations of on-times and off-times. There has been a recent surge in the progress on the fluorescence blinking phenomenon in quantum dots. The initially proposed theories of electron ejection via an Auger mechanism as the route of blinking have been reevaluated and newer theories based on internal trapping at the surface have been developed within the last couple of years. These newer theories have gained some experimental support, but much more work on verifying them is needed. The observations of fluorescence blinking and the presence of a dark fraction in the QDs were initially unexpected observations. We have experimentally observed that changing the pH of the solution surrounding the QDs systematically affects the blinking dynamics, individual QD emission intensity and the dark fraction formation. From our results, we have proposed a model, based on the newer energy fluctuations and internal trapping models developed by Rudolf Marcus and coworkers, showing that the physics underlying both blinking and dark fraction formation have a common mechanism that is dependent on charges at the QD surface, which in our case is the H^+ ion. We found an irreversible decrease in the ensemble fluorescence intensity, a decrease in the brightness of single QDs and an increase in the dark fraction with decreasing pH from 9 to 6. The irreversible decay in fluorescence intensity with time indicated that a permanent formation of trap states was responsible for observed changes. Both H^+ and O_2 were found to be important for the fluorescence decay, suggesting that a proton-catalyzed oxidation process was responsible for the decay. Above a certain threshold of the number of trap states formed, the QD is trapped in a permanent "off" state thus contributing to an increase in the dark fraction. These results indicate that a common mechanism underlies the dark fraction formation, fluorescence blinking and fluorescence lifetime change of quantum dots, and relate physical and chemical properties of single QDs to their ensemble fluorescent properties.

We believe that the study described in this thesis will be of interest to a wide audience in the field of nanomaterials and biophysics due to the wide range of uses of QDs in optical applications, many of which are in solution and in different pH environments. These results will be extremely important to further develop the theory of QD blinking, but will be also appreciated by experimentalists using QDs in quantitative cellular biological applications, in which changes in pH are an important parameter. The use of QDs in biological imaging is one of the most successful applications of QDs. Well understood optical effects open up the possibility of using blinking dynamics of quantum dots as spatial and temporal resolved sensors of QD environmental changes.

List of Publications

A. Bachir, N. Durisic, B. Hebert, P. Grutter, P. W. Wiseman. Characterization of Blinking Dynamics in Quantum Dot Ensembles using Image Correlation Spectroscopy. J. Appl. Phys. 99: 064503-1-064503-7 (2006).

N. Durisic, A. I. Bachir, D. L. Kolin, B. Hebert, B. C. Lagerholm, P. Grutter, P. W. Wiseman. Detection and correction of blinking bias in image correlation transport measurements of quantum dot tagged macromolecules. Biophys. J. 93: 1338-1346 (2007)

Brett A. Kaufman* , Nela Durisic* , Jeffrey M. Mativetsky, Santiago Costantino , Mark A. Hancock, Peter Grutter, and Eric A. Shoubridge. The Mitochondrial Transcription Factor TFAM Coordinates the Assembly of Multiple DNA Molecules into Nucleoid-like Structures. Vol. 18, Issue 9, 3225-3236, September 2007 (*joined first authorship)

M. Slim, N. Durisic, P. Grutter, H. F. Sleiman; “DNA-Protein Non-Covalent Crosslinking: Ruthenium Dipyridophenazine Biotin Complex for the Assembly of

Proteins and Gold Nanoparticles on DNA Templates", ChemBioChem, 2007, 8, 804-812

N. Durisic, P. W. Wiseman, P. Grutter, C. Heyes. A common mechanism underlies the dark fraction formation and fluorescence blinking of quantum dots. ACS Nano 3(5): 1167-1175 (2009)

Nela Durisic, Antoine G. Godin, Paul W. Wiseman, Peter Grütter and Colin D. Heyes. Ensemble and Single Particle Emission Properties of CdSe/ZnS Quantum Dots in Biologically Relevant pH Range. To be submitted.